Passive and Active Approaches to Sustained Turbulent Hydrodynamic Drag Reduction using Superhydrophobic Surfaces

By

Dhananjai V Saranadhi
B.S. Mechanical Engineering
Massachusetts Institute of Technology, 2014

SUBMITTED TO THE DEPARTMENT OF MECHANICAL ENGINEERING IN PARTIAL FULLFILLMENT OF THE REQUIREMENTS FOR THE DEGREE OF

MASTER OF SCIENCE IN MECHANICAL ENGINEERING
AT THE
MASSACHUSETTS INSTITUTE OF TECHNOLOGY

September 2015

Signature redacted

Signature of Author: ______________________________

Dhananjai V Saranadhi
Department of Mechanical Engineering
August 3rd, 2015

Signature redacted

Certified by: ______________________________

Gareth H. McKinley
Professor of Mechanical Engineering
Thesis Supervisor

Signature redacted

Accepted by: ______________________________

Accepted by David E. Hardt
Ralph E. and Eloise F. Cross Professor of Mechanical Engineering
Graduate Officer

Passive and Active Approaches to Sustained Turbulent Hydrodynamic Drag Reduction using Superhydrophobic Surfaces

By

Dhananjai Saranadhi

Submitted to the Department of Mechanical Engineering on August 3, 2015 in partial fulfillment of the requirements for the degree of Master of Science in Mechanical Engineering

Abstract

Superhydrophobic surfaces have been shown to trap a pocket of air (or a "plastron") in between the features of their rough texture when submerged in water. A partial slip condition is created at the interface between the water and the submerged body, allowing for a reduction in skin friction drag.

I begin by identifying and fabricating several superhydrophobic surfaces, and testing their ability to reduce skin friction in turbulent flows using a bespoke Taylor-Couette apparatus. These superhydrophobic surfaces possess different surface topographies and chemistry, and exhibit different amount of drag reduction, leading to a deeper investigation of the role of surface chemistry and the roughness on the robustness of the plastron. The mean square slope as the driving roughness parameter in promoting plastron stability, and suggest methods by which it may be increased in order to optimize drag-reducing performance.

The air plastron captured by a passive superhydrophobic surface represents one way of creating a slip boundary condition. An active approach can be used to augment slip at the boundary. With this approach, a submerged body is heated past its Leidenfrost temperature to form a thick, continuous film of steam between itself and the water. I continue to employ superhydrophobic surfaces, but now exploit their unique heat transfer properties (*i.e.* the insulation to heat transfer provided by the minimal contact area between the body and the surrounding water) to drastically reduce the Leidenfrost Temperature and Critical Heat Flux, and by extension the energy input required to

create and sustain such a boiling film. In the active case, vapor film completely envelops the heated body and is thicker than a typical passive plastron, which allows for a significant increase in obtained drag reduction relative to a passive superhydrophobic surface. I design and fabricate a mechanism by which a Taylor-Couette rotor can be heated past its Leidenfrost point and continuously supplied with power to maintain a boiling film under rotation rates of 60 rad/s. The results show that skin friction can be reduced by over 90% relative to an unheated superhydrophobic surface at *Re* = 52,200, and I derive a boundary layer and slip theory to fit the data to a model that calculates a slip length of 1.04 ± 0.3 mm. This indicates that the boiling film has a thickness of 37 ± 9.5 μm, which is consistent with literature.

Acknowledgements

It has been a pleasure and an honor to work with Professor Gareth McKinley. His knowledge of science is matched only by his pedagogical ability, and he taught me a great deal while guiding me to seek further knowledge and understanding for myself. Professor Robert Cohen, my *de facto* co-advisor was equally instrumental in my development as a scientist and his constant supply of encouragement and optimism made the going that much more enjoyable.

This would have been a grueling year were it not for the incredible group of people with whom I worked. I'm particularly grateful to Justin Kleingartner for his advice, support, and above all his friendship. I will truly miss Bavand Keshavarz's unique sense of humor, his direct approach to life and his ability to make even the difficult days enjoyable. Siddarth Srinivasan has been great mentor and friend, and his endlessly helpful nature has inspired me to try to emulate him. Finally, Dayong Chen's kindness and commitment made him a great collaborator within lab and great company outside it.

I'd also like to thank Michela, Caroline, Ahmed, Divya, Setareh and Alex for making long days at lab a lot more fun that I could have ever imagined, and for their friendship.

I owe everything I have achieved to my family. My parents have always been a source of unconditional love and support and having my sister and brother-in-law close by has been a blessing, allowing us to spend more time together than ever before. I can

only hope to be as kind and generous towards my family as they have always been to me.

Contents

List of Figures

List of Tables

Chapter 1 : Background and Introduction

The research I present in this thesis seeks to reduce the drag of bodies moving in water. I concern myself primarily with those flows that have high Reynolds numbers. While previous studies have sought to achieve this using a breadth of methods (Bushnell and Moore, 1991), my approaches will leverage the properties of superhydrophobic surfaces. When a superhydrophobic surface is immersed in water, it retains a discontinuous layer of air known as a *plastron* between itself and the liquid (McHale *et al.* 2010). Figure 1.1 shows side-by-side images of a superhydrophobic bird feather immersed in water and oil. A shiny, reflective plastron is clearly visible in water, but as the oil wets the feather, no plastron is visible. The optical mechanism by which this silvery reflection is created is shown schematically in Figure 1.2.

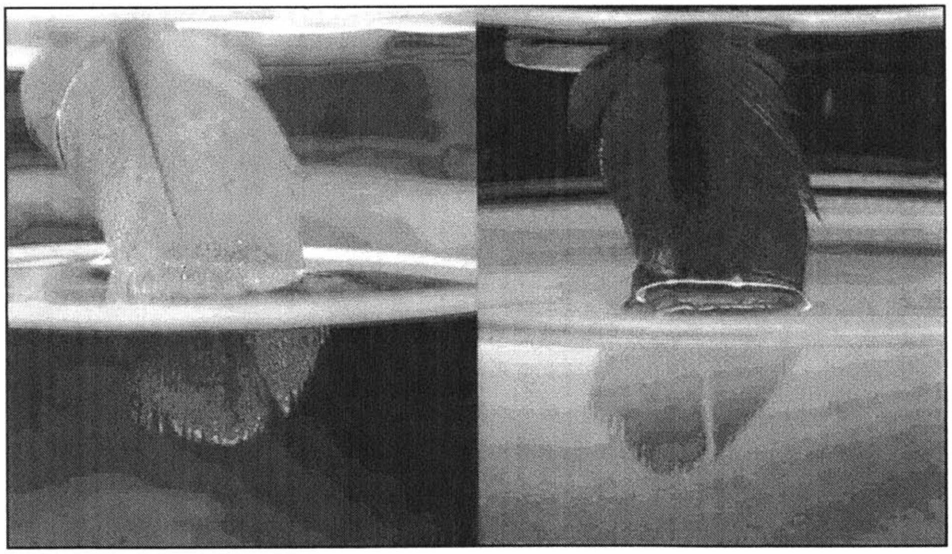

Figure 1.1: Superhydrophobic bird feathers immersed in water (L) and oil (R). A reflective plastron is clearly visible in water, but not in oil. (S. Srinivasan and J. Kleingartner)

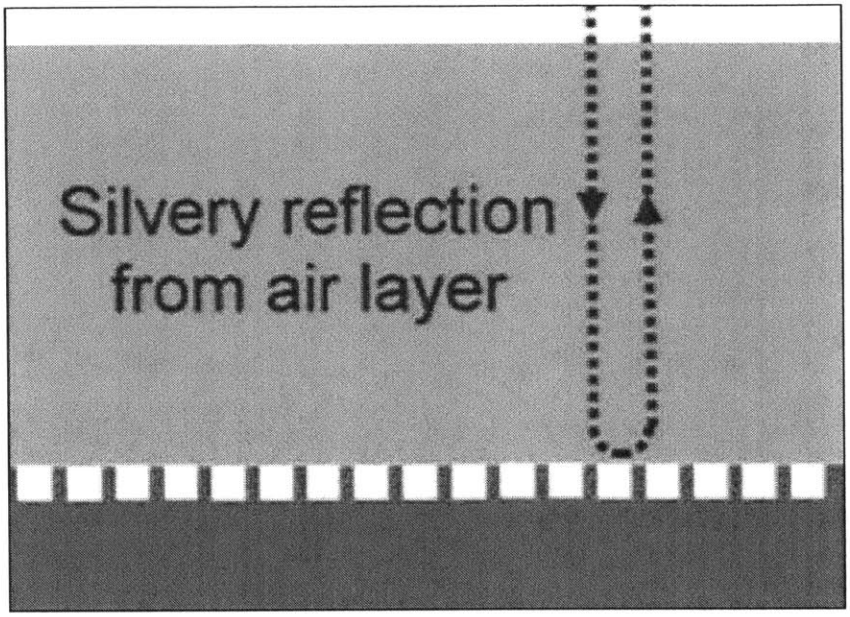

Figure 1.2: Schematic of an immersed superhydrophobic surface with a silvery reflection from a plastron (McHale *et al.*, 2010).

The interface is therefore a combination of slip and non-slip boundary conditions in flow. I begin by extending the work of Siddharth Srinivasan, a former student in the same research group who was able to create a superhydrophobic surface that consistently reduced drag in turbulent flow regimes. Furthermore, he was able to use slip theory to explain these results, and in doing so, lay the foundation for my work (Srinivasan *et al.* 2015).

While Srinivasan was able to identify a particular chemistry and process to create a superhydrophobic surface that functioned well, it was by no means the only option. Since the chemical agents he used are either in short supply or have since been banned, I start by creating my own superhydrophobic surfaces and using these to achieve drag reduction on a similar scale. Since the surfaces that I consider all show varying degrees of robustness to wetting and ability to reduce drag, I analyze the main drivers behind their performance and identify the parameters that must be optimized to create a surface that resists wetting and delivers high drag reduction.

The bulk of my research and hence a substantial part of this manuscript breaks from the passive approaches discussed above, and seeks to achieve drag reduction via active heating of the microtextured surface. Superhydrophobic surfaces are still used, but now a different property of the surface exploited. The low surface energy and heat transfer properties of these surfaces results in a highly reduced Leidenfrost temperature -the temperature above which stable film boiling occurs (Quere, 2003)- allowing them to attain film boiling at temperatures not much greater than 100°C (Vakarelski *et al.*, 2012). The steam film formed is similar to the passive plastron of a non-heated superhydrophobic surface, but is thicker and is continuous (Bonsignore, 1981). A film boiling sphere is shown in Figure 1.3.

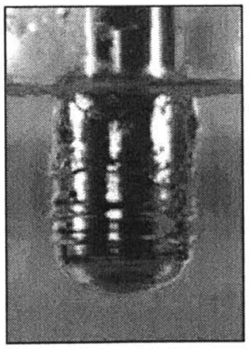

Figure 1.3: A superhydrophobic body at in the film boiling regime, showing a boiling film

The absence of pinning points and the larger gas fraction stored in the film promises substantially enhanced drag reduction, at the expense of an energy input required to heat the body to the Leidenfrost temperature and maintain it there (Vakarelski, Marston *et al.*, 2011). In the following sections, I introduce some key concepts spanning an array of disciplines to provide background for my work, briefly summarize Srinivasan's results, and provide an outline for this thesis.

1.1 Wetting on Flat and Textured Surfaces

1.1.1 Wetting on Flat surfaces and Young's equation

A droplet of water placed on a flat, homogeneous surface either spreads out to form an even film, or assumes the shape of a static drop (DeGennes, 2014). The drop can be characterized using the concept of a contact angle, measured at the interface of the solid, liquid and gaseous phases. Figure 1.4 shows the location of the contact angle measurement in relation to the drop.

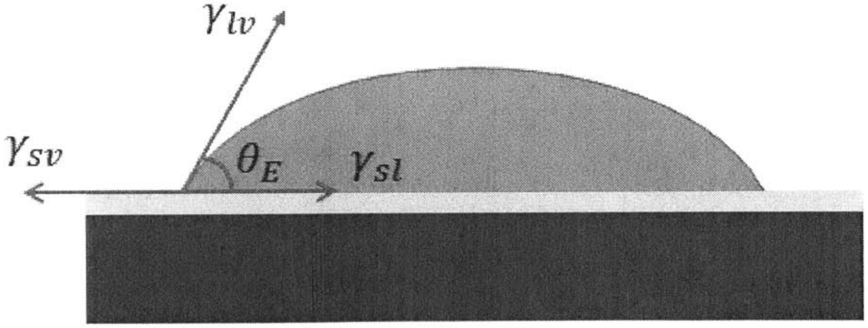

Figure 1.4: Schematic of a water droplet partially wetting a surface

The contact angle is such that it balances the forces acting upon the drop due to the surface tension, according to Young's equation (Young, 1805), reproduced here in equation (1.1).

$$\gamma_{lv}\cos\theta_E = \gamma_{sv} - \gamma_{sl} \tag{1.1}$$

Where γ_{lv} is the water-air interfacial tension, γ_{sv} is the substrate-air interfacial tension, γ_{sl} is the substrate-water interfacial tension, and $\cos\theta_E$ is the Young's contact angle. The value of the contact angle on a flat, homogeneous surface is thus entirely dependent upon the surface energies at the interfaces. As this manuscript deals exclusively with hydrodynamic effects in the environment, the two fluids of interest are fixed to be water and air. The only remaining variables are thus the solid-liquid and solid-air surface energies. These depend on the chemistry of the surface, and can be modified be adding a number of functional groups to the surface. These functional groups can be deposited in a number of ways, including chemical vapor deposition (CVD) (Kovacik, 2015), spraying, silanization in both the vapor and liquid phase (Hayn *et al.* 2011, Tasaltin *et al.* 2011), and through layer by layer assembly (Zhang, 2007). In creating and studying the effects of superhydrophic surfaces, each of these methods is explored further in this thesis.

The contact angle is the material parameter used to describe a surface as hydrophobic or hydrophilic. In general, a value of the Young's contact angle between 0 and 90 degrees is considered indicative of hydrophilicity, while any value greater than this is usually deemed hydrophobic. The latter feature a critical surface tension (unique for any solid and is determined by plotting the cosine of the contact angles of liquids of different surface tensions and extrapolating to 1), often close to 35 mN/m, while the former generally features surface energies above 45 mN/m (Arkles, 2006).

1.1.2 Advancing and Receding Contact Angles

In practice, surfaces are rarely perfectly flat and homogeneous, and this, combined with local pinning of the contact line, makes measuring the contact angle that represents the global thermodynamic minimum difficult.

Since any of the various local minima can be occupied by a drop at equilibrium, any number of angles could be measured (Marmur, 2009).

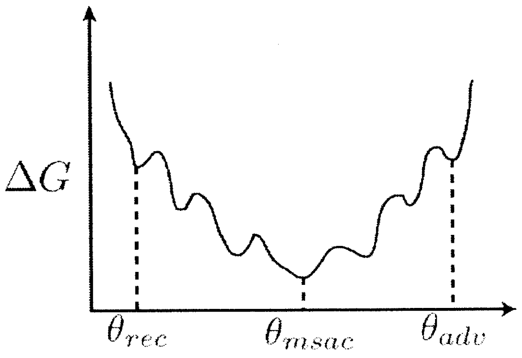

Figure 1.5: Plot of dimensionless free energy as a function of observable contact angle. Each of the local minima can be measured experimentally. θ_{rec} and θ_{adv} are the upper and lower limits, while θ_{msac} represents the most stable point and is related to the Young's contact angle, $\theta_{E.}$ (Srinivasan, 2015).

However, there exists a global maximum and minimum angle of such states, and these are called the advancing and receding contact angles. As the name suggests, the advancing contact angle occurs when the volume of the drop increases, causing its 3-phase contact line to advance across the substrate. The receding angle is correspondingly the angle measured as the volume decreases. The difference between the two angles is termed the contact angle hysteresis. Both angles can be measured using a number of techniques, including tensiometry and goniometry. The accuracy in these measurements and the factors that affect them has been the subject of various studies (Kleingartner *et al.* 2013).

1.1.3 Wetting on Rough Surfaces

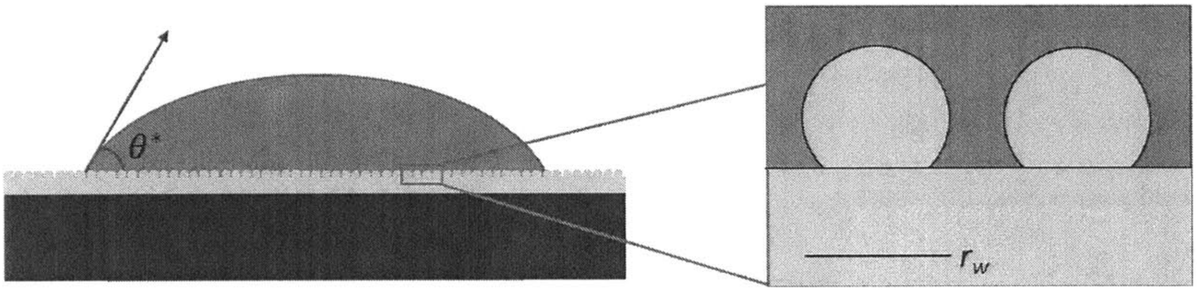

Figure 1.6: Wetting in the Wenzel state, with the water occupying the space between the asperities. The roughness parameter r_w is the ratio of the total surface area and the projected flat surface area.

Adding surface roughness to a surface of known contact angles can drastically alter the wetting behavior. Though the Young's contact angle, which is driven by the chemical makeup of the surface, remains unchanged, surface roughness serves to enhance and modify the properties of the surface. This can lead to a surface that could previously be described as hydrophobic taking on advancing and receding contact angles dramatically higher than before, often higher than 150°, with very little hysteresis (<1°). These surfaces can now be considered *superhydrophobic* (Lafuma and Quéré, 2003). The same is true for surfaces that chemically are inclined to wet to water; adding a microstructure of the correct size can make them *superhydrophilic*. The tendency of surface roughness to amplify wetting behavior at critical values of roughness can be explained using the Wenzel model of wetting (Wenzel, 1936). As shown in Figure 1.6, the Wenzel state is said to occur when the drop permeates in between the features that form the texture. A new contact angle, called the apparent contact angle or θ^*, is now macroscopically measured. It is related to the Young's contact angle (θ_E) by (1.2).

$$\cos\theta^* = r_w \cos\theta_E \tag{1.2}$$

The roughness is described using the parameter r_w, the Wenzel roughness, defined as the ratio of the actual surface area divided by the projected flat surface area. We can see from this equation that when θ_E is less than 90°, indicating a hydrophilic surface, having a value $r_w \geq 1$ makes θ^* smaller than θ_E, hence increasing the wettability of the surface. Analogously, for surfaces for which $\theta_E > 90°$ (so that $\cos \theta_E < 0$), the surface is found to behave more hydrophobically.

While the Wenzel model helps explain the amplification of wetting behavior, it does not account for surfaces with such drastically altered wettability that they merits a *super-* prefix. A different model is required, and one that serves the purpose well is the Cassie-Baxter model (Cassie & Baxter, 1944). Here, the liquid is assumed on only partially wet the solid. Where the Wenzel model assumed the liquid was occupying the area in between the features, the Cassie-Baxter model partially suspends the droplet on top of the features, with local contact occurring (Cassie *et al.*, 1944). This leads to a discontinuous layer of air getting trapped in between the features, as shown in Figure 1.7. This trapped air is known as a plastron (McHale *et al.* 2010), and will be a recurring theme of this thesis.

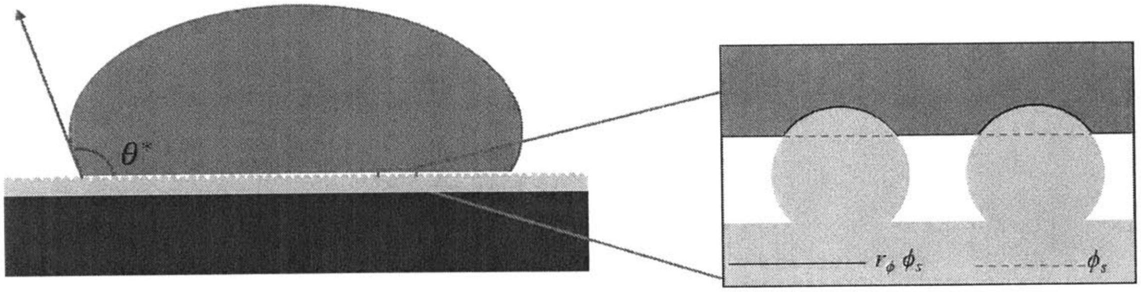

Figure 1.7: Partial wetting of a rough surface in the Cassie-Baxter surface, with air trapped in between the asperities. The wetted solid fraction $r_\phi\ \phi_s$ is shown.

Equating the interfacial energies allows us to obtain the Cassie-Baxter equation (1.3).

$$\cos\theta^* = r_\phi \phi_S \cos\theta_E + \phi_S - 1 \qquad (1.3)$$

Here, Φ_S represents the wetted solid fraction, and r_Φ describes the total surface roughness. The behavior that we are most concerned arises when the wetted solid fraction (Φ_S) approaches 0. In order for the equality to hold true, θ^* must approach 180°, which describes a perfectly non-wetting surface.

Further validation is lent to the theory by setting $\Phi_s = 1$, indicating a fully wetted surface, causing it to correctly reduce to the Wenzel equation.

1.2 Superhydrophobic Drag Reduction

For a regular, non-superhydrophobic body moving in water, there is a no-slip boundary condition at the water-solid boundary condition. In the reference frame of the body, in which it is stationary, the water thus has a velocity of zero at the point at which it touches the body. However, elsewhere, far away from the body, it has a finite velocity (equal to the body's velocity in the reference frame of a stationary observer). Thus, a non-uniform velocity profile is created close to the surface, and the slope of the profile evaluated at the boundary multiplied by the viscosity of the fluid yields the shear stress, as shown in (1.4).

$$\tau_w = \mu \left. \frac{du}{dy} \right|_{y=0} \tag{1.4}$$

This profile for a non-slipping surface is shown in Figure 1.8.

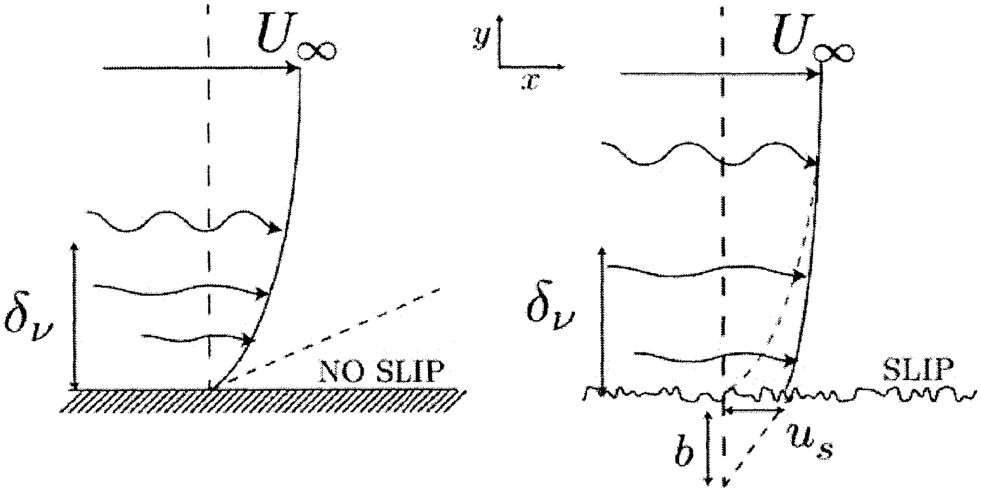

Figure 1.8: Velocity profiles over a non-slip surface and a partially slipping one, showing the slip length (S. Srinivasan, 2014)

However, a superhydrophobic surface submerged in water conserves a plastron of air about itself. Since the plastron is typically discontinuous, there are locally wetted spots at which a water-solid interface exists, and the above analysis applies. But the bulk majority of the surface will in fact feature the air in the plastron interacting with the water, resulting in a slipping boundary condition. The presence of a slip velocity means that the slope of the velocity profile is less steep, leading to a lower local value of the shear stress and hence a lower integrated friction force acting on the body (Ybert *et al.*, 2007). The resulting decrease in torque is described as *Drag Reduction,* in particular skin friction reduction. The drag acting on a body is generally the sum of two components: form drag (dependent upon the shape of the body), and skin friction (arises from the interaction at the wetted surface of the body). Skin friction is often the dominant component for streamlined bodies at high velocities (Cortana, 2014), and so it will be the central theme of this manuscript.

Large bodies in water moving at high speed tend to have large Reynolds numbers, defined in(1.5).

$$\mathrm{Re} = \frac{\rho L v}{\mu} \tag{1.5}$$

Where ρ and μ are the density and viscosity of the fluid medium (in this case water), respectively. L is a length scale factor, and v is the relative velocity between the body and the water. Since we are interested in turbulent flows, which is to say flows with high

Re, the experimental setup with capable of achieving this is required. One possible approach is a tow-tank, in which the force required to pull the body through water at a constant water is measured (Bill *et al.* 1976; Aljallis *et al.*, 2013). An alternative is a flow channel, in which the body remains stationary while the water flows over it (Woolford *et al.*, 2009; Daniello *et al.*, 2009). However, in both these cases, the setup is likely to consume a great deal of space and take a substantial amount of time to build. Furthermore, effects such as form drag have to be accounted for.

1.2.1 Bespoke Taylor-Couette Cell

A far more space and time-efficient solution was found in using a Taylor-Couette cell. The superhydrophobic body would be a cylindrical rotor, and it would be submerged into a larger cylinder water full of water. The sensitive torque transducer on a rheometer would be used to rotate the rotor at a specified angular velocity, and the torque required to sustain this angular velocity would be recorded through the rheometer software. In short, the concept is similar to a tow tank, but the motion is circular rather than linear, and drag reduction is computed from the measured torques rather than the forces required to sustain a constant linear velocity. The appropriate Reynolds number for a Taylor-Couette cell can be computed using (1.6) while the Taylor number is defined in (1.7).

$$\mathrm{Re} \equiv \frac{\Omega R_1 (R_2 - R_1)}{\nu} \tag{1.6}$$

$$Ta \equiv \frac{\Omega^2 (R_2 - R_1)^3 R_1}{\nu^2} = \mathrm{Re}^2 \left(\frac{R_2 - R_1}{R_1} \right) \tag{1.7}$$

Larger Reynolds numbers can be obtained by using a larger rotor and a larger gap, both of which call for a large cell radius. As most Couette cells designed for rheometry ensure a small gap, rheometer manufacturer TA Instruments provided a Taylor-Couette (TC) cell barely larger than its rotors. The maximum angular velocity that the instrument could reliably achieve is 250 rad/s, resulting in a Reynolds number of about 4,000 in water at room temperature. Srinivasan *et al.* were able to establish that the transition to featureless turbulence (Huisman *et al.,* 2014) occurred at Re = 12,000 (Figure 1.9). A new Taylor-Couette cell was designed and fabricated which allowed for a substantially larger gap of over 20 mm.

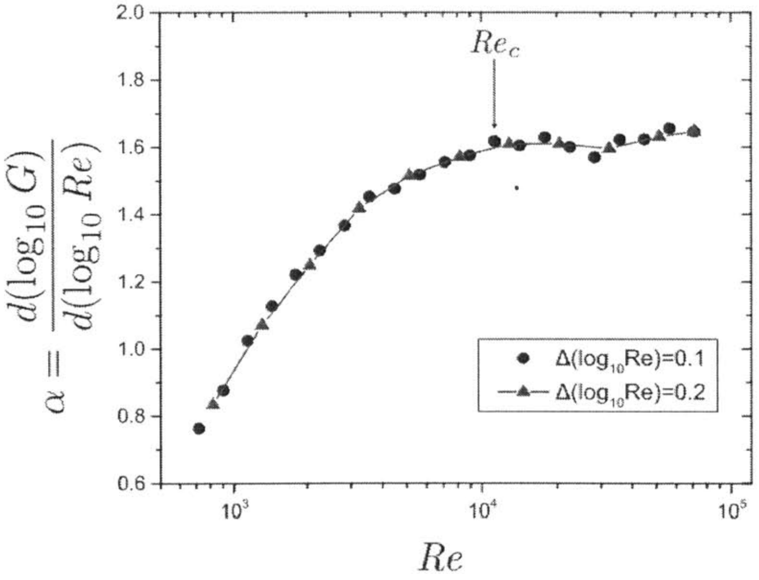

Figure 1.9: Plot of the local torque exponent as a function of the Reynolds number. The change in slope corresponds to the transition to the shear-driven turbulent flor region (Srinivasan et al., 2015)

A CAD and an image of the completed cell are presented in Figure 1.10.

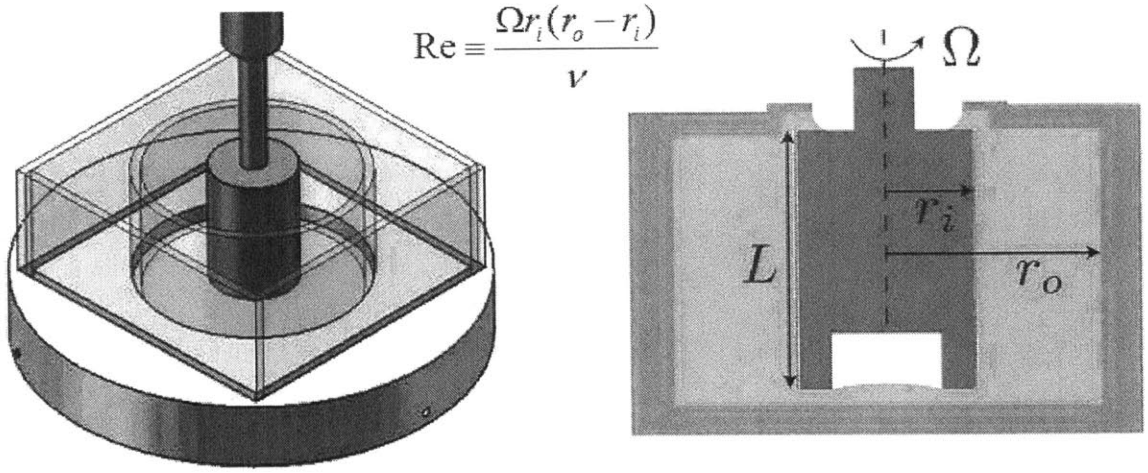

Figure 1.10: CAD (L) and schematic (R) of the rotor immersed in the Taylor-Couette cell. The Reynolds number for the system is defined. (S. Srinivasan, 2014).

Based upon this design, the author of this manuscript then machined an improved version of the wide-gap cell that allowed for a more compact construction. In addition to its bulk, the original cell also suffered from the fact that refraction took place at the curve cylinder, causing the light to move from air to water at an angle, leading to further refraction and a highly distorted image. The challenges in machining the new cell that overcomes these optics issues are discussed in Appendix A.

1.2.2 Measuring Drag Reduction

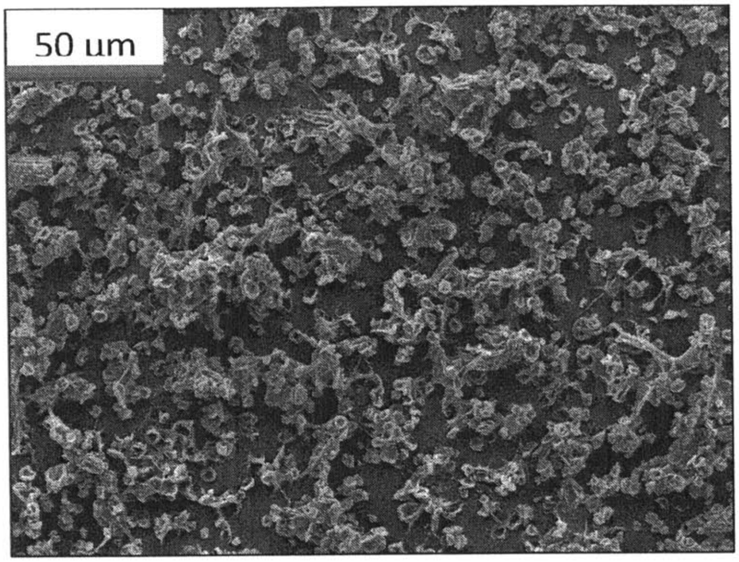

Figure 1.11: SEM of a sprayed PMMA-POSS surface

Using their bespoke Taylor-Couette cell, Srinivasan *et al*. were able to measure drag reduction. A flat, smooth rotor provided by TA Instruments was first inserted and the torques required to spin it at a range of velocities was measured. The same rotor was then sprayed using PMMA-POSS. The first of the two chemicals served to create a rough microstructure, while the second conferred upon the surface chemical hydrophobicity. The combination of the two yielded a robustly superhydrophobic surface. An SEM of this surface is presented in Figure 1.11.

.

Two different modes were considered: the "connected state", in which the rotor was sprayed upon its top surface, allowing air from the environment to get pulled in and replenish and augment the plastron, and the "unconnected" state, which isolated the superhydrophobic surface. This is presented schematically in Figure 1.12.

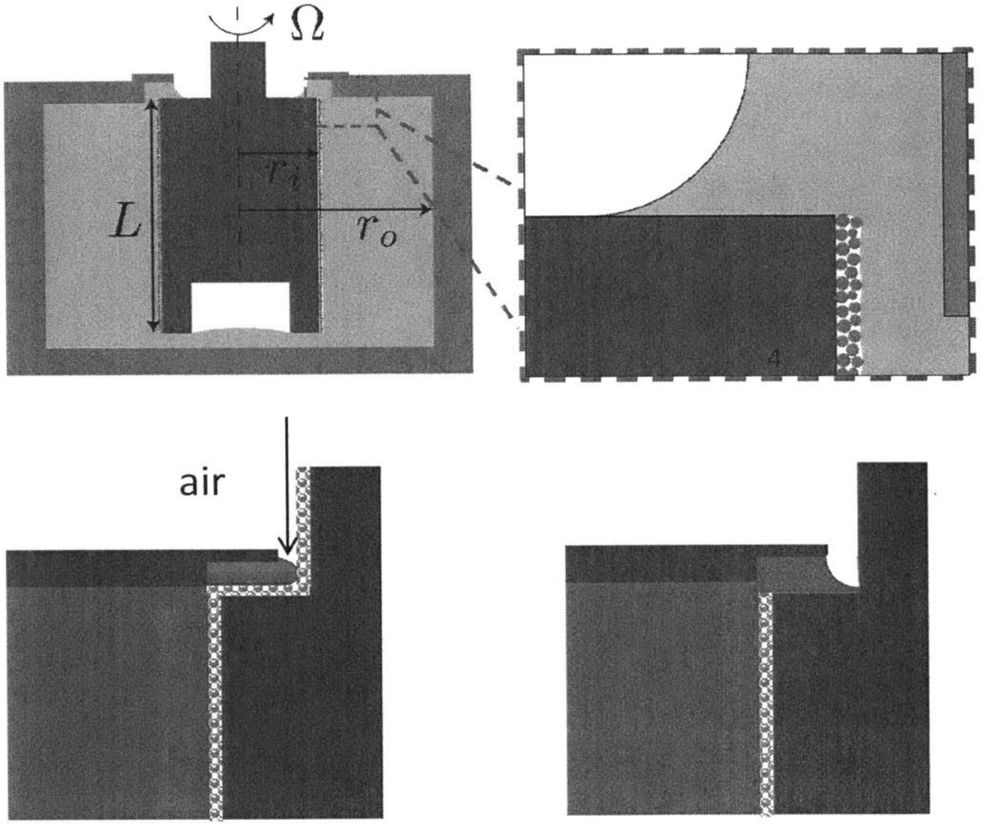

‘Connected’ ‘Unconnected’

Figure 1.12 Schematics showing the connected and unconnected states (Srinivasan, 2014)

The rotor, it should be noted, features a recessed end in order to prevent edge effects (Choi and Kim, 2006; Bocquet *et al.*, 2006).

Srinivasan *et al.*’s results are presented in Figure 1.13.

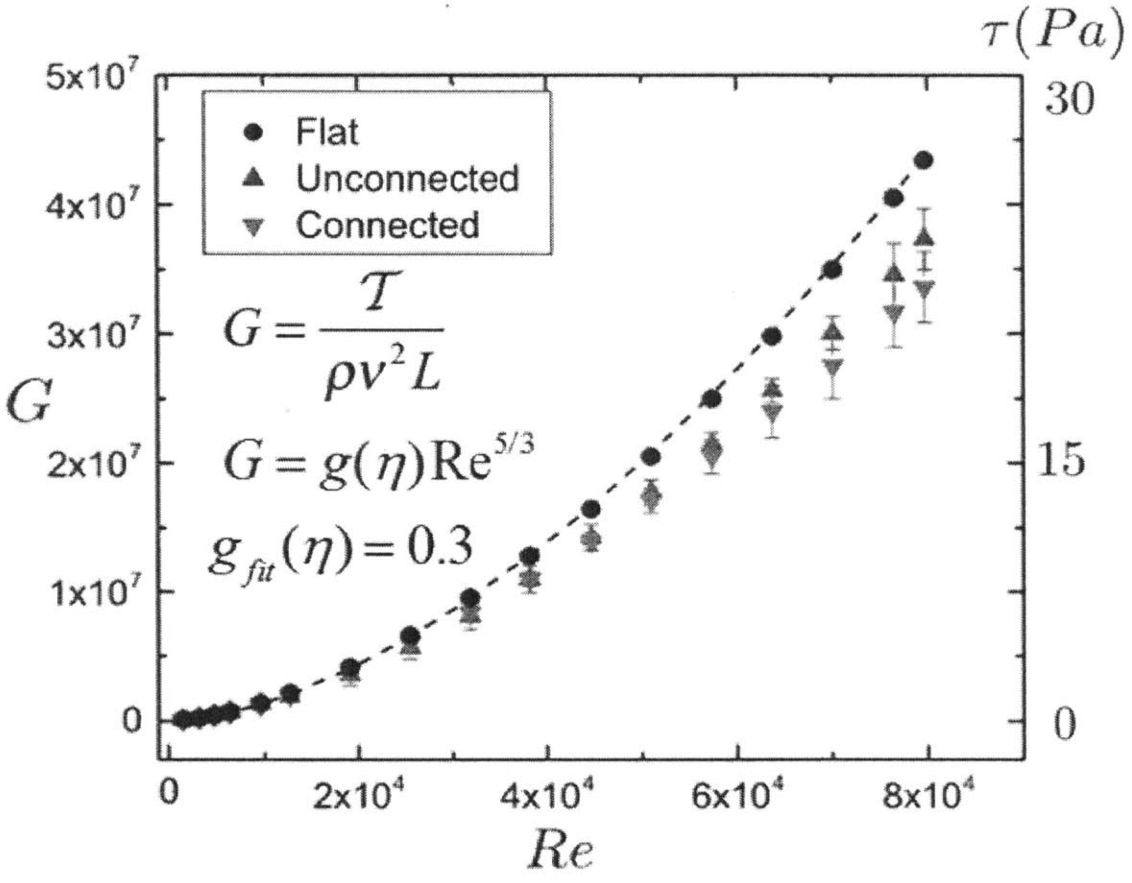

Figure 1.13: Graphical representation of Srinivasan *et al.*'s results, showing skin friction reduction at a range of Reynolds numbers

A maximum drag reduction of 22% was measured at Re = 80,000. As the figure above shows, drag reduction increases as a function of Reynold's number. This was explained by the fact that the viscous boundary layer becomes smaller as the flow becomes increasingly turbulent. Eventually, the width of this layer begins approaching the width of the plastron, allowing the trapped air to interact with the turbulent bulk flow. It is thus the relative scaling of the viscous sublayer and the trapped air that explain this drag reduction. Srinivasan *et al.* were also able to expand this theory further using the concept of a slip length, introduced in section 1.2. Indeed, by plotting the results in Prandlt- Von Kármán co-ordinates, they were able to predict the drag reduction created by the additional slip. The resulting plot is presented in Figure 1.14, while equation (1.8) shows the torque reduction due to the partial slip.

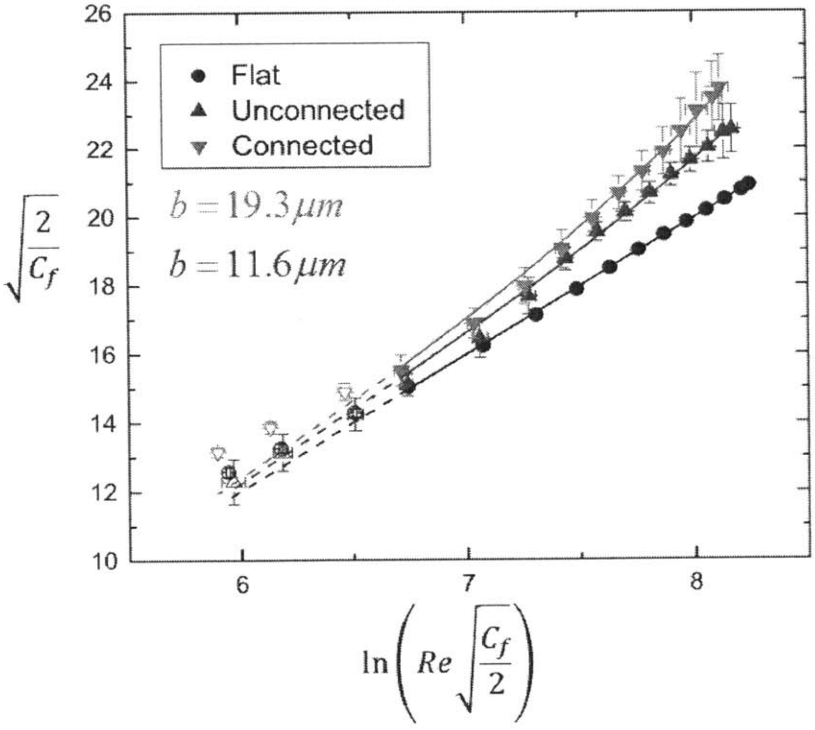

Figure 1.14 Measured skin friction plotted in Prandtl-von Kármán coordinates. The solid black line is the fit to the logarithmic skin friction law. The blue and green lines are fits for the connected and unconnected SH surfaces. (Srinivasan *et al.*, 2015).

$$\sqrt{\frac{2}{C_f}} = M\ln\left(\mathrm{Re}\sqrt{\frac{C_f}{2}}\right) + N + \left(\frac{b}{\Delta R}\right)\mathrm{Re}\sqrt{\frac{C_f}{2}} \tag{1.8}$$

The fact that a spray-on surface is capable of reducing skin friction opens the potential of a myriad uses, including usage on boats (Dong *et al.* 2003) and other marine vehicles.

A great deal of time has been devoted to summarizing Srinivasan *et al.*'s results, as their work proved to be a springboard for my own. The following sections of this document will first explain how I extended Srinivasan's work by seeking alternative drag reducing surfaces, and developing a theory that identifies the features of these surfaces that drives robust drag reduction. The bulk of this manuscript, however, deals with active drag reduction. While superhydrophobic surfaces are still used, they serve only to decrease the required energy input required to achieve drag reduction. A slip-based theory is derived to explain the observed drag reduction, which is on a much higher scale to everything discussed thus far. I conclude this work by discussing avenues for future research.

Chapter 2 : Making and Optimizing Superhydrophobic surfaces for Drag Reduction

2.1 The Search for Drag-Reducing Superhydrophobic Surfaces

As discussed in Chapter 1, Srinivasan *et al.* developed a robust superhydrophobic surface that reliably reduced skin friction in turbulent flows. PMMA-POSS, their most successful surface coating, achieved this via the random deposition of corpuscular PMMA spherical micro-structures with the hydrophobic agent Heptadecafluorodecyl Polyhedral oligomeric silsesquioxane (F-POSS) uniformly dispersed in the matrix. The latter is a fluorinated silicon-oxygen cage molecule (Meuler, 2011) and had to be specially produced through a multi-step synthetic process, giving it limited potential for scaling up (Mabry *et al.*, 2008). As such, it was essential that an alternative superhydrophobic surface that was capable of sustaining consistent turbulent drag reduction be identified.

As discussed in Chapter 1, making a superhydrophobic surface requires both chemical hydrophobicity as well as a rough micro-structure to amplify this property. Various surfaces were considered and tested to assess their ability to reduce drag.

2.1.1 PMMA + A Hydrophobic Agent

Creating a rough micro-structure can be achieved in many ways. For instance, PMMA (along with the hydrophobic POSS molecule) was dissolved in Asahiklin (Ak-225), a hydrochlorofluorocarbon, the sale of which was banned beginning in 2015. The solution was then sprayed through a two-fluid nozzle. Pressurized Nitrogen at 40 psig was used to disintegrate the liquid into drops, which were then expelled. The highly volatile Ak-225 largely evaporates in flight, leaving the corpuscular PMMA structures to deposit on the substrate. Extensive studies of the parameters required to create the desired surface characteristics have been done in order to optimize this (Srinivasan *et al.*, 2011). Initially, the author of this manuscript also used PMMA-POSS. Since the distance from the nozzle to the substrate and the rate of motion of the nozzle greatly impacted the resulting surface, the process was automated using a CNC gantry router (Shapeoko 2), which runs on conventional gcode. The system is pictured in Figure 2.1, while the user interface of the software and a visualization of the spraying path are shown in Figure 2.2 and Figure 2.3, respectively.

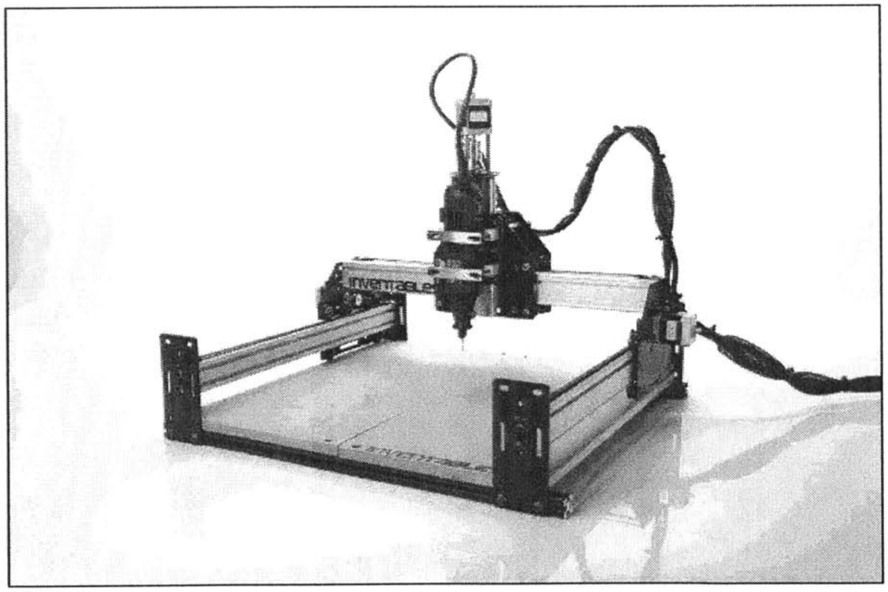

Figure 2.1: Shapeoko automated XYZ stage, assembled by J. Kleingartner

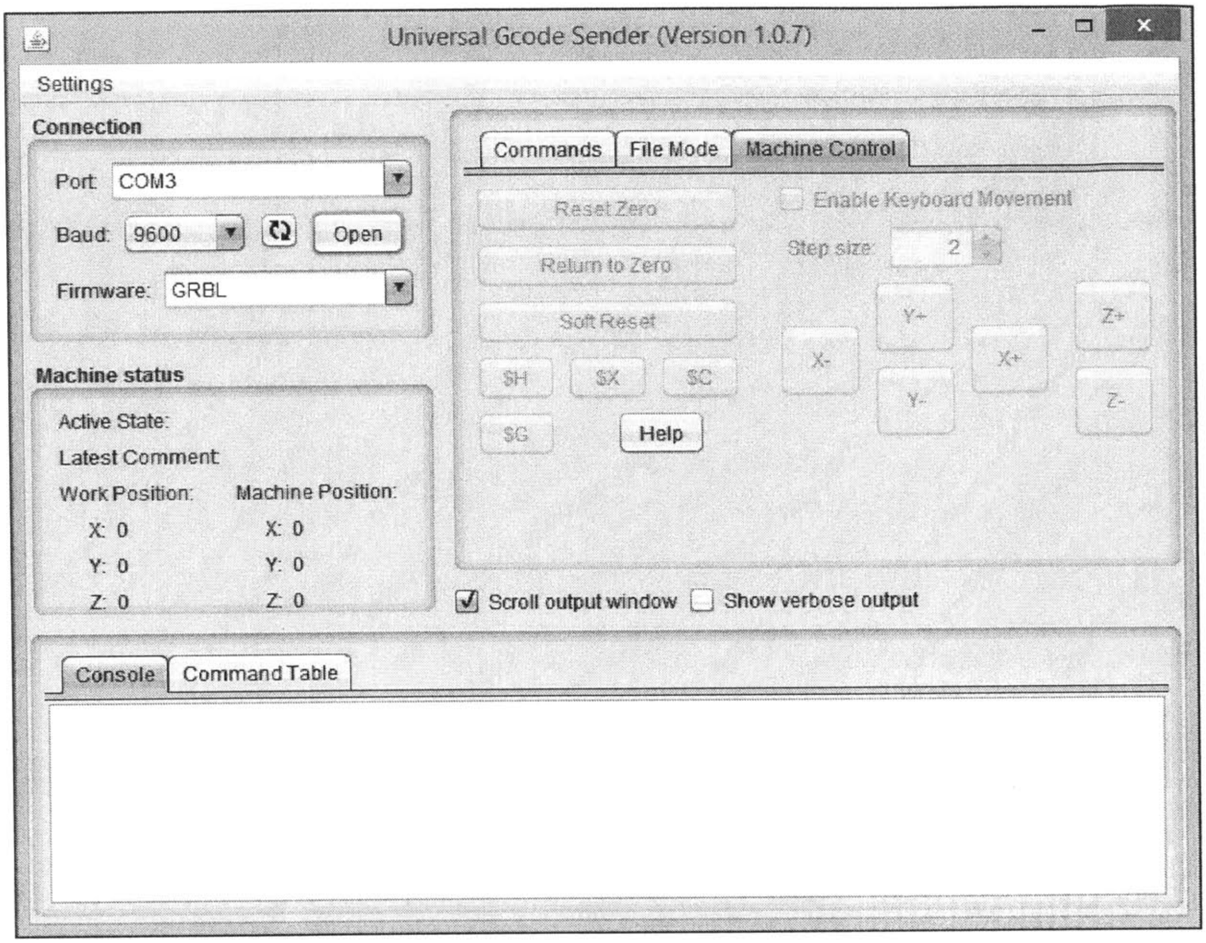

Port: COM3

Baud: 9600

Firmware: GRBL

☐ Enable Keyboard Movement

Step size: 2

Active State:

Latest Comment:

Work Position:	Machine Position:
X: 0	X: 0
Y: 0	Y: 0
Z: 0	Z: 0

☑ Scroll output window ☐ Show verbose output

Figure 2.2: User interface of the Java-based Shapeoko software used to send gcode to the XYZ stage

Two primary replacements for POSS were considered. The first of these was a variation of the Fluorodecyl POSS used in previous studies, but lacking two CF_2 groups. The resulting molecule, Fluorooctyl POSS (F8POSS), was thought to have many of the same properties, and was synthesized by a local company, NBD Nano. Initial impressions seemed to confirm this – a 50-50 mixture by mass of PMMA and F8POSS dissolved without issue in Ak-225 and sprayed with ease using the same nozzle and settings as Fluorodecyl POSS.

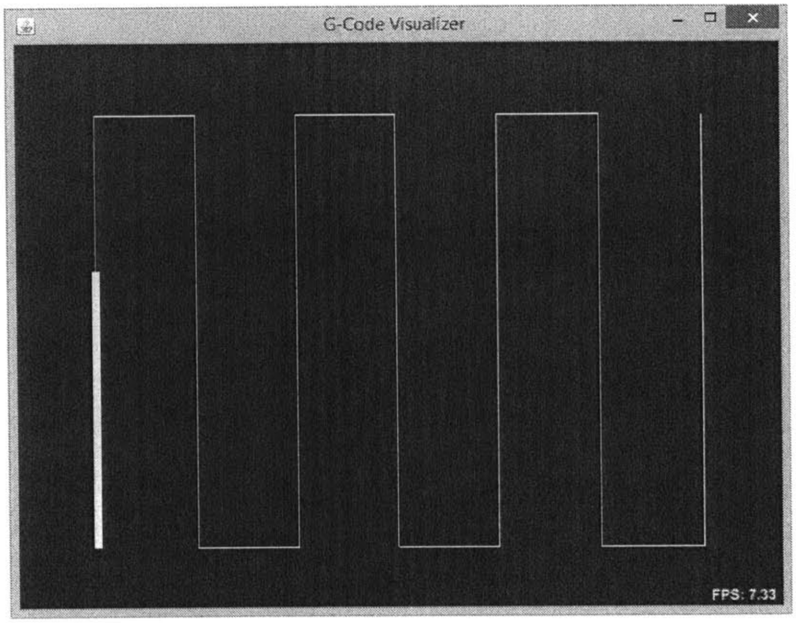

Figure 2.3: Visualization provided by the Shapeoko software of the nozzle path. The yellow line indicates the current position of the nozzle.

The resulting surface was certainly superhydrophobic, with contact angles in excess of 160° (θ_{adv} = 161°, θ_{rec}= 160°) with very little hysteresis (approximately 1°). Spraying water on the surface yielded promising results, with the jet of water bouncing off, leaving a dry surface. SEM images of the surface, shown in Figure 2.4 also showed a structure of the kind that was expected to reduce drag (Srinivasan *et al.*, 2011). However, when sprayed onto a rotor and tested for drag reduction in the Couette cell, PMMA-F8POSS yielded unsatisfactory results. The fact that there was no increase in frictional drag, which one would expect from a rough, non-SH surface, suggested that there was at least some slip occurring, but the drag reduction was minimal, as shown in

Figure 2.5, which plots non-dimensional torque $G = T/(\rho v^2 L)$ against the Reynolds number.

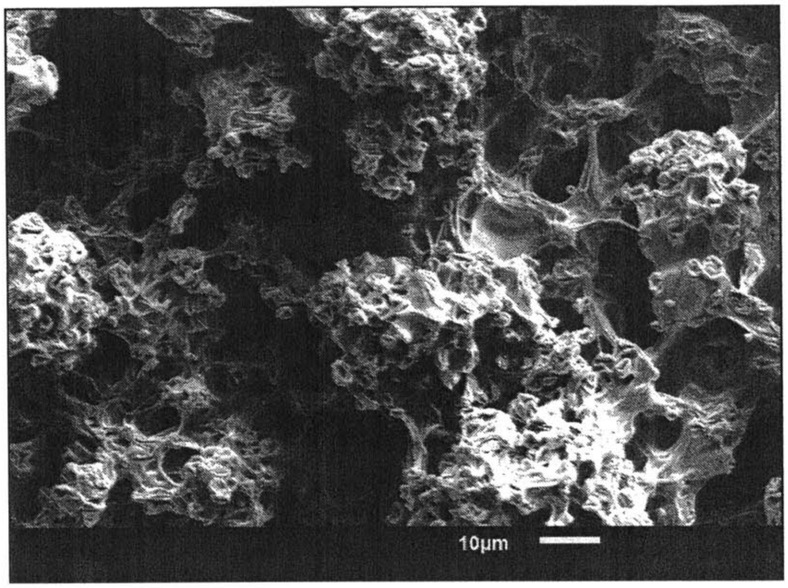

Figure 2.4: SEM of sprayed PMMA-F8POSS surface.

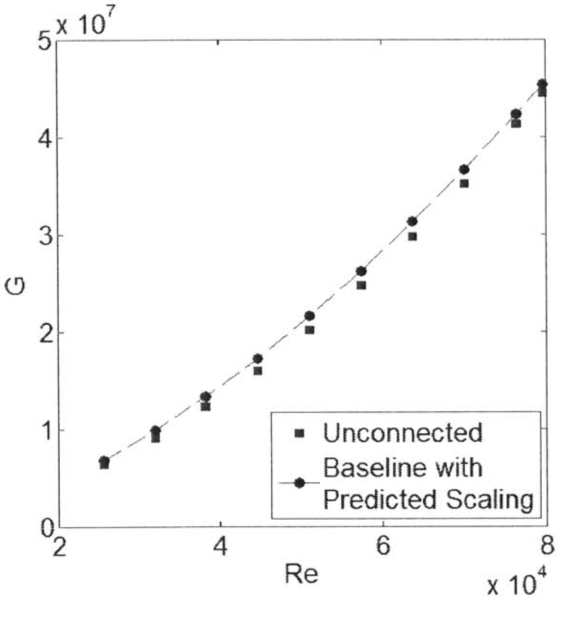

Figure 2.5: Plot of non-dimensional torque vs Reynolds number for PMMA-F8POSS surface. The black points correspond to a flat rotor, while the blue squares are data from the SH surface. The black dotted line is the predicted scaling.

Observing the graph of torque vs time for a fixed Reynolds number (defined in Figure 1.10) in Figure 2.6 seemed to shed more light on this.

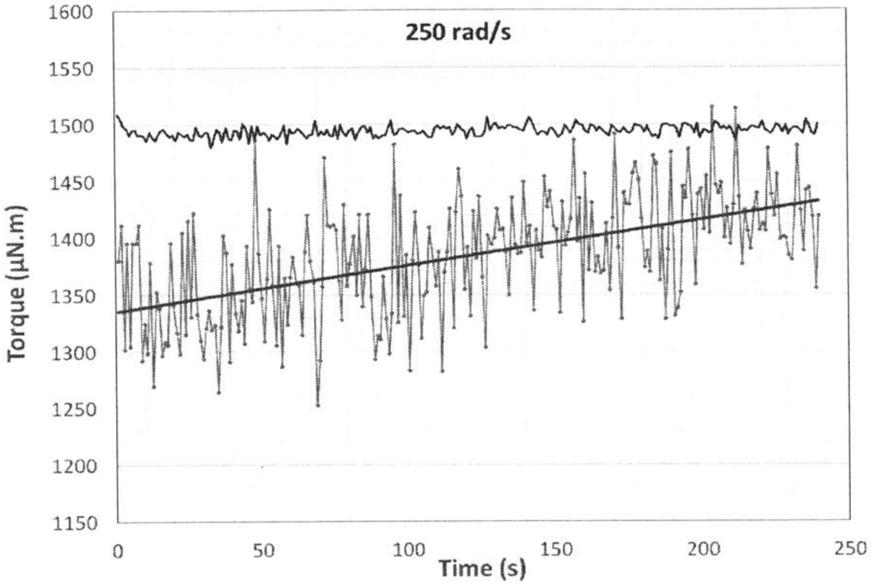

Figure 2.6: Trace of dimensional torque vs time for a fixed velocity of 250 rad/s

The gradual increase in torque with time suggests that the coating is losing effectiveness. The most likely cause for this is that it is getting mechanically worn away, and indeed, following a test, spraying water on the rotor resulted in a great deal of pinning, indicating that many areas had lost their superhydrophobicity. While a number of different fixes were tried, including varying the fraction of POSS and thermally annealing for different times at various temperatures, F8POSS never delivered on its initial promise of sustainable, robust drag reduction.

Since Fluorodecyl POSS (F10POSS) had given good results with the same sprayed-PMMA microstructure, it was determined that the hydrophobic agent (and not the PMMA-based rough microstructure) was most likely to be at fault for the failure of the PMMA-F8POSS coating. An alternative was considered in the form of poly(perfluorodecylacrylate) (PFDA) with the collaboration of Dr. Hossein Sojoudi. Like POSS, this is a fluorinated organic molecule. However rather than being sprayed along with the PMMA, the PFDA was deposited upon the PMMA in a conformal layer using initiated Chemical Vapor Deposition iCVD (Sojoudi *et al.* 2014). An SEM of the resulting surface is depicted in Figure 2.7. While displaying high contact angles, initial results were not promising, showing minimal drag reduction. However, adding a thick layer of poly(divinyl benzene) (DVB) caused the fluorinated groups of the PFDA to lock in place (Sojoudi, Walsh, Gleason and McKinley, 2015) and this caused the drag reduction performance to improve dramatically, as shown in Figure 2.8.

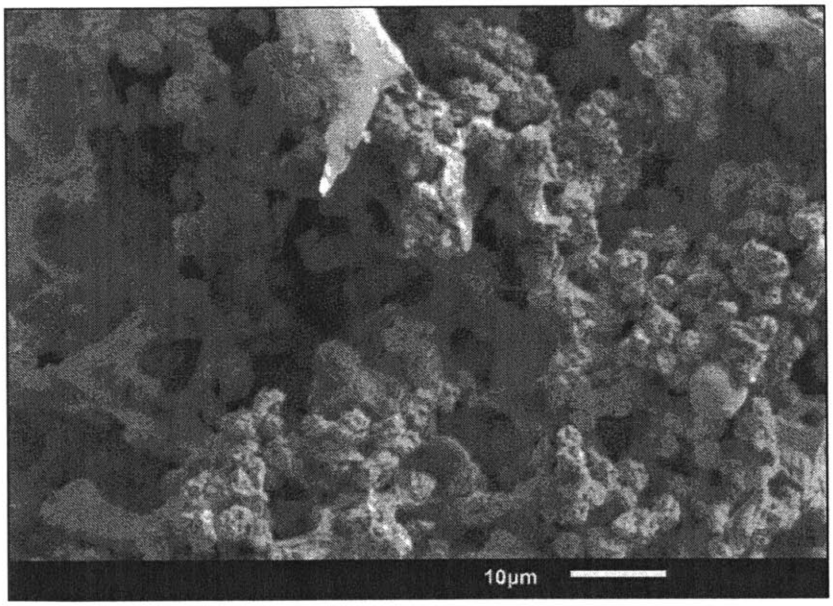

Figure 2.7: SEM of PMMA-PFDA surface, created by first spraying PMMA in Ak-225 and then adding the PFDA *via* iCVD.

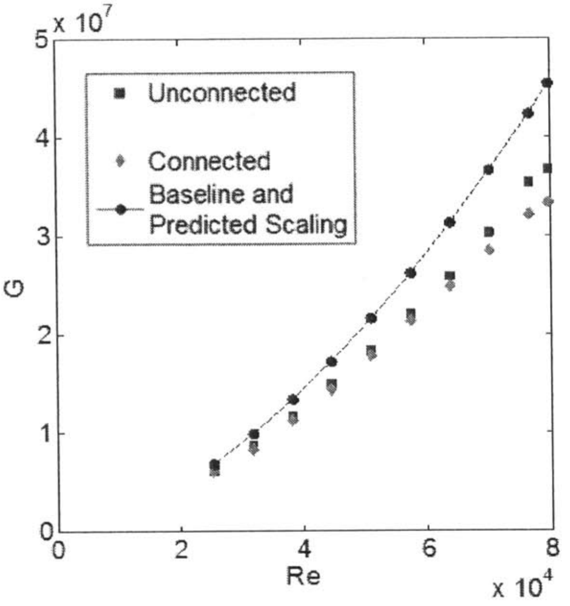

Figure 2.8: Plot of non-dimensional torque vs Reynolds number for PMMA-PFDA.

The maximum observed drag reduction was 26%, which was on par with the best results observed from PMMA/POSS. The slip length was found to be somewhat lower (11 μm, compared to PMMA/POSS's 19 μm), which is to be expected, given the lower contact angles of the PFDA-based surface. However, the emergence of PMMA/PFDA as a viable alternative to PMMA/POSS assured that a suitable drag reducing surface would always be available for any further studies.

2.1.2 A Surface Created by iCVD in a Single Step

As previously mentioned in the discussion of PFDA, iCVD can be used to deposit a conformal layer of PFDA on a rough PMMA surface. DVB was also added to decrease the mobility of the fluorinated chains. However, with the collaboration of Dr. Hossein

Soujoudi, it was possible to eliminate the first step of the process (spraying of PMMA). The rough surface was instead created by grafting DVB directly onto the metal surface, and the PFDA was laid over this in a conformal layer. The surface's contact angles (θ_{adv} = 154°, θ_{rec}= 150°) quite as high as those of PMMA-based surfaces , but unlike the white PMMA coatings, these iCVD-made coatings were transparent. While this did not make a great deal of difference to our attempts to achieve drag reduction, there are a plethora of applications that would benefit from a totally transparent superhydrophobic surface. The transparent surface was also able to achieve reasonably good drag reduction, peaking at 15%. As before, Figure 2.9 shows a graph that shows drag reduction.

A great deal of room remains to experiment with the iCVD parameters to optimize the surface for drag reduction and make it more robust. Unlike PMMA, which does not adhere very well to the surface of a metal, grafting has the potential of offering a better bond to aluminum, thus making it harder to remove the superhydrophobic surface through mechanical abrasion.

The most glaring flaw of an otherwise highly appealing surface is the necessity of using iCVD to create it. The process takes several hours, and requires access to an iCVD reactor. Furthermore, considering that this research is funded by the ONR with the goal of ultimately being able to reduce the frictional drag of torpedoes, ships and submarines, the current inability to scale iCVD is a major drawback. Currently, coating a 28 mm-diameter cylindrical rotor already necessitates modifications to the reactor to prevent the rotor from interfering with the filament, and anything larger simply would not fit. While the Gleason lab at MIT is investigating drastically scaling up CVD, such technology is certainly not viable in the immediate future.

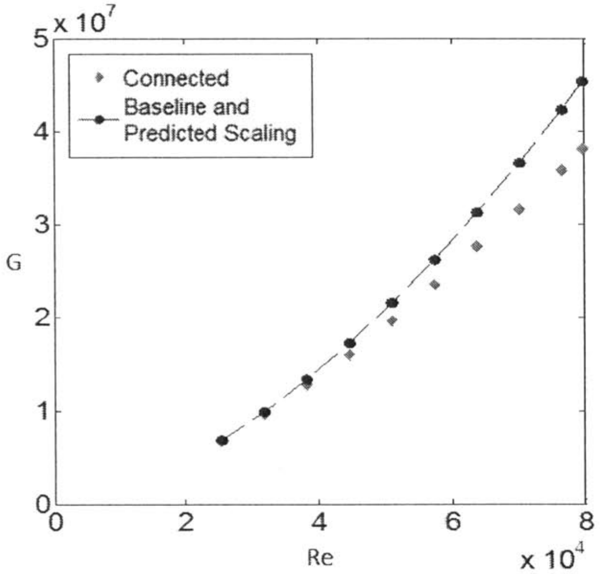

Figure 2.9: Plot of non-dimensional torque vs Reynolds number for DVB-PFDA coating

2.1.3 A Commercially Available Superhydrophobic Coating

NeverWet ™ is a commercially available spray-on superhydrophobic surface. While its exact composition is a trade secret, analysis of the MSDS and our own research seems to indicate that it consists of a silicone-based undercoat and a topcoat of silica nanoparticles. The result is a highly mechanically robust with high contact angles and a structure shown in the SEM image in Figure 2.10.

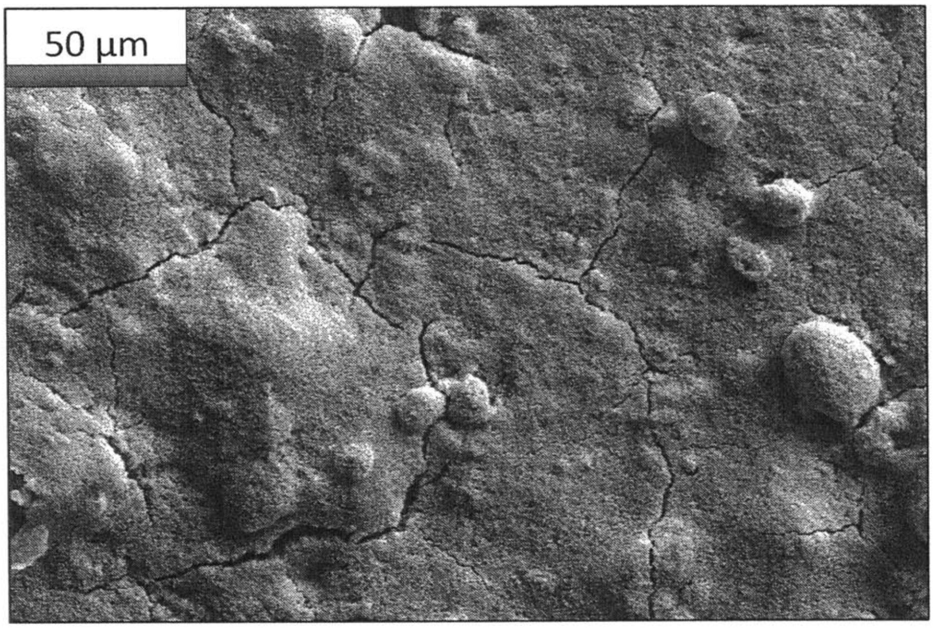

Figure 2.10: SEM of sprayed NeverWet surface showing surface texture

While the structure looks nothing like the successful PMMA-based surfaces, its high contact angles and robustness gave high hopes for good drag reducing performance. At lower Reynolds numbers, but well into the turbulent regime, NeverWet delivers on this promise, providing drag reduction performance superior to that of even PMMA-POSS. However, soon after, the torque curve stops following the expected pattern, and begins to show fluctuation and poor drag reduction. Several repeated runs showed the same artifact. A deeper investigation was made into this phenomenon using high-speed photography, which helped shed light on the issue. Figure 2.11 depicts a still image from one of these videos, and shows a series of instabilities that are occurring in the coating, most likely occurring due to local failures that allow air inside to distort the surface and the plastron.

Figure 2.11: Still image from high-speed video of NeverWet-coated rotor. Local failure of coating causes formation of chevron-like patterns that may be detrimental to drag reduction performance.

2.2 What Makes a Surface Reduce Drag?

Since all the surfaces described above are superhydrophobic to some degree and successfully capture a plastron when submerged in water, their range of drag reducing performance seems to indicate that slip theory alone does not explain why certain surfaces reduce drag better than others. This research arm aims to find out what specific characteristics of a surface are needed for sustainable, robust turbulent drag reduction.

2.2.1 Contact Angles

The importance of the contact angle as a measure of superhydrophobicity was discussed in Section 1.1.2. These contact angles on rough surfaces were measured using goniometry, for each of the surfaces discussed above, as well as two others that were previously investigated by previous students working on the project. These values are listed in Table 2-1.

Surface	**Adv. Contact Angle (°)**	**Rec. Contact Angle (°)**	**Hysteresis (°)**
PMMA-POSS	160.1 ±0.8	160.0±0.4	0.1
PMMA-PFDA	148.5 ± 1.0	147.9 ± 0.9	0.6
DVB-PFDA	154.0± 1.1	150.3° ± 1.6	3.7
NeverWet	152.5 ± 0.7	151.4 ± 0.6	1.1
Supeglue-POSS	165.0 ± 2.8	164.0 ±3.2	1

Table 2-1: Contact angles for the various surfaces that were studied

As superhydrophobicity is essential in maintaining a plastron which then allows for regions of slip, it is expected that high contact angles and low hysteresis must be instrumental in promoting robust drag reduction.

2.2.2 Surface parameters

While equilibrium contact angles are a measure of the resistance of the surface to wetting out, the surface topography is also believed to play a role in the reduction of drag. There are several ways in which the roughness of a random surface can be characterized, summarized in Table 2-2 (Gadelmawla *et al.,* 2002)

Surface Parameter	**Definition**
Root-Mean-Square (RMS)	$RMS = \sqrt{\sum \frac{x_i}{n}}$
Skewness	$S = \frac{1}{nRMS^3} \sum_{i=1}^{n} x_i^3$
Kurtosis	$S = \frac{1}{nRMS^4} \sum_{i=1}^{n} x_i^4$

Table 2-2: Amplitude parameters commonly used to describe the roughness of a random surface.

While some of these definitions appear abstruse, they are all variants of common statistics. A surface is best understood as a data set that reflects the heights at various points, x_i for i = 1,2,...n. As such, statistical analyses can allow us to understand the distribution of the points and make inferences based upon that. The root mean square, for instance, is a measure of the standard deviation of a sampling of points on the surface about the mean height, giving us an idea of the distribution of the height profile. The RMS roughness is in fact one of the most common metrics used to describe a surface, much like the standard deviation is for a data set. However, the RMS roughness is unable to account for additional roughness caused by multiple roughness scales. In

Figure 2.12, the red curve and blue curve have the same RMS roughness, but are likely to feature differing wetting behavior.

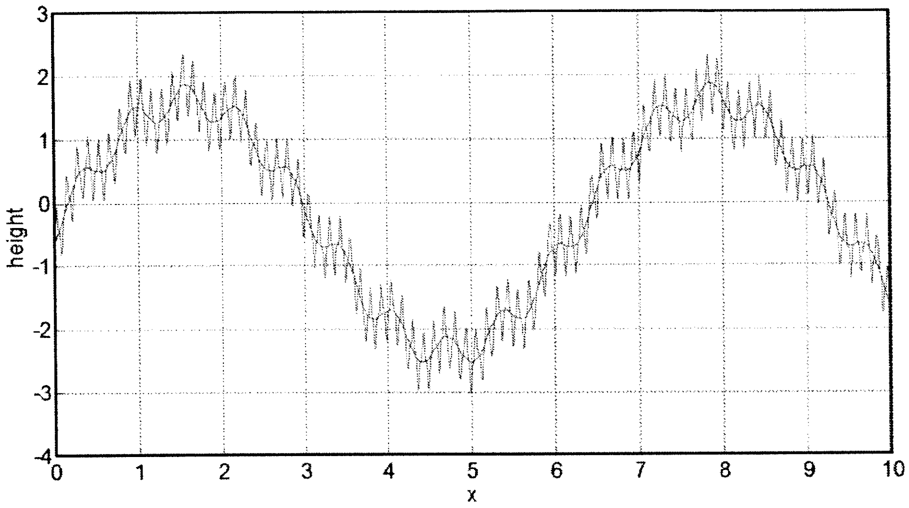

Figure 2.12: A simulated surface created using superimposed sine waves. The red and blue curves have the same RMS value in spite of likely having differing wetting behaviors.

Bottiglione *et al.* posit that there are two other measures that are likely to have a bearing on the ability of a surface to resist wetting: the Hurst exponent (H) and the mean square slope (m_2) (Bottiglione and Carbone, 2013). These paramaters two very different aspects of the surface morphology, and each merits a brief but detailed consideration:

(i) The Hurst Exponent is related to the fractal dimension of a surface, and is therefore a measure of the way in which the surface extends into space. The concept of a fractal surface is driven by the fact that a line (in the 1D case) that features multiple slope changes has a length that is dependent on the length scale of the technique used to measure it. In the truest sense, a fractal surface is thus “infinitely rough” in that every line segment can be spilt into smaller segments. The randomly rough surfaces discussed here are not fully-similar, but due to the multiple length scales that compose their roughness, fractal geometry is an effective way to describe them. For the profile of a surface, a lower fractal (closer to 0 than 1) indicates that the 1D surface extends further into the second dimension. Visually, this is characterized by a surface that seems to feature multiple self-similar scales of roughness. The Hurst Exponent can be extracted from the height profile or a surface using equations (2.1) and (2.2)

$$G(x') = \frac{1}{L}\int [h(x'+x) - h(x)]dx \tag{2.1}$$

$$G(x') \sim \mathrm{x}'^{2H}; x' << \xi \tag{2.2}$$

While Carbone *et al.* found that that that the Hurst exponent does not affect the ability of a surface to sustain a plastron, they worked with surfaces of a Hurst Exponent higher than those that were typical for our surfaces. Furthermore, on an intuitive level, it seemed as if multiple layers of self-similar roughness would make a surface resistant to wetting out. A study was made using the five different drag reducing surfaces, each of which reduced drag to a different degree (measured by slip length). The relationship between the Hurst Exponent, the slip length and the apparent contact angle is plotted in Figure *2.13*.

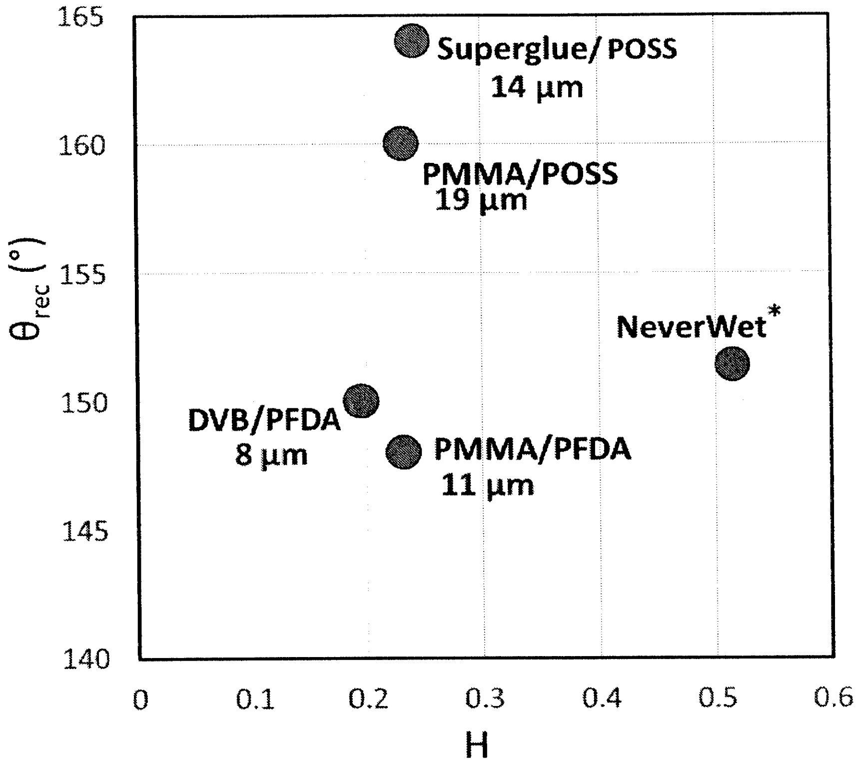

Figure 2.13: Plot of slip length as a function of Contact Angle and Hurst Exponent for five drag-reducing surfaces. The green points indicate surfaces that are robust, able to sustain multiple runs of testing. The orange points represent those that are not.

The data points colored in green represent those surfaces that are robust – they are able to undergo multiple runs of drag reduction testing without losing effectiveness. The red points, however, are less robust, and are unable to withstand more than a single run. NeverWet, it should be noted, is not able to complete a single drag reduction test as it breaks down at high values of Re as discussed in section 2.1.3. It should be noted that contact angle on a rough surface and the Hurst Exponent (which describes the surface) are not entirely unrelated to each other. However, as the graph above shows, nor are they directly correlated; both PMMA-based surfaces feature the same Hurst Exponent, but they do not have the same contact angles because they employ different hydrophobic agents. Similarly, both PFDA-based surfaces have similar contact angles despite having very different Hurst Exponents. In any case, the results of these studies appeared to indicate that the Hurst Exponent was not a key parameter, as concluded by Carbone *et al* in their study of Cassie-Baxter and Wenzel states on fractal surfaces.

(ii) The mean square slope (often abbreviated as m_2) can be described as the mean of square of the slope of the surface. This is defined mathematically in equation (2.3)

$$m_2 = \langle h'^2 \rangle \tag{2.3}$$

A surface with a high value of m_2 can be described a "spiky" – featuring many changes in slope. Carbone *et al.* posit that m_2 is indeed the dominating parameter in ensuring robustness and resistance to wetting, due to changes in surface energy caused by wetting, such that

$$m_2 > \frac{\pi}{2\cos^2\theta_Y} \tag{2.4}$$

Slip length and robustness are plotted as before, but now as a function of m_2 and the contact angle.

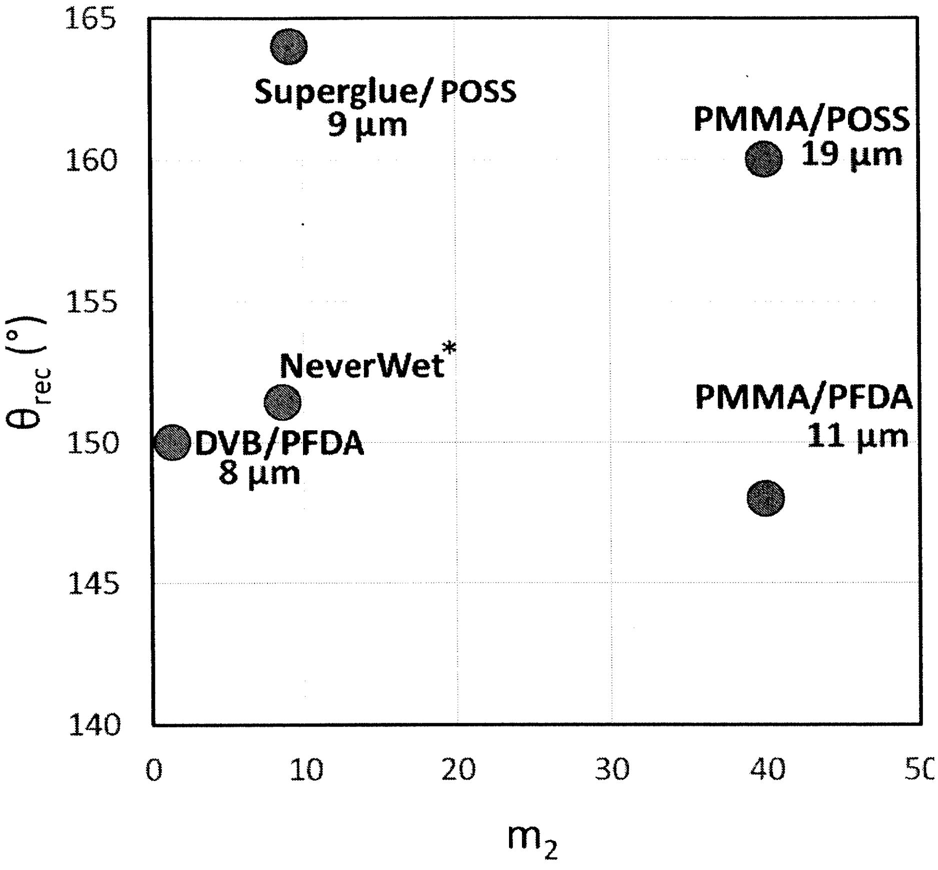

Figure 2.14: Plot of slip length as a function of Contact Angle and mean square slope for five drag-reducing surfaces. The green points indicate surfaces that are robust, able to sustain multiple runs of testing. The orange points represent those that are not.

Figure 2.14 indicates that m_2 affects both the robustness as well as the slip length, with a spikier surface proving more effective at robustly reducing drag.

It should be noted that distinguishing between the RMS, m_2 and H measures is not highly intuitive, and an attempt to elucidate the issue is made in Appendix B. The measured values for these surface roughness parameters are also dependent upon the filtering of the data obtained from profilometry, and this is also discussed in Appendix B.

2.2.3 Obtaining Surface Profiles

In order to calculate the various surface parameters considered here, a height profile of each surface was first required. This could be achieved via confocal microscopy (Wilson, 1990; Srinivasan *et al.*, 2015), but is a time-consuming process. Though the resulting visualizations offer great insight into the wetting behavior, they also feature several gaps in the data that have to be filled via interpolation. An alternative is to use profilometry. As some of the surfaces being considered have very poor mechanical robustness, non-contact profilometry was used. The Tuteja group at the University of Michigan used their Olympus LEXT OLS4100 laser profilometer to provide us with height-maps with a resolution of 1.25 microns in each direction, and these were used to perform all calculations presented above.

2.3 Moving Forward: Optimizing Superhydrophobic Surfaces for Robust Drag Reduction

Given that the contact angle and the mean square slope (m_2) both seem to be responsible for creating robust drag reduction, it follows that future attempts at creating a drag reducing surface should seek to optimize these two values. Optimizing m_2, in particular, is dependent on the method being used to generate the rough micro-structure. Controlling the surface morphology is no doubt possible using techniques such as iCVD, but since the most successful surfaces that were considered in this manuscript were call created by spraying, means of altering the geometry of sprayed surfaces will be considered.

(i) Nozzle type. Currently, all successful structures (both Superglue and PMMA) were sprayed in a volatile solvent through a two-fluid nozzle. Nitrogen gas used to break the solvent into droplets, which are then ejected from the nozzle. However kinds of nozzles may lead to different results. Using an ultrasonic nozzle, for example, would result in a smaller droplet size in the solvent, leading to a different surface. This kind of nozzle vibrate the nozzle head at a high frequency, causing the liquid inside to break into droplets due to the creation of standing capillary waves in it (Sono-tek) Initial talks were held with two different companies (Sono-tek and Sonaer) that make ultrasonic nozzles, and while spray rates and frequencies were identified that seemed to yield satisfactory results, sample transport made it difficult for the author to obtain and analyze a sprayed sample to ascertain an m_2 value. We were provided with an SEM image of the surface, shown in Figure 2.15 but this was not sufficient to obtain the values for the surface parameters. The fact that the particles seem to be smaller seems to indicate that the ultrasonic nozzle could lead to surfaces that feature smaller length scales and are more robust. However, given that such a nozzle would be a significant investment, it is important that this be verified prior to a purchase.

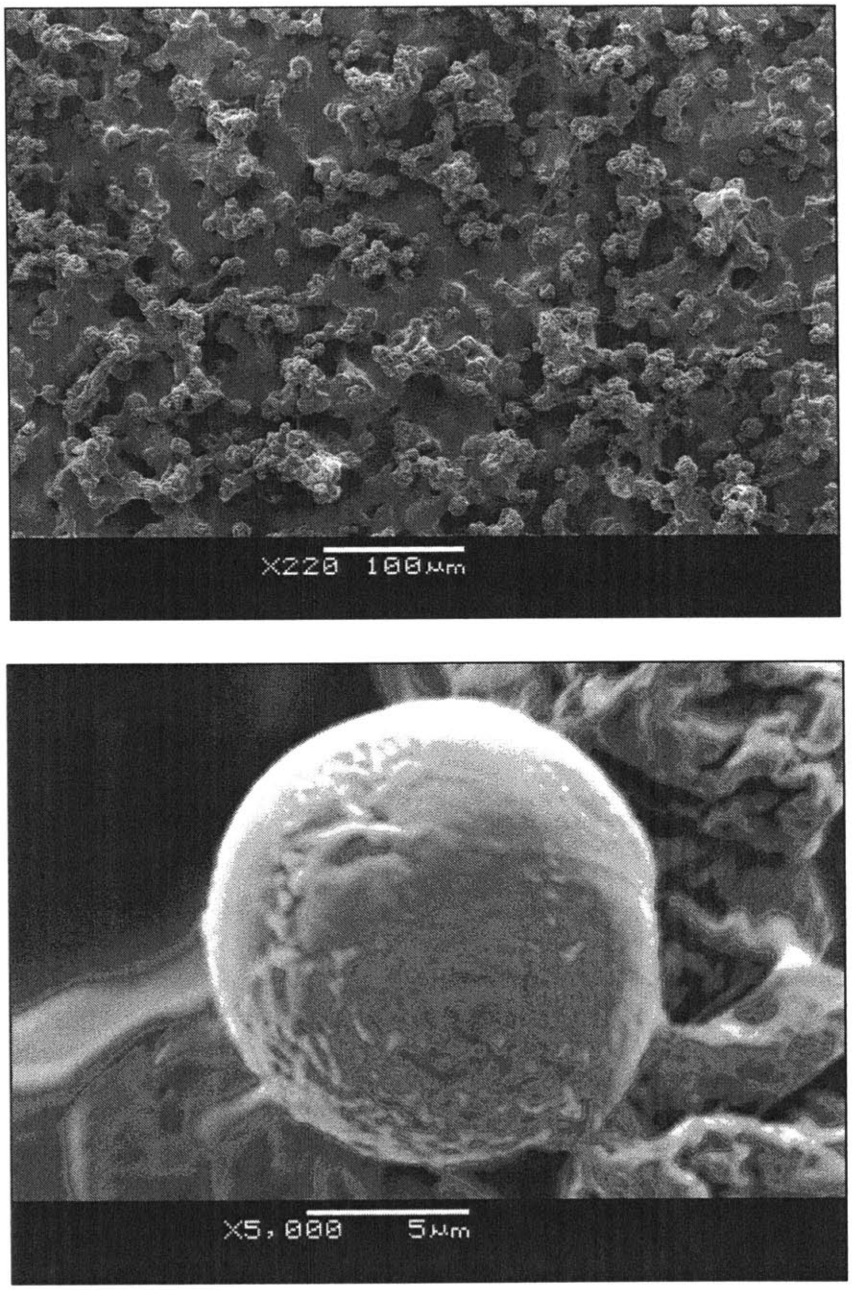

Figure 2.15: PMMA-POSS sprayed using an ultrasonic nozzle

(ii) Nozzle parameters. If future surfaces are to continue with the tried-and-tested method of spraying with a gas nozzle, there are still several parameters that can be varied. Chief among these are the pressure of the gas (in this case Nitrogen), and the height of the nozzle above the substrate.

Both of these vary the amount of time required for the solution to travel from the outlet of the nozzle to the substrate. Spraying at too a high pressure or bringing the substrate too close results in partial evaporation of the solvent, and results in a non-rough surface. However, allowing too much time of flight results in the spray spreading out too much, causing much of the solution being lost. Varying the gas pressure also affect the nature of breakup of the drops.

(iii) Heat Treatment. This is generally carried out after spraying, and is used predominantly on PMMA-based coatings. Heating the sprayed substrate is placed in an oven at 85°C for approximately 8 hours. While this is below the glass transition temperature of PMMA ($T_g = 108°C$), the heat causes the PMMA to flow and re-arrange, and causes the POSS to bloom to the surface (Srinivasan *et al.*, 2013). However, varying the time and temperature will cause the surface to flow more or less, and this will certainly have a bearing on the surface morphology and the value of m_2. It seems likely that a longer heating time, or heating a higher temperature would cause the surface roughness to decrease, and this would lead to m_2 decreasing, too. However, this must be confirmed experimentally, and a balance must be struck between maintaining a high value of m_2 and allowing the POSS to bloom to the surface.

2.3.1 Polyurethane and Abrasion

While the term "robust" has largely been used thus far to describe surfaces that are able to resist wetting out, there exists a second kind of robustness, of the mechanical variety. Mechanical robustness refers to the ability of a coating to resistance being abraded or sheared off the surface, and the vast majority of coating discussed thus far fare very poorly by this metric. Anything PMMA-based is severely damaged by the slightest touch of a solid object. The DVB-PFDA coating made using iCVD and NeverWet are significantly better, but nonetheless can be damaged quite easily, and also are not robust to wetting out. Collaborators of the author at the Tuteja Lab at the University of Michigan are developing a coating that seeks to remedy this. The surface roughness is derived from sprayed polyurethane, while F10POSS is once again used to confer chemical hydrophobicity on the surface. High contact angles with low hysteresis were achieved, along with a surface that has to be soaked in acetone and vigorously scraped to be removed. In order to vary the surface properties, the surface is abraded using a grinder Thus far, drag reduction has been inconsistent and difficult to achieve.

The data suggests that the surface is wetting out, and indeed, the rotor always emerged wet following the experiments. However, running it at lower values of Re seem to yield better results, which makes it seem likely that robustness towards wetting is lacking.

From the studies above, it seems that a higher value of m_2 is required. A systematic study of the value of m_2 as a function of abrasion cycles is presented in Figure 2.16.

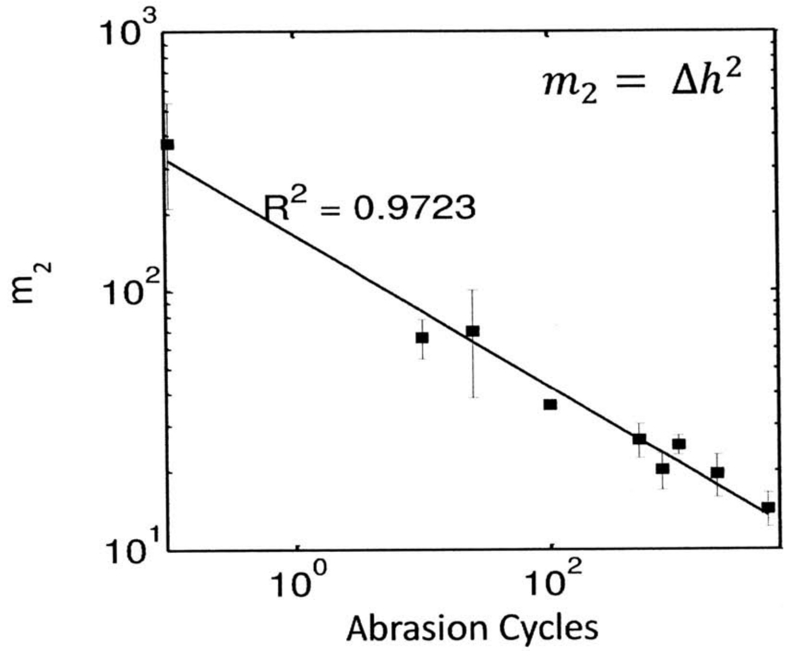

Figure 2.16: Plot showing mean square slop as a function of abrasion cycles for Polyurethane surface.

The first data point at 0 abrasions is likely due to remnant flakes of polyurethane after the spraying process, and it is important to remove these. However, after that, the value of m_2 seems to reduce linearly with abrasion cycles. Applying our findings above would seem to indicate that it is important to remain under 100 cycles of abrasion before the surface's ability to resist wetting out becomes highly compromised. This information has since been shared with the collaborators, and the information will hopefully be used to create the ultimate surface: one that is robustly superhydrophobic and reduces drag by large amount will maintaining its mechanical robustness.

Chapter 3 : Active Drag Reduction – Conception, System Design and Fabrication

3.1 The Need for Active Plastron Generation

Thus far, the drag reduction techniques discussed have been passive. Once the superhydrophobic surface has been made, it simply needs to be submerged from air to water in order to form a plastron. The immersed fluid slips on these regions and no power input is required. We have demonstrated that this approach has successfully reduced friction drag, it has several inherent disadvantages. Firstly, the resistance to wetting tends to be low. PMMA-POSS and others are able to withstand the pressure fluctuations caused by turbulence (Srinivasan, 2015) but larger imposed pressure gradients will cause the surface to wet out. In the intended application setting, *e.g.* large naval bodies immersed in water, such fluctuations are bound to occur. Furthermore, since the plastron is initially created during the submersion process as the textured surface locally traps air pockets, once the plastron is destroyed, there is no way to replenish it without recoating the object or obtaining additional air through some other means. Finally, over large time scales, the trapped air has been shown to diffuse out, causing gradual and irreversible wetting of the surface (Xu *et al.*, 2014).

In order to tackle these shortcomings, I investigate an approach that seeks to improve the robustness to wetting, and provide the ability to replenish the plastron. This calls for a radical departure from the work discussed thus far as it employs a totally different mechanism from superhydrophobic drag reduction. The term "plastron" itself may no longer apply as the gas film is replaced by water vapor, is continuous and requires a power input to create and sustain. A superhydrophobic surface is not strictly required to achieve this steam film, but a useful property of these surfaces described below allows for a considerable reduction in the energy input required to create and sustain them.

Drag reduction using a Leidenfrost film is not a novel concept; it has been recently studied by dropping heated spheres through water (Vakarelski *et al.*, 2011) and measuring the terminal velocity of the sphere as a way of assessing changes in the frictional drag. These studies observed approximately 85% drag reduction, but were unable to separate the contribution of form drag from skin friction reduction.

In this Chapter, which forms the bulk of the thesis, I discuss the process by which these surfaces are made, and explore a bespoke apparatus that I designed and fabricated to study active film generation.

3.2 The Leidenfrost Effect and Film Boiling

In order to understand the mechanism by which a steam film can be generated, we begin by studying the boiling curve of water, presented in Figure 3.1.

These curves are generated by placing a drop of water upon a heated plate and increasing the temperature of the plate. The independent axis measures the wall superheat – the temperature of the plate above the saturation point of water. At standard conditions (1 atm), the saturation temperature is 100 °C, and so the x-axis values can be converted to absolute temperature values by adding 100 °C to them. In the initial part of the curve, the heat flux unsurprisingly increases along with the wall superheat. The increased temperature gradient aids both conduction and convection. In these regimes, the water initially boils by natural convection, before moving to nucleate boiling, characterized by the formation of bubbles on the boiling surface (Bergman, 2011).

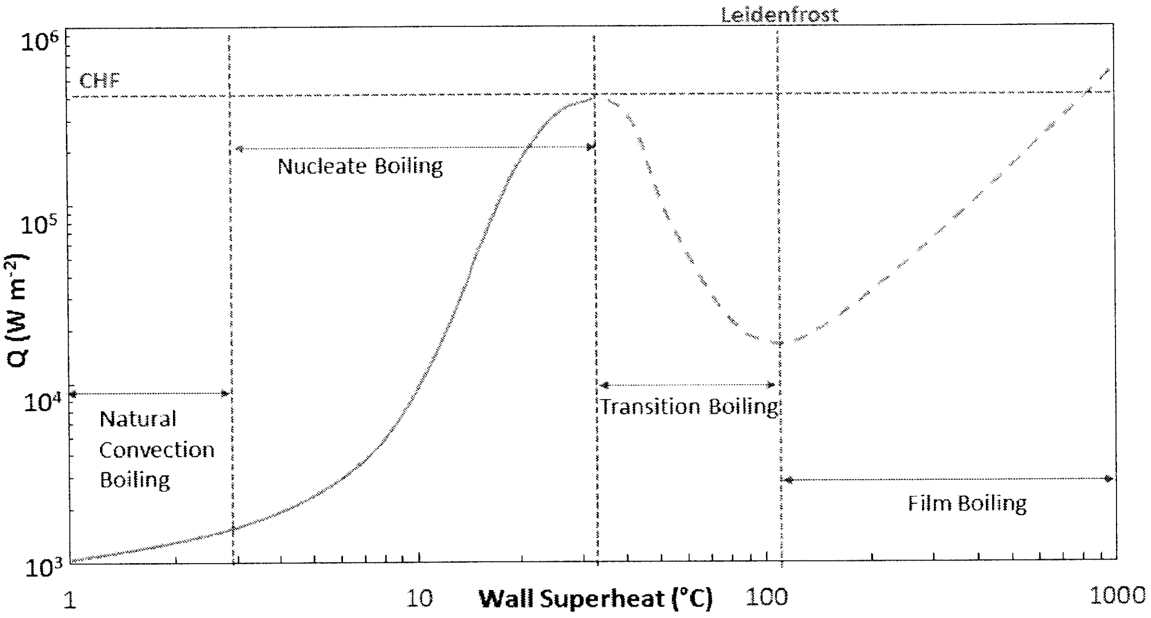

Figure 3.1: Boiling curve for water on a smooth, heated metal surface. The wall superheat is the temperature of the surface above the boiling point of water.

At a certain value of the wall superheat however, the heat flux reaches a local maximum known as the critical heat flux (CHF). If the temperature of the body is controlled and is increased, the heat flux decreases. This unexpected change is caused by enhanced local evaporative boiling occurring on the bottom of the droplet, forming a layer of vapor. This steam film lies in between the droplet and the heated surface, acting as an insulating barrier and hindering further heat transfer. During this transition boiling phase, the steam film gradually grows, providing insulation until it reaches its maximum thickness and becomes continuous, completely enveloping the surface. The heat flux is at a local minimum at this point, and the absolute temperature is known as the Leidenfrost temperature. The lifetime of the droplet is longest at this point (Leidenfrost, 1756).

If the temperature is further increased beyond this point, the thickness of the steam film is now fixed and so the heat flux once again increases. This regime is known as film boiling, and the droplet is entirely insulated from the heated surface by the layer of steam. For metals such as steel and aluminum, the Leidenfrost temperature occurs in the vicinity of 200-300°C (Bernardin and Mudawar, 2010.)

Using a superhydrophobic surface such as those discussed in Chapter 2 can drastically reduce the values of the Leidenfrost temperature and heat flux (O'Hanley *et al.*, 2013), resulting in a boiling curve like that shown in Figure 3.2. The nucleate boiling and transition boiling regimes are shortened considerably, while the CHF and Leidenfrost temperatures are significantly decreased (Vakarelski *et al.*, 2012). Indeed, a later discussion of the surfaces used in this manuscript to promote low-temperature

Leidenfrost vapors finds that our surfaces do not visibly nucleate at all, and have a Leidenfrost Temperature barely above 100°C.

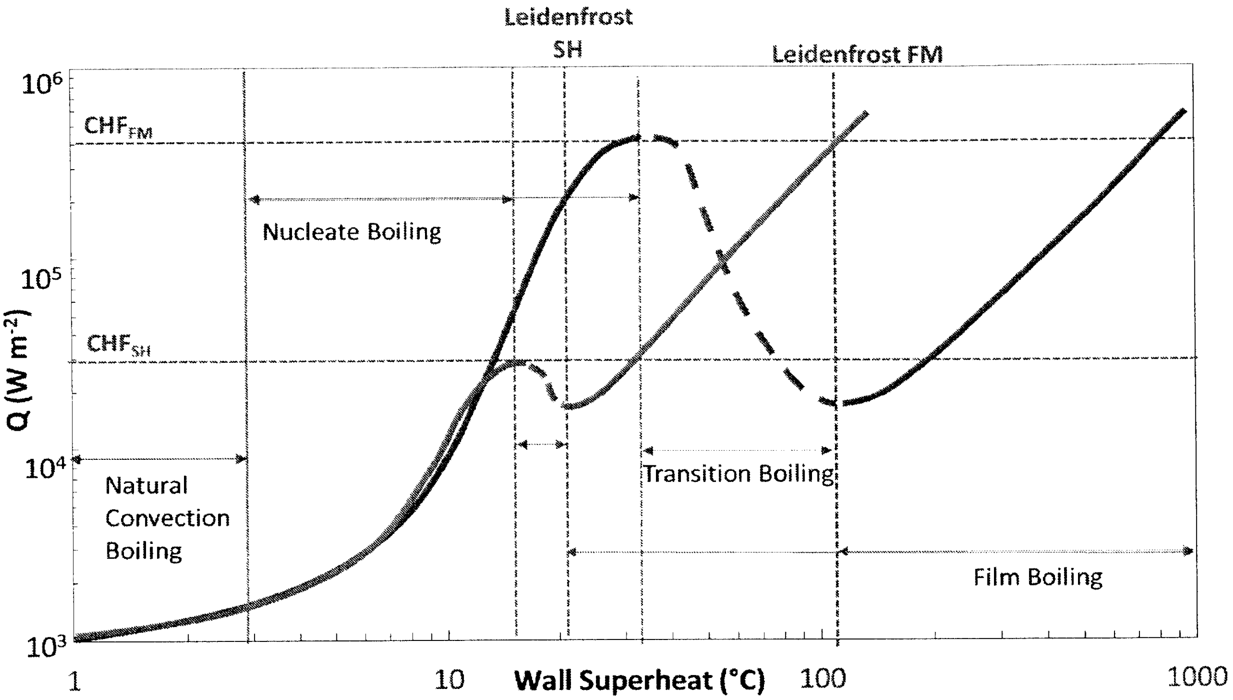

Figure 3.2: Boiling curves of water on a flat metal (FM) surface (blue) and a superhydrophobic (SH) surface (orange). The latter features a decrease in both the critical heat flux and the Leidenfrost temperature.

3.3 Design and Fabrication of an Apparatus to Measure Drag Reduction

The fact that Srinivasan *et al.* had already developed a method and the apparatus to measure a reduction in skin drag meant that it was logical to build off their success and modify their equipment and approach, rather than develop a new system from the ground up. As noted earlier, they combined a bespoke wide-gap Taylor-Couette cell with a rheometer to measure the torque required to impose a steady rotation rate upon a superhydrophobic rotor. They then compared this value to the torque required to produce the same rotation rate from a regular (non-superhydrophobic) rotor, and used the difference between the two to compute the drag reduction, arising from the superhydrophobic coating. Measuring the drag reduction caused by low-temperature film boiling called for a largely similar methodology. The wide-gap TC geometry that allows for high Reynolds number could still be used, and a rheometer could be used to measure the different torques that a film boiling and a non-film boiling rotor require to achieve the same rotation rate.

The entirety of the challenge lay in achieving continuous film boiling on the rotor. O'Hanley *et al.* developed porous superhydrophobic surfaces with Critical Heat Fluxes on the order of 30 kW m^{-2}. Using the same couette rotor geometry used by Srinivasan *et al.* in the study of passive superhydrophobic surfaces, and assuming that the water temperature is 90°C and the rotor is at 110°C, this translates to a power requirement of approximately 220 W (the calculation is based on a rotor surface area of 0.0037 m^2). The proposed apparatus had to be modified to provide at least this amount of thermal power to heat up the rotor and allow it to sustain film boiling.

In itself, providing 220 W to a body is of no difficulty; the complication arises from the fact that the body is rotating rapidly, at speeds of at least 3000 rpm in order to achieve turbulence. Furthermore, the proposed method of quantifying drag reduction involves a highly precise measurement of the frictional torque supplied by the rheometer. As such, any method of power delivery that adds friction to the system will distort the torque signal recorded by the rheometer and hence prevent accurate measure of drag reduction. *The crux of the research objective can ultimately be summarized as the search for a method to provide thermal power to a rotating body while exerting a minimal and noise-free torque upon it.* Several different options were considered towards achieving this goal, and these are discussed below:

(i) Embedding a heater in the rotor, and powering it by using the rotating rotor as an electrical generator. This approach would see the placement of a coil of wire about the rotor. A magnetic field would need to be provided, and the spinning coil would rotate in this field, generating a current; this is effectively a rudimentary generator.

However, while there is no mechanical friction being exerted upon the rotor, the generation of current will cause a Lorentz force, resulting in a back torque which counteracts the rotation of the rotor. The rheometer will now measure the torque of the rotor spinning in water as well as the back torque, a noisy signal which could obfuscate the anticipated change in the torque measurement. This same process is exploited in magnetic braking, where eddy currents are negated in the moving piece of metal. However, in the present case, they are detrimental to the objective.

(ii) Inductive heating. In a process similar to the generator, the spinning rotor interacts with a magnetic field to induce a current. However, where the former features a coil in which the current is induced, the latter causes eddy current generated in the rotor itself to heat it. This approach involves directly heating the rotor rather than using a heater, and this is a drawback in that there is no theoretical upper bound to the amount of heat that can be generated, leading to the possibility of irreversible damage. Furthermore, the induced current will once again create a back torque, which will result in a noisy torque measurement at the rheometer.

(iii) Commutators/Slip rings. The most common solution in industry to the challenge of supplying current to a rotating shaft, slip rings are used in DC motors. A schematic is shown in Figure 3.3.

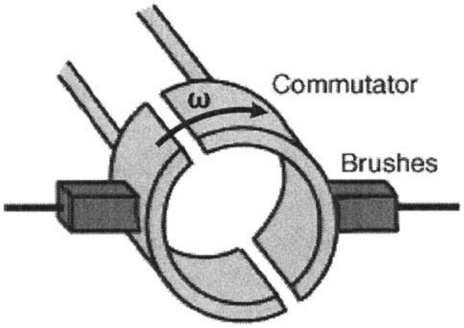

Figure 3.3: Schematic of a slip ring used to transmit current to a rotating body (commutator). The commutator would be replaced by the rotor in the Taylor-Couette setup

Carbon brushes are used to transmit the current from an external power source to the rotating commutator, but these were found to exert too much torque on the rotor. Several industrial slip rings were considered, but none provided less than 1 mN.m in friction torque, on the same order of magnitude as the expected measurements. While such a large friction torque is undesirable, it can nevertheless be subtracted from the torque measured at the rheometer leaving the hydrodynamic torque – provided it is of sufficiently low noise. However, the ball bearings in the slip rings cause the maximum noise in the torque to be of the same order of magnitude as the torque itself, which will obfuscate any measured drag reduction (from discussions with the slip rings manufacturer Orbex).

One potential alternative was to use mercury-based slip rings, but these are not sold with a through bore. They need to be affixed the top or the bottom of the rotating shaft, which is not possible in this setup, as the bottom of the rotor is immersed in water, and the top is contained inside the rheometer.

(iv) Liquid metal conductor. A unique solution devised for this project, it consists of using a liquid metal to provide current to a cartridge heater embedded in the rotor. The two leads of the cartridge heater protrude from the rotor, and each of them is dipped into a dish of liquid metal, one attached to the positive terminal of a power supply and one to the negative. As the rotor rotates, the wires are pulled through the liquid metal, maintaining electrical contact even as they move, and providing power to the heater. This is shown schematically in Figure 3.4.

In contrast to the three options considered above, using liquid metal contacts are an unproven technology with no industrial application and a lack of extensive literature. Accordingly, while it was potentially a low-torque method of sending power to a rotating shaft, this had to be verified via experiments and a substantial part of the research focus was devoted to this.

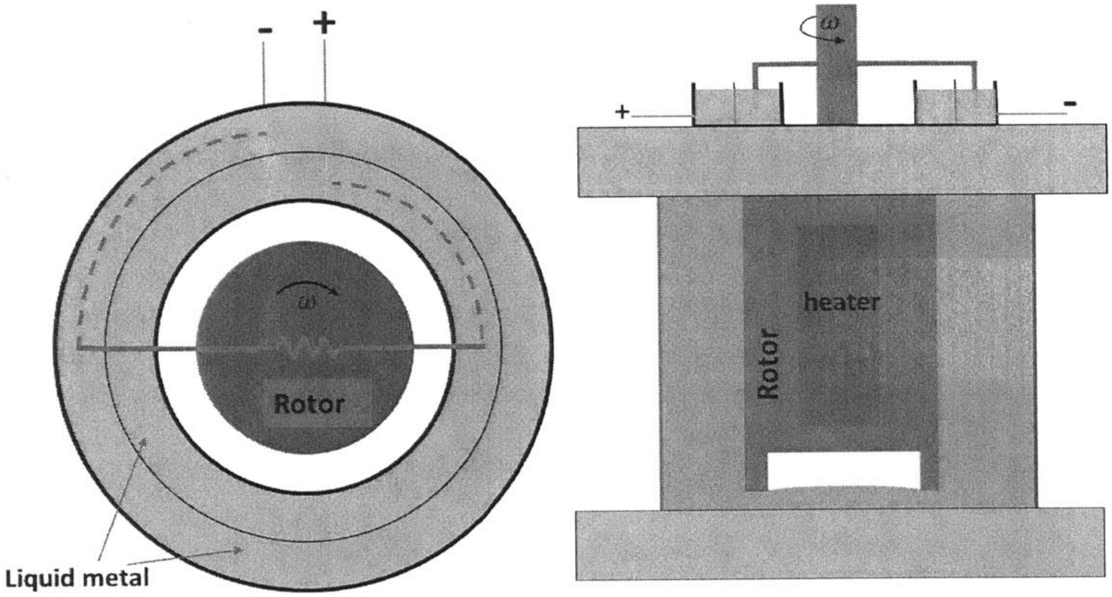

Figure 3.4: Setup of liquid metal contact system. Top View (L) shows the electrical connection under rotation. The heater is modeled as a resistor. Front view (R) is the full setup, including the Taylor-Couette cell and the rotor with the heater embedded inside it.

3.3.1 Proving the Viability of Gallium Eutectic as a Liquid Metal Contact

Mercury is the only metal that exists as a liquid at room temperature in its elemental form. However, the toxicity and health hazards posed by mercury are well understood (Vallee and Ulmer, 1972) and as such it is an undesirable material to work with. A second metallic element, gallium, is a liquid at 35°C and has few of the risks associated with mercury (Domingo and Corbella, 1996). The high melting point could be mitigated by carrying out all experiments in controlled conditions at a higher temperature, but a simpler solution was to dope the Gallium with Tin and Indium (Ga 68.5%/In 21.5%/Sn 10% by weight), reducing the melting point to -19°C. As this gallium eutectic is readily purchasable (GalliumSource), the latter solution was adopted.

It is worth noting that the possibility of using a conductive salt solution was also considered; however, the likelihood of this approach succeeding was always limited as the conductivity of a salt solution is typically 5 orders of magnitude lower than that of a liquid metal (Weast, 1989; Wolf, 1966.; Engineering Toolbox). A brief experiment proved this; the electrolysis of saturated salt water, one of the most conductive electrolytes, with 120 volts and 2A resulted in the water heating to its boiling point and boiling off. Furthermore, one product of the electrolysis process is highly toxic and corrosive chlorine gas. While this could be mitigated by using a different electrolyte, many of these are highly concentrated acids, which would inevitably result in other complications and safety hazards. The viscosities and conductivities of the gallium eutectic, mercury and sodium chloride solution (saturated) are tabulated below:

	Mercury	Gallium-Indium-Tin Eutectic	Saturated NaCl (aq)
Viscosity (Pa.s)	1.5×10^{-3}	2.4×10^{-3}	1.9×10^{-3}
Conductivity (S/m)	1.0×10^{7}	3.5×10^{6}	22.6

Table 3-1: Dynamic viscosities and conductivities at standard conditions for mercury, gallium-indium-tin eutectic and saturated common salt solution.

While the low resistance of the gallium eutectic theoretically would allow it to carry 2A at 120V without heating losses, there is not enough literature on the subject to rule out other possible effects such as rapid oxidation of the gallium. As such, an experiment was designed to verify this; the apparatus consisted of a 3-D printed ABS holder with two separate gallium eutectic chambers and 4 openings (2 per chamber). A variable transformer, or Variac, was used to provide a variable voltage between 0 and 140 volts, and copper leads from its terminals were inserted into each chamber. As the two chambers were as of yet electrically isolated, no current could flow. Subsequently, a copper wire bent into a horseshoe shape was inserted with each end in one of the remaining two openings, electrically connecting the two gallium eutectic chambers. A current now flowed; the resistance in the circuit was measured and found to remain at 1.3 Ω even after several minutes at 2A. There was no noticeable oxidation; following the experiment, the top layer of oxide was disturbed, and the gallium immediately beneath remained unoxidized. Figure 3.5 depicts this experimental setup.

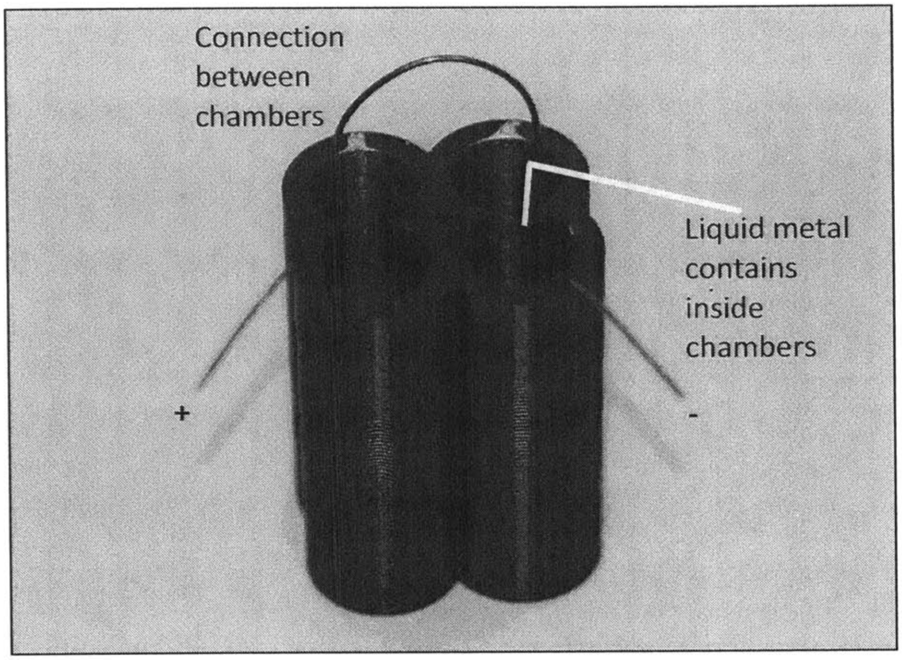

Figure 3.5: Image of the apparatus used to verify the behavior of gallium while conducting high currents. The two chambers contain the liquid metal, and are electrically connected by the bent orange wire. The other two wires carry current to and from the liquid gallium eutectic chambers.

Having confirmed that the gallium eutectic could handle high currents for several minutes with no apparent consequences or changes in properties, it now had to be ascertained whether it could sustain a good electrical contact with a wire being dragged through it at high speed. The formation of the non-conductive gallium oxide film posed a risk in that it could electrically insulate the wire from the eutectic. Furthermore, if the wire is modeled as being wetted to the eutectic and is pulling it away from the whole, the force of the wire pulling the wetted eutectic is opposed by the surface tension of the liquid metal. The relative size of each of these forces can be compared using a modified

Bond number as the appropriate dimensionless group. However, in practice, the surface tension between the eutectic and copper wire is difficult to ascertain, and experimental verification was required. In order to achieve this, a new apparatus was built, that would prove to be precursor of the final system. The eutectic was now housed in a dish containing two concentric slots. A DC motor capable of speeds up to 10,000 rpm was suspended over the center of this dish. Press fit to the shaft of the motor was an aluminum cylinder 0.7" in diameter and 0.8" in length, and around it was a laser cut piece of acrylic that served to hold a single copper wire with bared ends in place, with the two ends falling downwards into the eutectic-filled slots, as pictured in Figure 3.6.

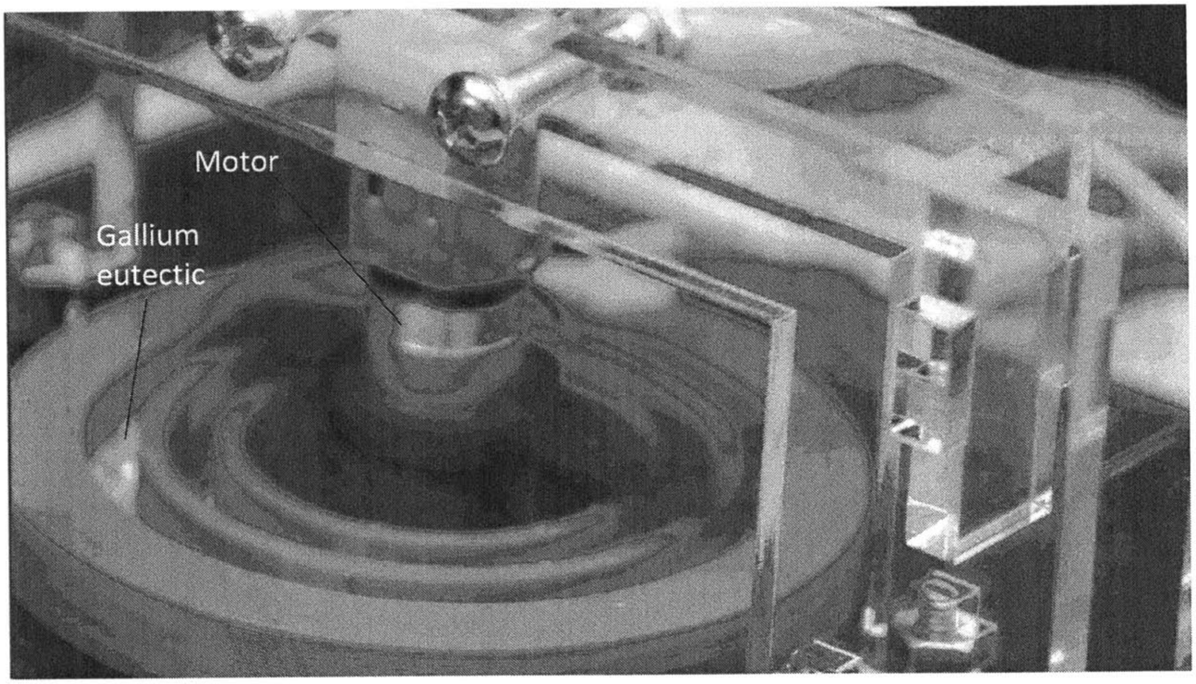

Figure 3.6: Apparatus to test the conductivity of gallium with rotating wires. The green acrylic piece houses a wire that electircally connects the two circular liquid metal dishes. The acrylic piece is mounted to an aluminum rotor that is spun by a motor.

The ABS dish and the eutectic liquid metal that it contains remain stationary throughout the experiment, while the motor plus the attached shaft and wires spin. A wire is dipped to each of the eutectic dishes, and is connected to an Ohmmeter. Thus, only if the wire ends remain in electrical contact with the eutectic will the Ohmmeter indicate a closed circuit; if the contact is broken, it will indicate an open circuit. When the test began, the circuit was closed, and the rate of rotation of the motor was gradually increased, peaking at around 6,000 rpm, considerably above the 2,500 rpm that the rheometer is capable of. Promisingly, at no point did the contact break, in spite of the high rotation rates and the gradual oxidation of the gallium, proving that the liquid metal could indeed maintain electrical contact with the rapidly rotating electrode wires.

3.3.2 Challenges Associated with Using Liquid Gallium Eutectic

In spite of its many useful properties, there were two key challenges to using liquid gallium eutectic as a conductor.

(i) Oxidation. When exposed to air, gallium forms a thin film of gallium oxide over its surface, much like that of aluminum. Unlike the liquid metal, this oxide film is solid and non-conductive. The gallium below the layer remains unoxidized and in the liquid state. However, the constant motion of the wires through the gallium effectively churns it, causing fresh liquid metal to be exposed to air, resulting in much of the gallium getting oxidized. The oxidation is undesirable for several reasons. Being non-conductive, it interferes with the electrical contact. Secondly, the presence of a flaky solid that covers the liquid serves to effectively enhance the apparent viscosity of the liquid metal. The torque required to pull the wire through the gallium dramatically increases, as does the noise in the torque signal. It is possible that the torque exerted by the gallium on the wires changes in the middle of an experiment. This occurs most often when a surge of current is passed through it. Since a variac is effectively an autotransformer, suddenly decreasing the voltage being put through the gallium causes a transient current spike, and this leads to massive oxidation in the gallium. Care is therefore required with ramping the voltage up and down; the ramping process needs to be gradual.

(ii) Corrosion. Gallium is corrosive on some level to most metals (Down, 2013) and gallium-infused aluminum reacts violently with water to form hydrogen gas (Czech, Troczynski, 2010). The fact that the couette cell was made of non-anodized aluminum naturally made avoiding a gallium spill of great importance. In spite of the precautions taken, a minor spill occurred, and the consequences of this, as well as safety measures taken to prevent a repeat occurrence, are discussed further ahead.

3.3.3 Rotor Design and Material Selection

Using the same methodology and Taylor-Couette cell as Srinivasan *et al.* fixed the geometry of the rotor. Doing so meant that the relationship between angular velocity and Reynolds number would remain the same for these experiments vis-à-vis those of Srinivasan *et al*. However, beyond the basic dimensions of the rotor, the vast majority of it had to be changed. The rotors used by Srinivasan *et al.*, manufactured by TA Instruments, were made entirely out of stainless steel, and coupled directly to the rheometer via a stem made of the same metal, as shown in the images in Figure 3.7 and Figure 3.8.

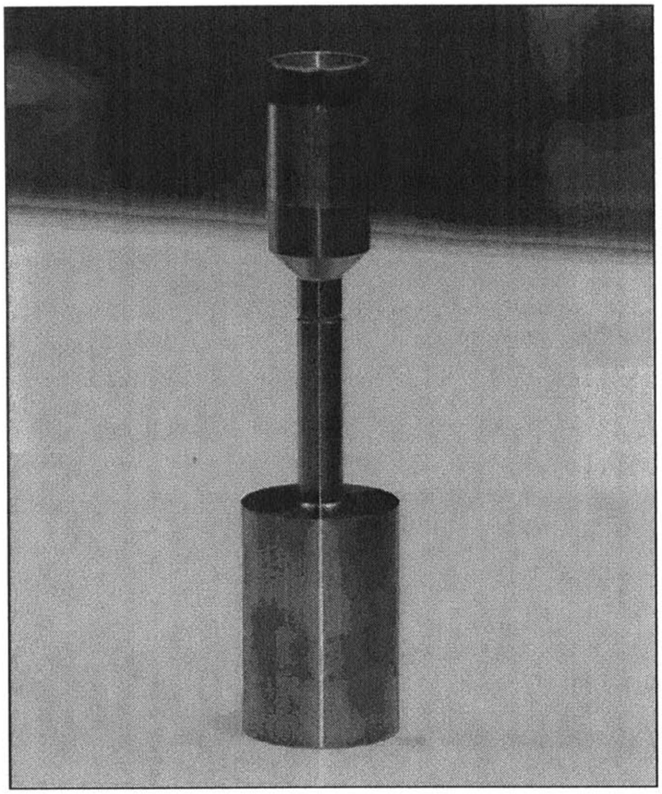

Figure 3.7: Front view of a stainless steel TA recessed-end rotor. The top part interfaces with the AR-G2, and features a magnetic strip (black) for automatic recognition by instrument.

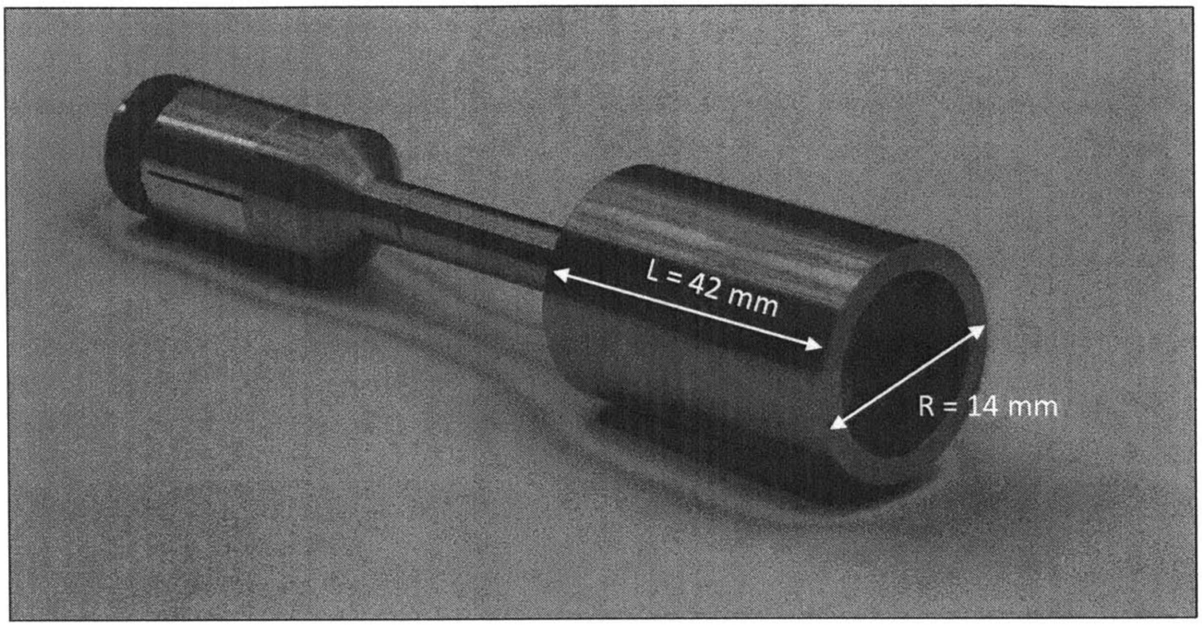

Figure 3.8: A prone TA stainless steel rotor. The visible recessed end eliminates end effects by trapping a bubble of air.

These rotors, while hollow, offer no access to their interior, which would be required to house the cartridge heater. Where the TA rotors are made of steel, the authors of this manuscript opted for Aluminum for the film boiling rotor. This decision was based on the fact that a uniform temperature was desired across the length and the diameter of the rotor, allowing for the assumption of a lumped parameter system. When the rotor is submerged in water which is film boiling around it, there are two primary modes of heat transfer:

(i) The embedded cartridge heater is transferring heat to the rotor by conduction

(ii) The rotor is transferring heat to the water by convection across the boiling film.

In order for the rotor to have a uniform temperature across both its diameter and length, the conduction mode of heat transfer must be larger than the convection. The relevant non-dimensional number that reflects this is the Biot number, defined in equation 3.1.

$$Bi = \frac{hL_C}{k_b} \tag{3.1}$$

In order to assume a lumped parameter system with uniform temperature, the Biot number must be $Bi < 0.1$, and this can be done by increasing the conductive heat transfer rate. Aluminum is a better thermal conductor than stainless steel, making it a better option. Furthermore, while the specific heat capacity of aluminum is higher than that of steel of a per-mass basis, the added density of steel makes it have a high specific heat capacity on a per-volume basis, which is the more pertinent measure. Therefore, selecting aluminum would also lead to a system that responded more quickly and uniformly to temperature input changes.

A second challenge lay in the fact that the entire TA rotor, including the stem, is made of thermally conductive metal which would lead to the heat being conducted to the rheometer. The sensitive nature of the measurements that a rheometer must take and the high precision that it must employ make any exposure to heat a risky proposition, creating the necessity for the stem of the rotor to be made from an insulator. A plethora of options would satisfy this requirement, but relatively few are also machinable to a high degree of precision, and are able to withstand a temperature of at least 150°C. The possibilities initially numbered two:

(i) High-temperature plastics such as Delrin. A commercially-sold variant of Polyoxymethylene (POM), Delrin is readily purchasable and is commonly used in a multitude of applications (Read & Williams, 1961). It is highly machinable, and can easily be formed into shapes. Delrin melts at 176°C, which is adequate, though close to the estimated maximum operating temperature of 150°C. A machined Delrin stem is pictured in Figure 3.11 , on the left.

(ii) Mykroy/Mycalex, a machinable ceramic. Like most ceramics, Mycalex is very hard, brittle, has an extremely high melting point of over 500°C, and is a highly effective electrical and thermal insulator (Crystexllc.com). However, the fact that it is machinable sets it apart from most other ceramics, most of which are too brittle. In practice, machining this ceramic was far from a simple proposition; the extreme hardness of the material made selecting spindle speeds and feed rates difficult and a matter of trial and error, even with carbide tooling. Furthermore, tool deflection was substantial, and made turning diameters and boring holes precisely a time-consuming process, requiring very low rates of material removal and measurements after virtually every pass. The material itself and the setup are pictured in Figure 3.9 and Figure 3.10.

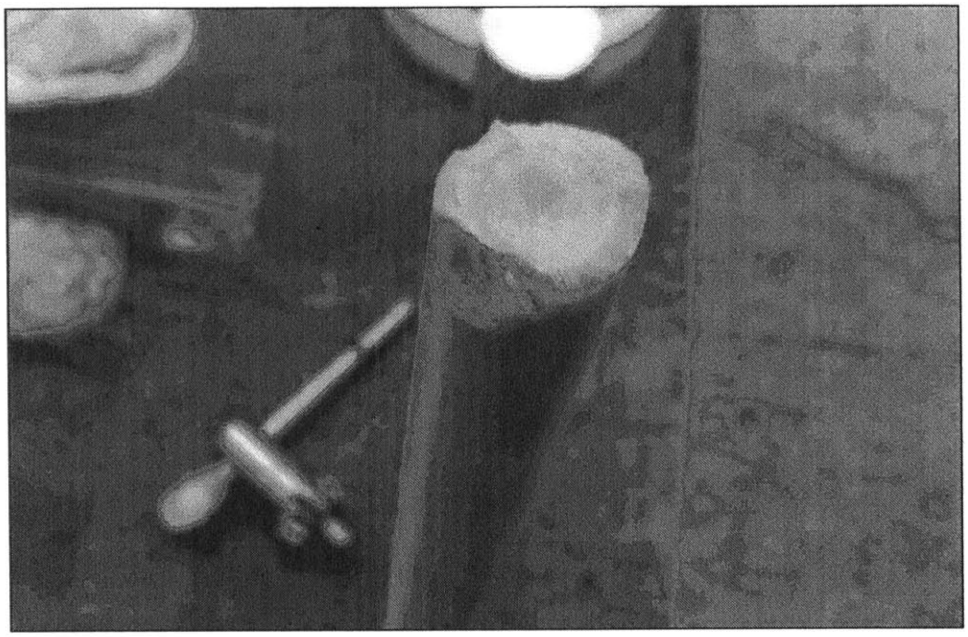

Figure 3.9: Fractured Mycalex rod

Figure 3.10: Turning a Mycalex rod in a lathe. Note the use of a live center to prevent wobble and tool deflection.

Ultimately, it was found that neither Delrin nor Mycalex was the optimal choice, as they both were too far on either side of the spectrum of thermal expansion. The parts of these stems which couple to the aluminum rotor would be at 150°C. Both the stem and the rotor would expand, and if the expansion rates are very different, the press fit that couples them would be affected. Delrin's coefficient of linear expansion is between 8.46 and 21.96 x10^{-5} m/m/K, (McMaster.com) five to ten times that of aluminum (22 x10^{-6} m/m/K), leading to the press fit failing and the aluminum rotor falling off the stem by action of gravity at high temperature. The ceramic meanwhile, barely expanded with a COE of just 9x10^{-6} m/m/K (Professional Plastics) leading to hoop stresses being generated on the inside of the ceramic by the expanding aluminum.

The solution was found in a material that had properties intermediate between those of Delrin and Mycalex. Polyamide-imide (PAI) has a melting point of 274°C, a COE of 25.2 x10^{-6} m/m/K and is easily machined. A heat-break stem machined in PAI is pictured alongside a Delrin stem in Figure 3.11, while a machined PAI stem is pictured atop a rotor in Figure 3.12 .

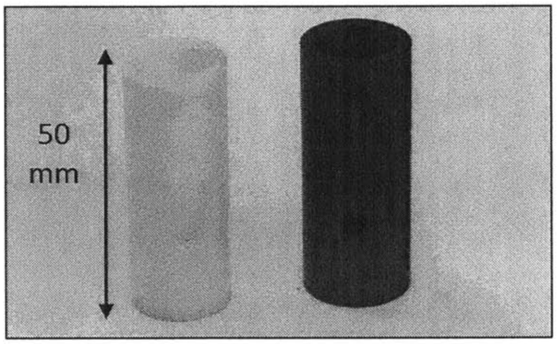

Figure 3.11: Delrin stem (left) and PAI stem (right)

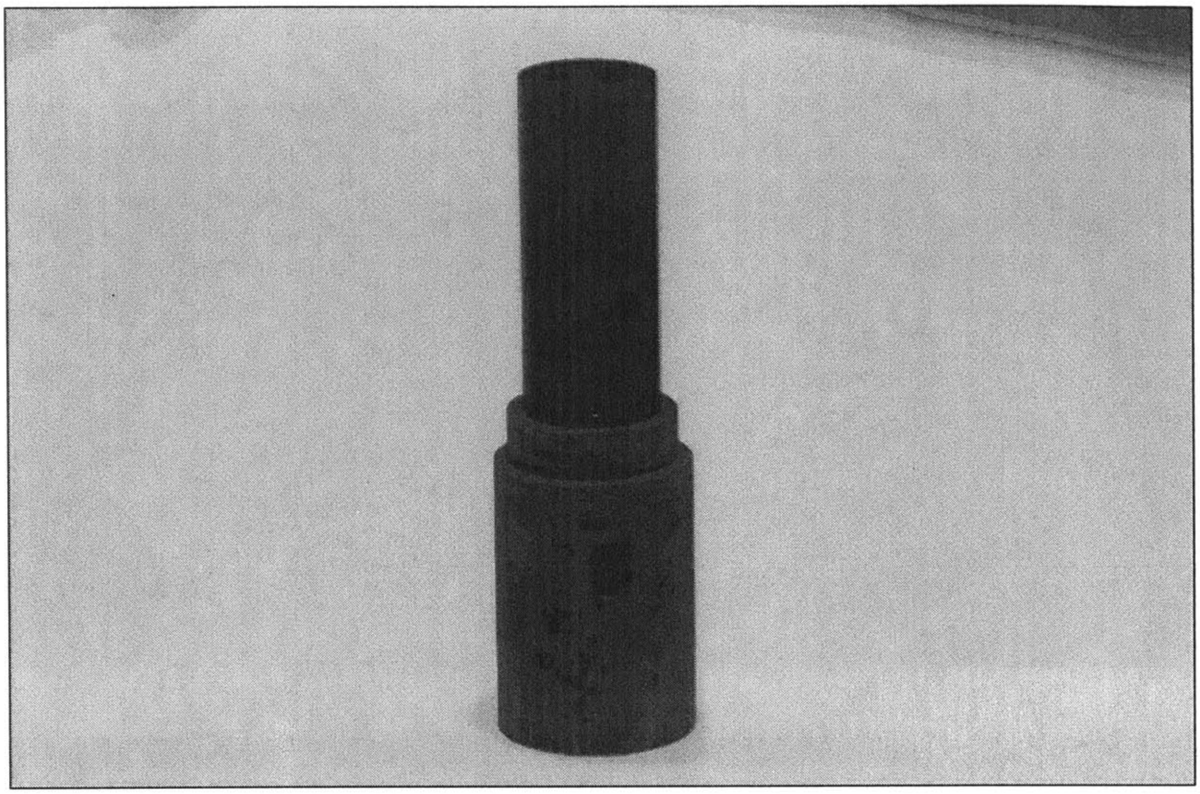

Figure 3.12: PAI stem mounted atop a superhydrophobic aluminum rotor

3.3.4 Low Temperature Leidenfrost Surface

The logical choice for the surface of the rotor was the PMMA/POSS combination used by Srinivasan *et al*. However, due to the difficulty associated with obtaining the fluoro-POSS molecule, this was not possible. The natural alternative was PMMA/PFDA (discussed in section 2.1.1) as it offered similar drag-reducing performance. However, both of these coatings are PMMA-based, which has a glass-transition temperature of T_g = 108 °C. Film boiling on any surface, even those optimized for very low Leidenfrost Temperatures, would likely take place at a higher temperature than this, so any PMMA-based option was ruled out. Initial testing was instead carried out using a nano-structured, porous hydrophobic surface. It was applied using the layer-by-layer (LBL) coating process (O'Hanley *et al.*, 2013) The substrate is first dipped into a polycation solution, imposing a negative charge upon it. It is then successively dipped into polyanion and polycation solutions of poly(allylamine hydrochloride) and silica nanoparticles until a 50-bilayer, 22nm thick coating is created. The resulting coating is then silanized and calcinated. The former step adds chemical hydrophobicity to the nanostructure, while the latter imparts upon it very high mechanical robustness. This surface exhibits tremendous resistance to mechanical wear, to the point that it could be rubbed vigorously and still maintain its hydrophobicity. It also retained these properties to a temperature of over 250°C, and featured a Leidenfrost temperature of approximately 150°C. However, it featured a critical heat flux higher than the value that the 250W heater was able to provide, so the cold rotor immersed in water could not be heated to film boiling. Instead, the rotor had to be initially heated in air to approximately 200°C, and then immersed into water, effectively removing the need to climb over the "hump" or local maximum in the film boiling curve. Another major drawback to the coating was that creating it was a highly time-intensive process, requiring no less than 4 days of work.

These major issues led us to consider an alternative, which was found to lie in realms outside of coatings. In this latest attempt, with the collaboration of Dr. Dayong

Chen, the aluminum rotor was dipped in 18% Hydrocholoric acid, which etched a microstructure into the metal. The resulting surface was then silanized in a solution of perfluorooctyltricholorosilane in hexane (7 μL per mL), leading to a robust syperhydrophobic surface (θ_{adv} = 161°, θ_{rec} = 160°) with an extremely low Leidenfrost temperature of just over 100°C. Only 9% of the heater's 250W maximum power output was required to heat this surface from the temperature of the surrounding water directly to film boiling, seemingly never passing through the nucleate boiling regime.

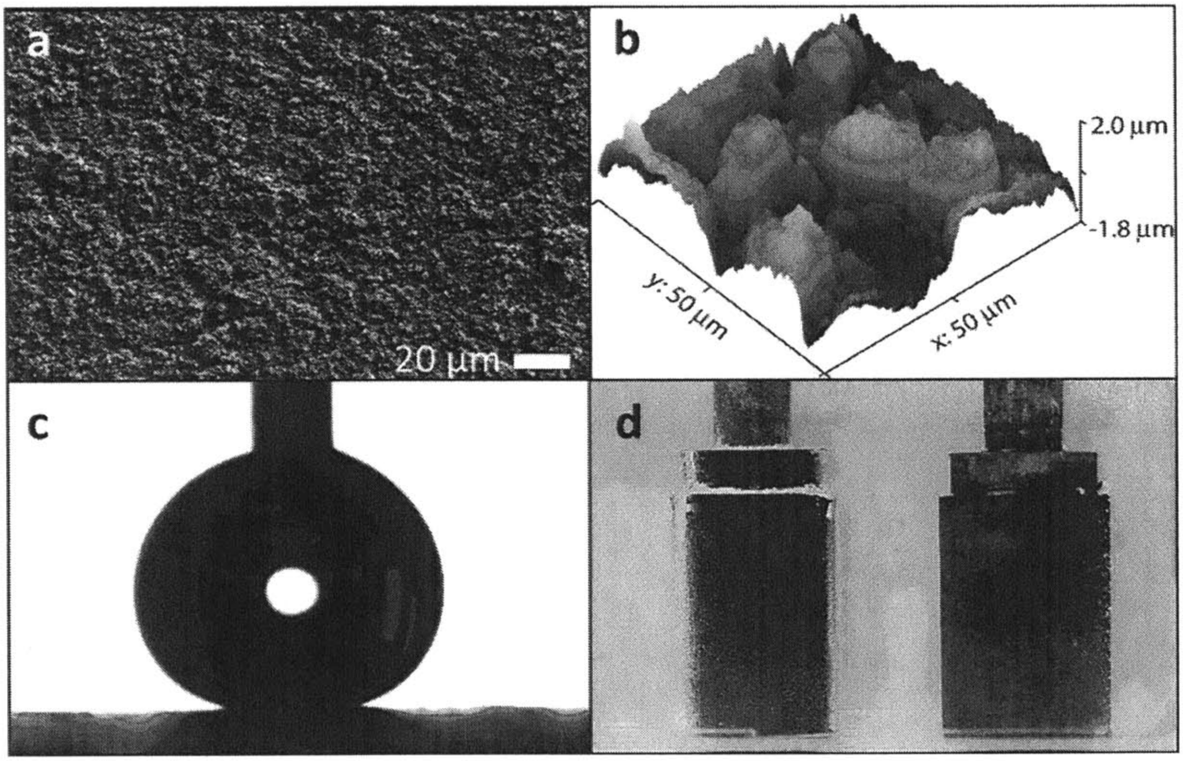

Figure 3.13: : Low-Temperature Leidenfrost superhydrophobic surface. **a**: A scanning electron micrograph of the acid-etched and silanized aluminum surface. **b**: An atomic force micrograph of the same surface. The surface roughness parameters were calculated from this profile: mean square height (m_o) of 0.58 μm, a Hurst Exponent (H) of 0.643 and a mean square slope (m_2) of 0.10. **c**: A water droplet on the surface, showing high contact angles indicating superhydrophobicity. **d**: An image of two identical superhydrophobic rotors. The rotor on the left is at 150°C, showing a thick, continuous steam film. The rotor on the right is at room temperature, and consequently has no steam film.

Unfortunately, the surface proved unable to sustain film boiling for more than a few minutes, after which it gradually transitioned back to nucleate boiling. The issue was hypothesized to be boehmitization of the aluminum in boiling water (Kim *et al.,* 2013), and was dealt with by thickening the oxide layer surrounding the aluminum by heating it. The resulting surface required 40W to achieve sustained film boiling and became the surface of choice for all future experiments.

3.3.5 Lessons Learned from First Full Prototype

The first full prototype of the film boiling system proved to be instructive in a number of ways. As before the dish holding the gallium eutectic was 3-D printed in ABS. As discussed in section 3.3.1, the tendency of the gallium to oxidize in air was mitigated by opening a sealed shipment of the eutectic in an inert glove box, and then covering the gallium with rapeseed oil prior to exposing it to air. The holder containing the eutectic sat atop the Taylor Couette cell, and the PAI/Aluminum rotor was attached to the rheometer. After the leads from the heater were dipped into the eutectic, the rotor was gradually spun up to higher and higher speeds – it was ascertained that a safe maximum rotation speed for the system was 60 rad/s. The rotor was immersed in water, and 120V and 250W was send to the heater. This early setup can be seen in Figure 3.14.

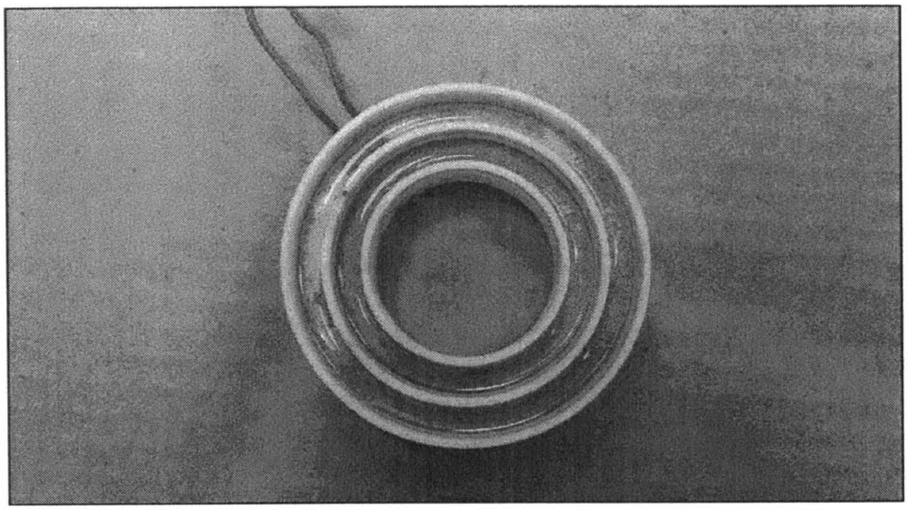

Figure 3.14: Top view of the liquid metal holder (ABS).

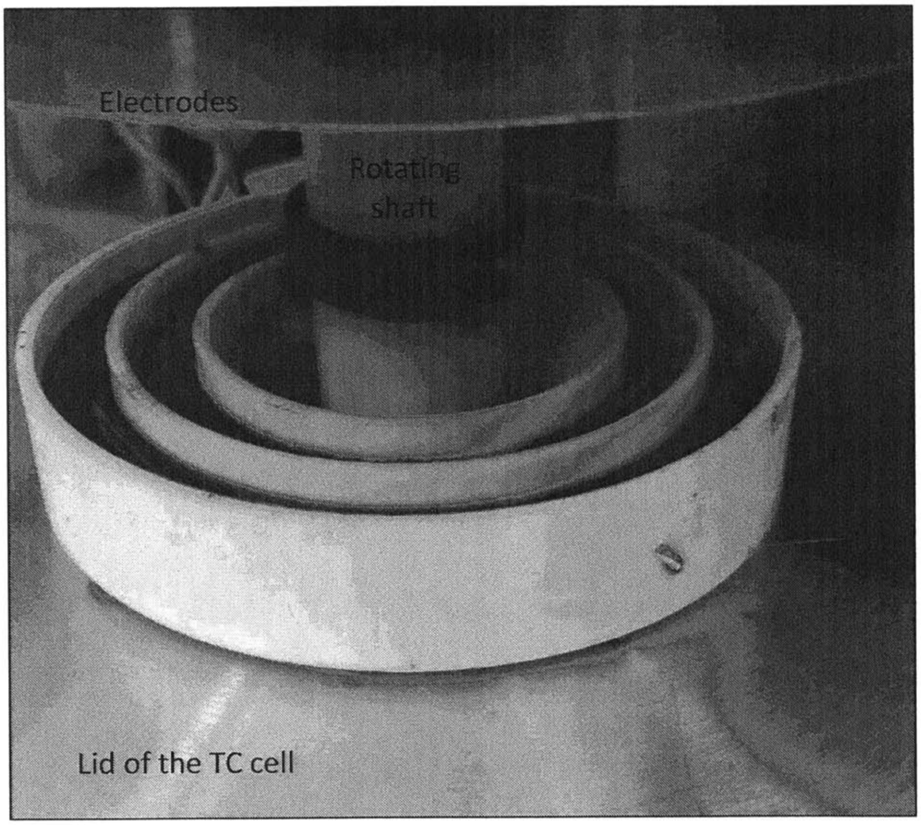

Figure 3.15: The gallium holder containing the liquid metal atop the Taylor-Couette cell, with the rotor attached to the rheometer.

A boiling film was established when the rotor was immersed in water, but the experiment was cut short due to several observations:

1) Under rotation, the rotor was found to "wobble" – a visual indicator of non-concentric rotation. Since the path that the rotor was tracing was not circular, this effectively prevented it from being a true Taylor-Couette system.
2) After several minutes, the PAI began to melt. Since the melting point of PAI was 274° this seemed like an unlikely outcome but it clearly illustrated the need for additional characterization of the coating and an estimation of the how much power would be required to sustain a film.
3) Due to an error in the procedure, the rotor began to spin at 100 rad/s, well above the 60 rad/s that it was deemed safe for. The wire was being pulled through the gallium at too high a speed, leading to the liquid metal leaking out of the holder, and onto the Taylor Couette cell, as well as some of it being hurled out of the system. While very little was flung out, the leakage into the Taylor Couette cell was not noted until several minutes later, by which time it had begun to corrode the aluminum body of the cell. The affected region of aluminum changed to a much lighter color, and soon as it came into contact with water, it began to react, producing hydrogen gas as well as dark gray aluminum hydroxide. The damaged sections of the cell are shown in Figure 3.16.

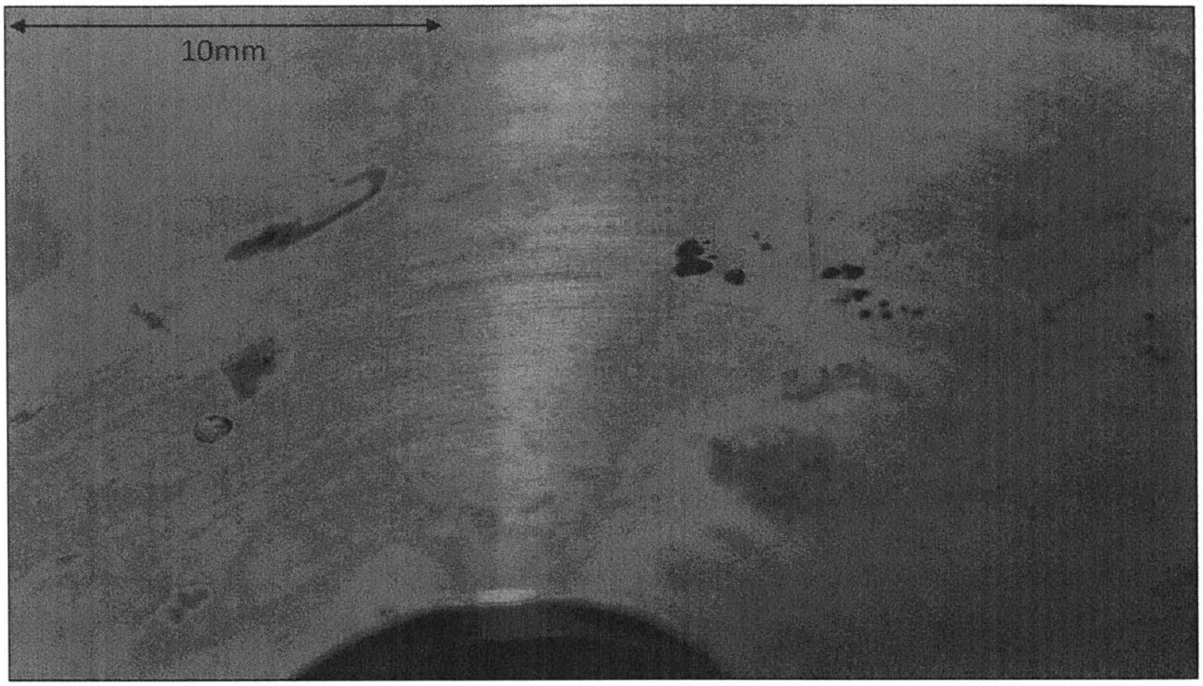

Figure 3.16: Damage to the lid of aluminum Taylor-Couette cell due to exposure to gallium. The damaged areas are dark gray in color due to a reaction between the bare aluminum and water, which led to the formation of dark gray aluminum hydroxide.

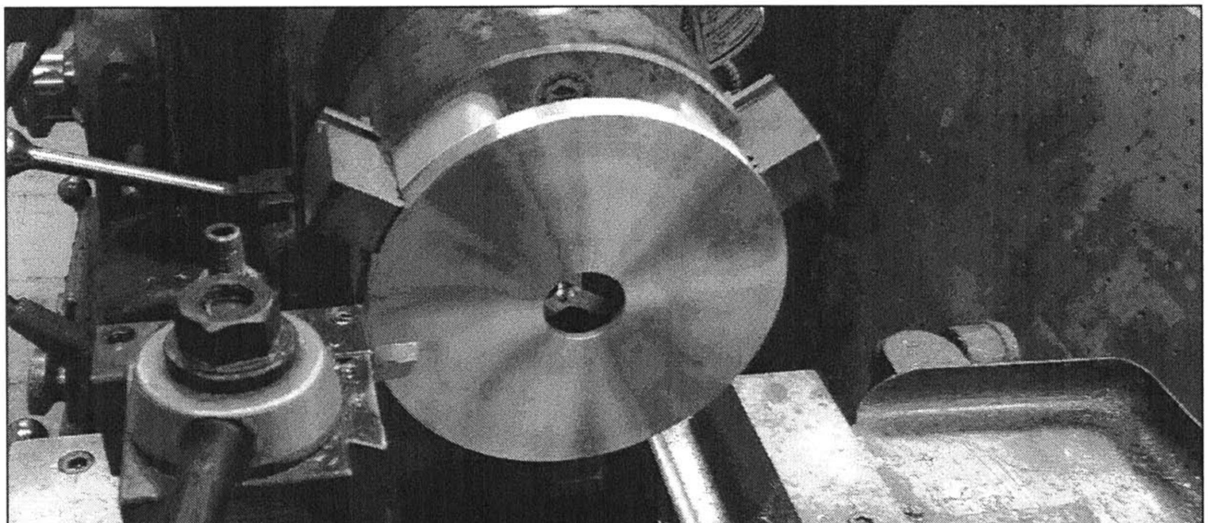

Figure 3.17: The setup used to remove the gallium damage from the top of the Taylor-Couette cell. The resulting clean aluminum surface is pictured.

Since there is no way to chemically remove gallium once it has permeated into aluminum, the damaged area was machined off, as shown in Figure 3.17. The gallium-impregnated section of the aluminum, while no different to the rest of the specimen to the touch, displayed a completely different behavior under machining as it had become much softer and less brittle. The Taylor Couette cell was fully restored to its previous condition.

Each of these observations required certain changes to be made to the system. The first of these, the issue of non-concentric rotation, was traced to the method in which the stem was being machined. This consisted of three main steps – the turning of the diameter of the stem, and the boring of two holes on either end. During this process, the PAI stock was moved in and out of the lathe a number of times. When working with stock with a large length-to-diameter ratio, the lathe effectively acts as the fixed end of a cantilevered beam, while the tool exerts a force on the beam.

The force exerted by the tool causes the beam to deflect, and this results in chatter, causing an uneven and imprecise finish. The simplest way to mitigate this is to expose as little of the stock as possible while machining, effectively decreasing the length of the cantilever and hence minimizing the deflection and chatter. However, this does result in the stock being released from the collet several times, and each time it is re-clamped, its position changes slightly. Any further machining operations are thus no longer about the same rotational axis as before, leading to the two bores being non-parallel. This leads to non-concentric rotation, as pictured in Figure 3.18.

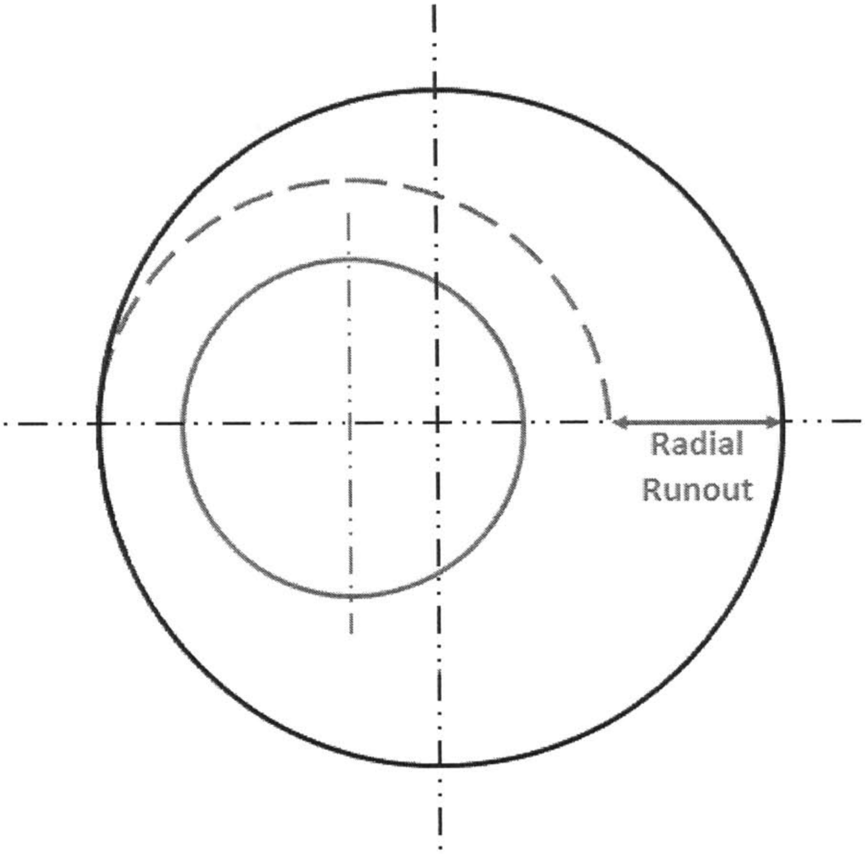

Figure 3.18: Explanation of radial runout. The black circle indicates the stock, while the red circle indicates a hole that has been bored off-center relative to the stock.

Completely avoiding chatter while achieving a high degree of concentricity appear mutually exclusive, but both goals can be achieved reasonably well by using a 3:1 length : diameter ratio. This is generally considered to be the largest allowable ratio before chatter becomes significant, and it also allowed just enough of the stock to emerge from the lathe that the entire diameter could be turned, and one of the end holes could be bored. A setup-change with the stock being removed from the collet was inevitable at this point in order to bore the second hole on the other side. However, in order to ensure a high degree of concentricity between the two holes, a dial indicator was used to characterize the rotation of the diameter. As shown in Figure 3.19 the lathe used featured a "buck chuck" – a chuck which allows its concentricity to be changed, and this was modified until it matched the previously turned diameter to within 0.0005". The second hole was then bored, resulting in a high degree of parallelism, and minimal runout. Visually, the wobble was completely eradicated.

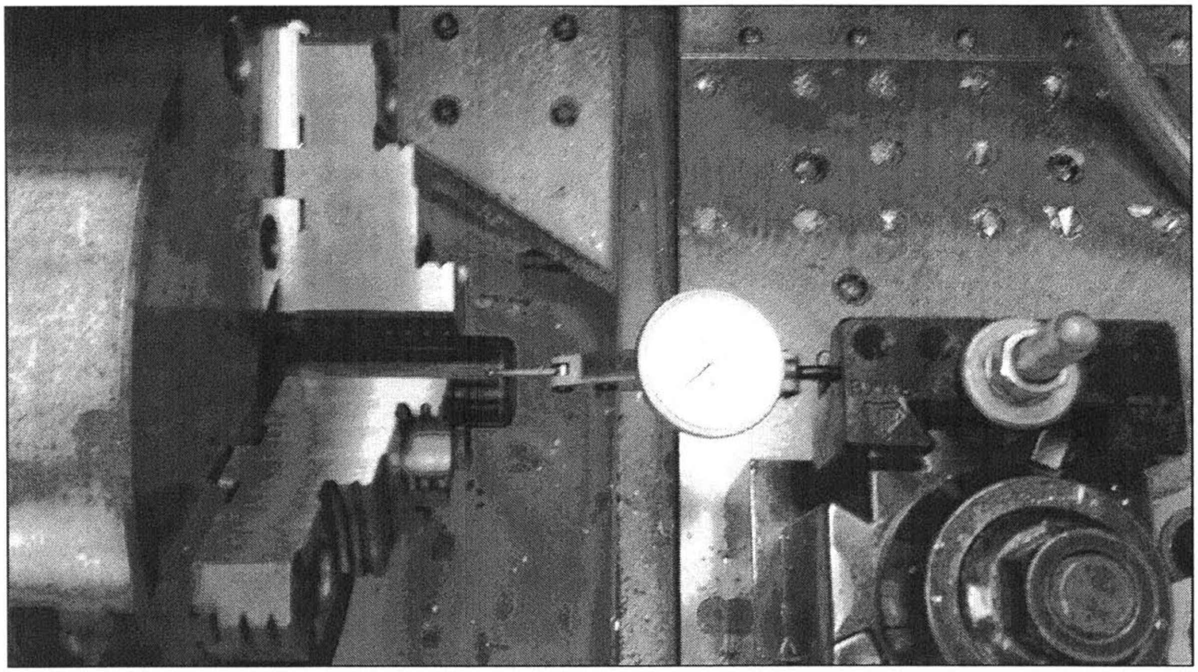

Figure 3.19: Setup used to minimize wobble when removing and replacing parts in the lathe jaws. Dial indicator (pictured) and buck chuck were used to achieve a high degree of concentricity.

The second issue in the system that was exposed by the prototype was the lack of temperature control. Firstly, it was apparent that 250W was more than enough to allow the rotor to attain critical flux and begin to film boil. Once the rotor began film boiling, the substantially lower heat transfer rate caused the rotor to heat up rapidly. One way to mitigate this was to heat the rotor in air to a temperature above the Leidenfrost point, and then lower it into the water with a lower power input from the heater. However, in order to prevent any accidental overheating, temperature measurement was still required. The same challenges with sending power into the spinning rotor without adding torque to the system also applied here. Embedding the thermocouple into the rotor and extracting the signal via the gallium eutectic was a possibility, but involved a great deal of additional complexity. Instead, an IR thermometer (Extech 42545) was calibrated to the emissivity of the rotor and was used to monitor its temperature throughout the experiment. While this did not allow for a control loop to ensure a tight temperature band, it was sufficient to alert the operators of any anomalies causing the temperature to increase beyond safe limits, and would allow for safe shutdown of the test before the Torlon plastic stem could get close to its melting point.

The third issue, concerning the leakage of the eutectic, was the most important of the three. While the damage to the Taylor Couette cell was not catastrophic, the possibility of eutectic getting spread around the testing environment posed a clear safety risk. The design approach taken sought to mitigate a potential gallium spill in two different ways:

(i) Prevention. The initial design of the holder did little to prevent a spill taking place in the event of an unexpected increase in rotation rate. It was thus redesigned to make the openings in the holder at the same level as the surrounding material, and the walls of the holder were also modified so as to be concave. This approach would not have been possible had the holder been fabricated by virtually any method other 3D printing (Figure 3.20).

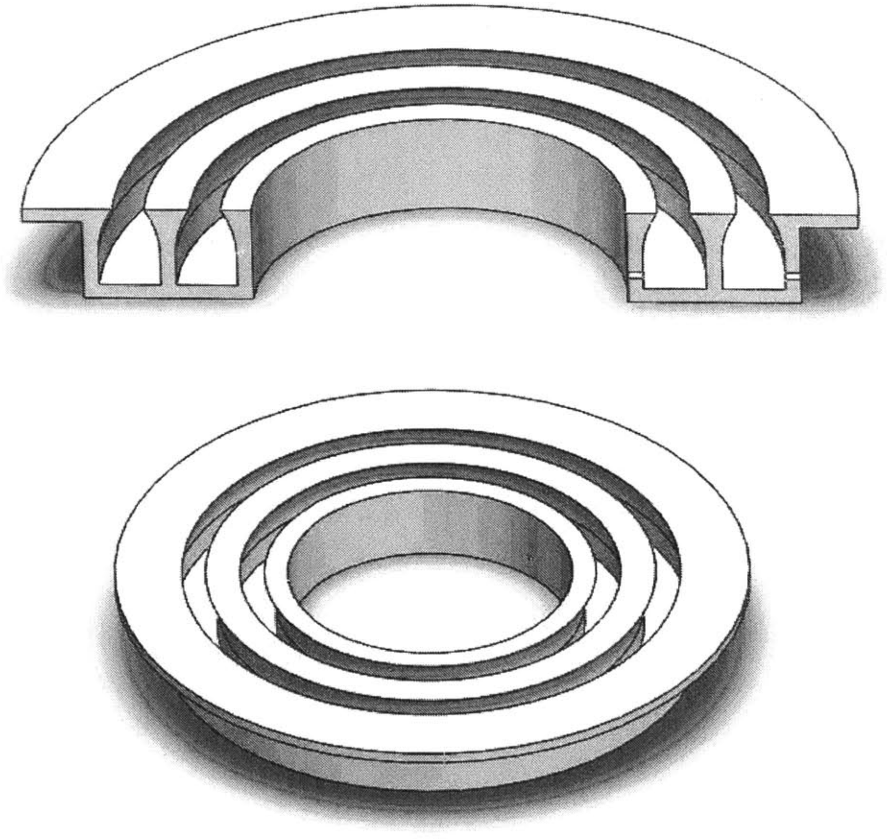

Figure 3.20: CAD models of the 3-d printed holder with concave side walls and narrower openings at the top to minimize the risk of a gallium spill.

(ii) Containment. In the event that a spill should take place in spite of the countermeasures detailed above, it was extremely important that the gallium be contained and prevented from reaching the rheometer or any other parts of the laboratory. This was achieved by enclosing the gallium eutectic holder and the rotor in an acrylic enclosure (Figure 3.21).

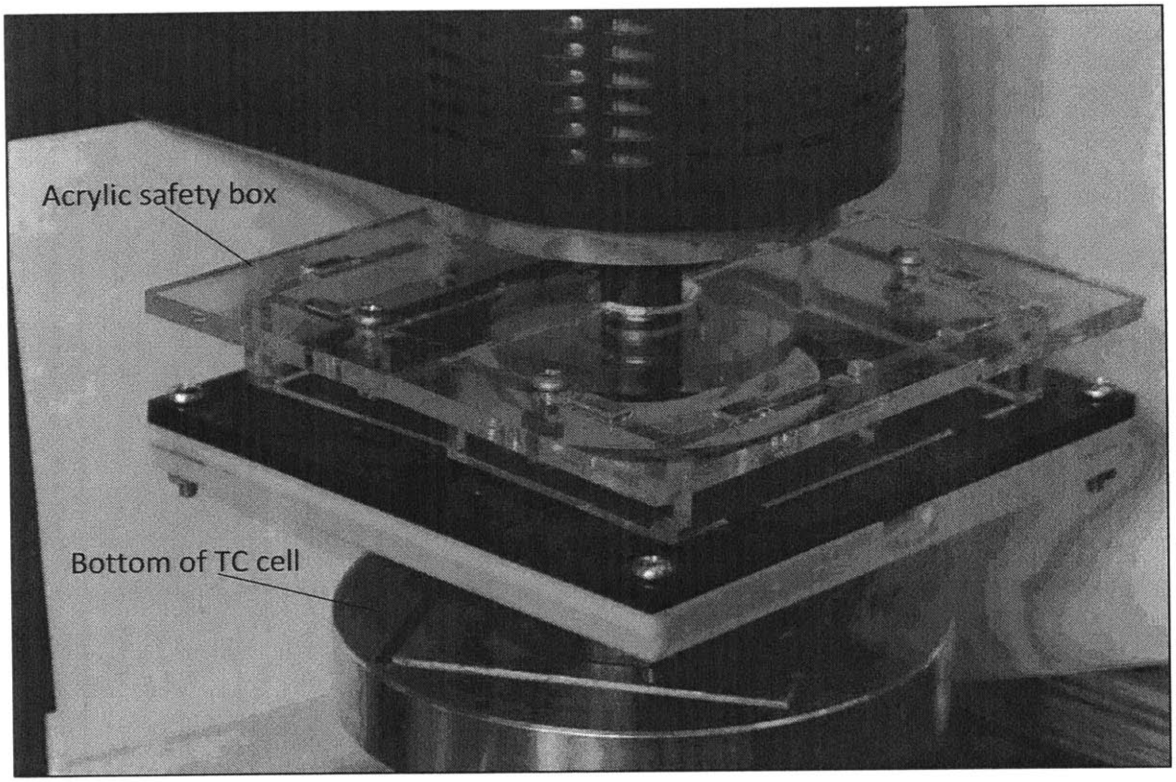

Figure 3.21: Image of the safety box (clear acrylic) and the additional layers of safety (black and white acrylic) added to the system.

The enclosure fits over the system in two symmetric parts. The spinner, the piece that holds the wires from the heater in place, was also redesigned in order to also act a steam shield, preventing water from entering the rheometer (Figure 3.22).

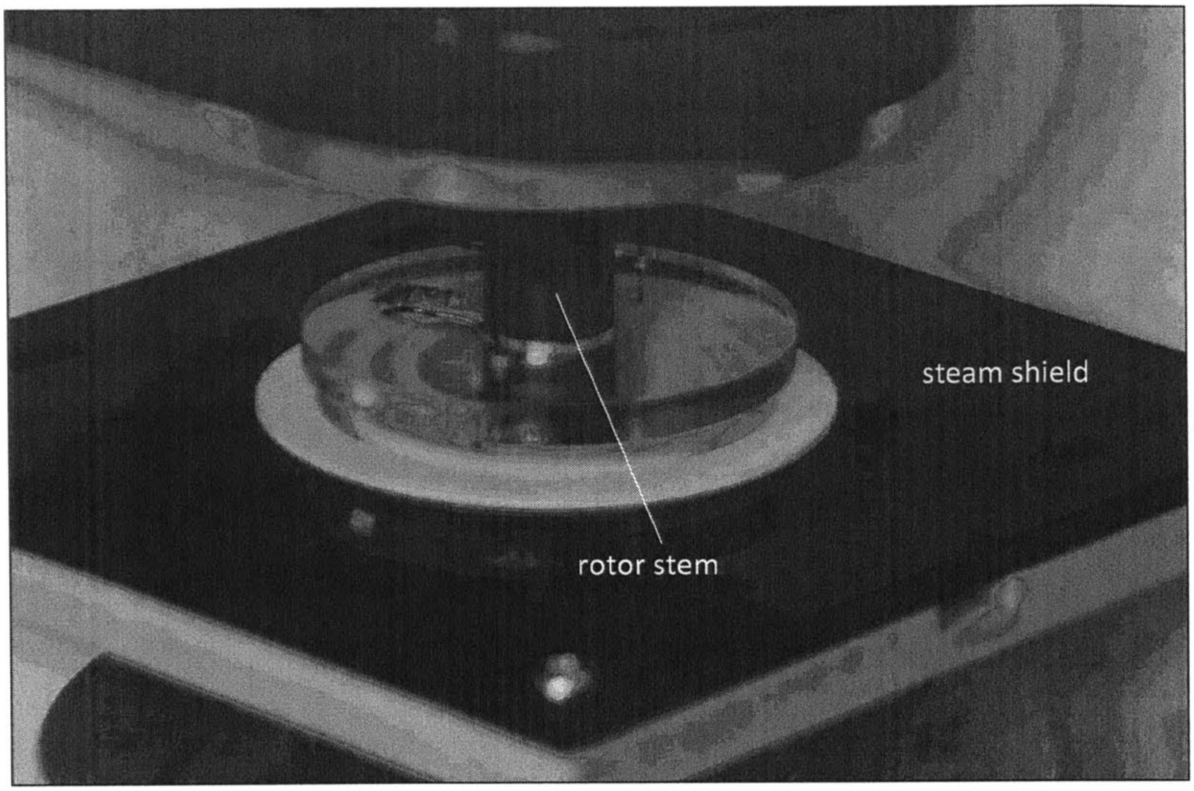

Figure 3.22: Image of the steam shield/wire holder (transparent acrylic), attached to the stem of the rotor (dark grey plastic).

The combination of the steam shield and the gallium effectively prevent any gallium or steam from leaving the closed system, protecting both the rheometer and the surrounding lab area from any hazards.

3.3.5 First Drag Reduction Result

Based on the various criteria discussed in the previous sections, the first system to successfully achieve a drag reduction was created.

Initially, two rotors were prepared: one "smooth", untreated aluminum rotor and one that was etched and silanized to give an SH surface. Table 3-2 describes the tests that were run.

Test	Surface	Gallium Torque	Heating	Notes
Active	Acid etched, silanized Al	Yes	Yes	
Passive	Acid etched, silanized Al	Yes	No	
Gallium Calibration	Acid etched, silanized Al	No	No	(Passive) – (Gallium Calibration) = Gallium torque

Table 3-2: The three tests carried out in order to find the drag reduction due to film boiling. The gallium calibration test was required to ascertain the gallium torque in each case so that it could later be subtracted out from the active and passive torques.

The graph of results in Figure 3.23 reflects the torques after the gallium torque had been subtracted.

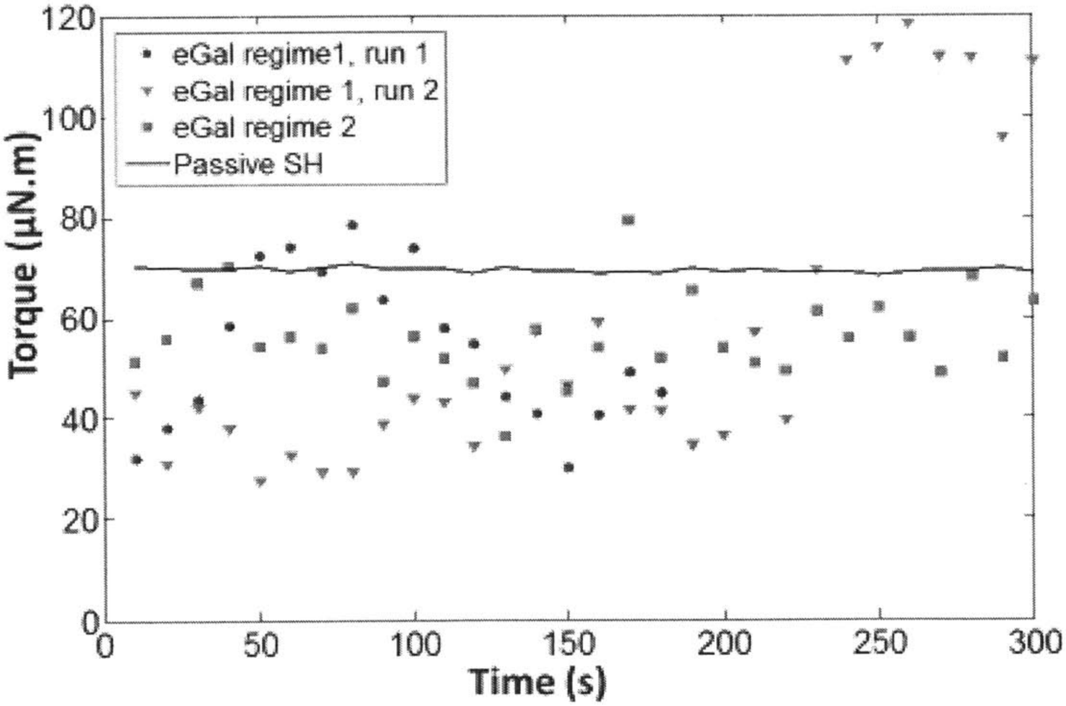

Figure 3.23: Traces of torque vs time for a film boiling rotor. Also plotted (in black) is the baseline torque of a passive, non-film boiling rotor. The gallium torque has been calibrated out.

Possibly the most interesting feature of these result occurred in the eGal (gallium eutectic) regime 1, run 2 (red) dataset, which features a sudden increase in torque after 230 seconds of operation. This occurred due to oxidation of the gallium, causing the torque exerted by the eutectic on the wire to be magnified. This step change was then calibrated out in the third experiment (green). The mean torques of the passive SH surface vs the active SH surface are shown in Figure 3.24.

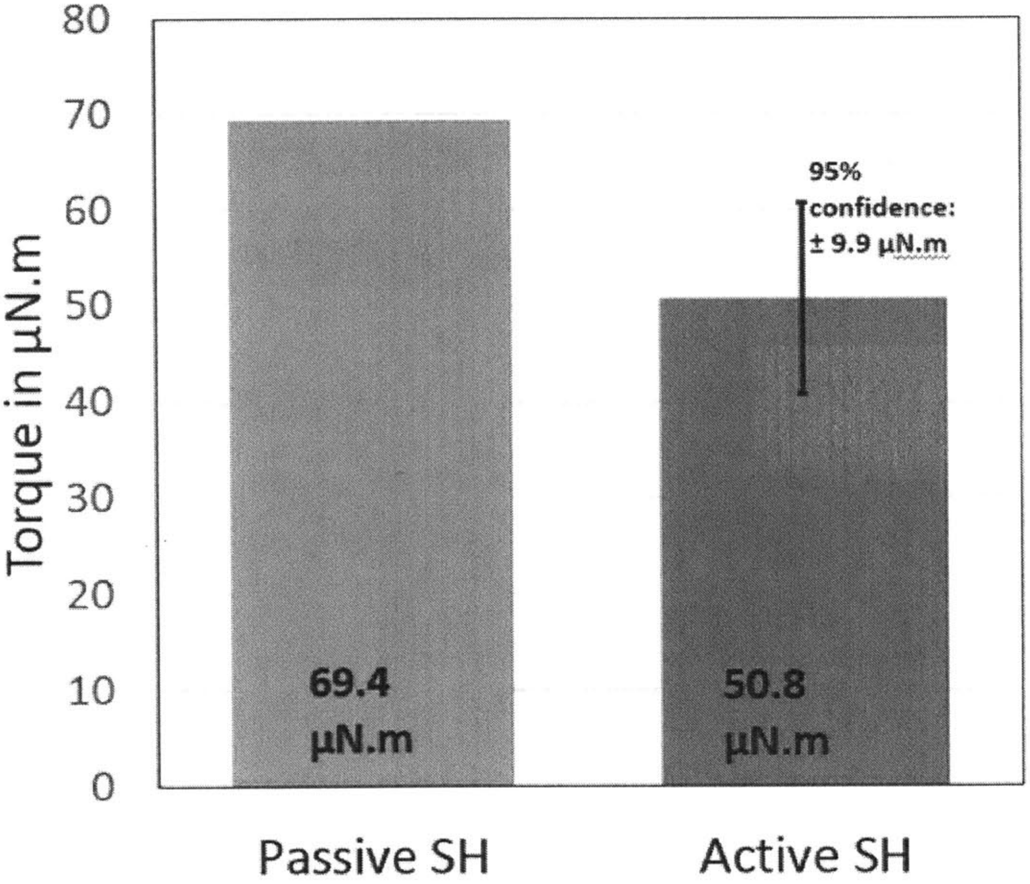

Figure 3.24: Average torques of passive and active rotors compared, indicating a 27% drag reduction as a result of film boiling on the SH surface.

These experiments were all carried out at 60 rad/s (Re = 52,200), with a water temperature of 84°C. At this temperature, the viscosity of water is approximately 3.350 x 10^{-4} Pa.s.

While the measured average of 27% drag reduction was certainly encouraging, certain issues arose during the course of the experiment. The most important of these, of course, was the afore-mentioned increase in gallium eutectic torque due to oxidation. Several options were considered to prevent this oxidation, including creating an inert environment around the Taylor-Couette cell by pumping Nitrogen or Argon through the safety box. However, the rotating stem would be likely to entrain air and hence oxygen, defeating the goal of an inert environment. Consulting literature proved that this issue was a common one, and that one possible solution was to add hydrochloric acid to the gallium eutectic (Figure 3.25).

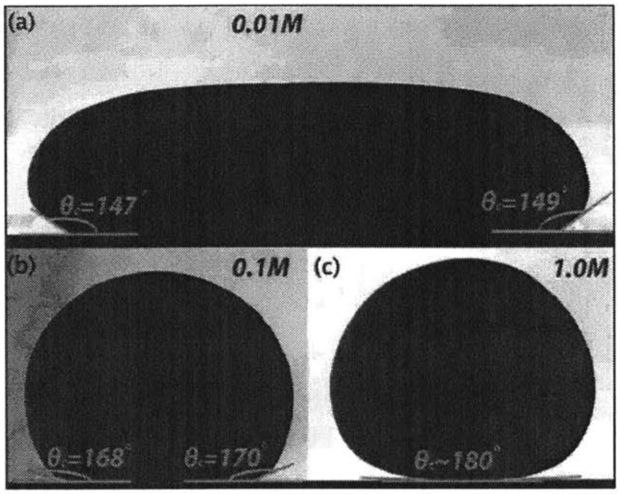

Figure 3.25: Gallium contact angles in various concentrations of hydrochloric acid (Xu *et al.* 1994.)

While heavily oxidized gallium was beyond repair, acid was able to remove some of the oxide and prevent further prevention. Adding the acid to the gallium at the end of each run and then removing it prior to the start of the next allowed for the removal of some of the oxide. However, the since the gallium holder was made of 3D printed ABS, it exhibits some porosity. The gallium eutectic has a high surface tension so it did not pass through the pores. The acid, however, certainly did and this called for a redesign of the holder. Since 3D printing is virtually the only way to obtain the overhanging walls, and these were deemed unnecessary in any case, the new holder was milled in polycarbonate. With the elimination of the curved walls, the spinner was adapted to become a continuous disk with two ridges protruding downwards towards the holder. The holder, meanwhile, had two additional channels, one inside and one outside the gallium eutectic channels, into which the ridges from the spinners dropped. The result was that any gallium splashes would impact the spinner, and either fall back into the gallium channels, or would move outwards by centrifugal action, and be deposited into the outer channel (Figure 3.26).

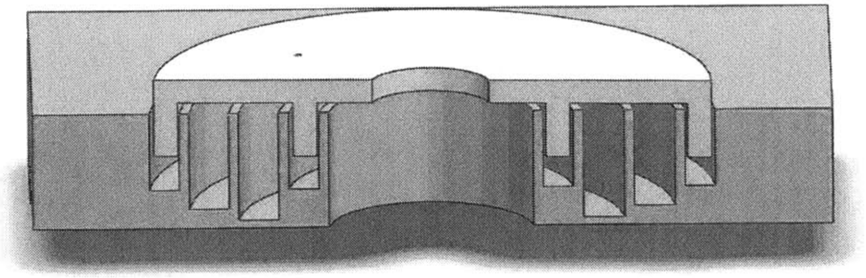

Figure 3.26: CAD rendering of the new spinner and holder system, to prevent gallium splashing.

The piece was machined from a single polycarbonate plate using a mill. The machining process is shown in Figure 3.27, and the final part is shown in Figure 3.28.

Figure 3.27: Milling of the polycarbonate liquid metal holder.

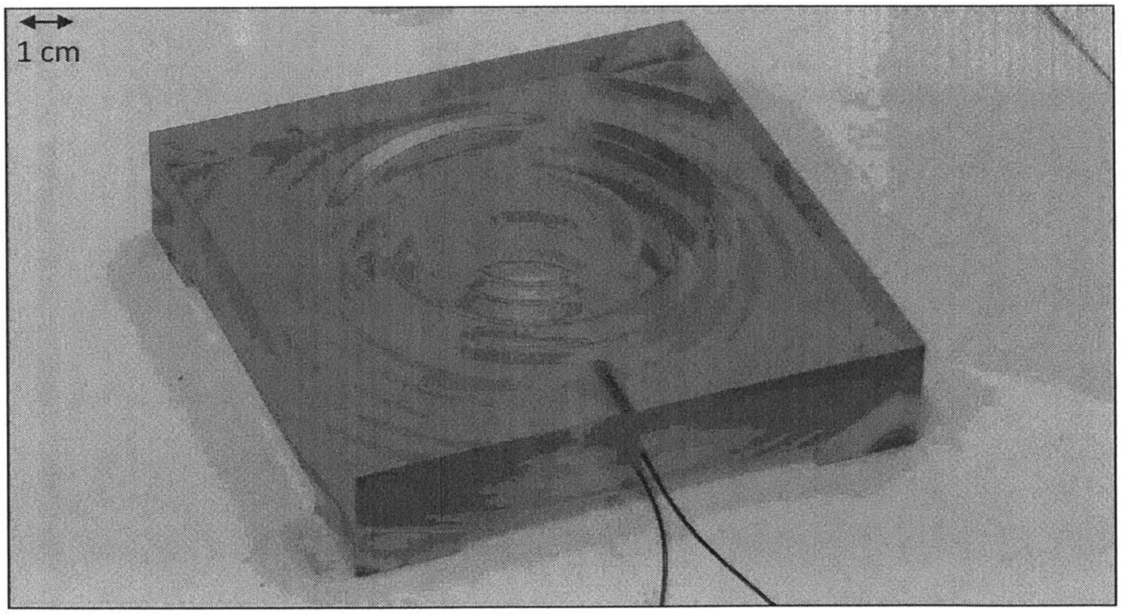

Figure 3.28: Image of the completed polycarbonate liquid metal holder

Chapter 4 : Active Drag Reduction: Results and Discussion

4.1 Final Drag Reduction Results

The modified setup described in Chapter 3 was used for all future experiments. The system is pictured in Figure 4.1 and Figure 4.2 below:

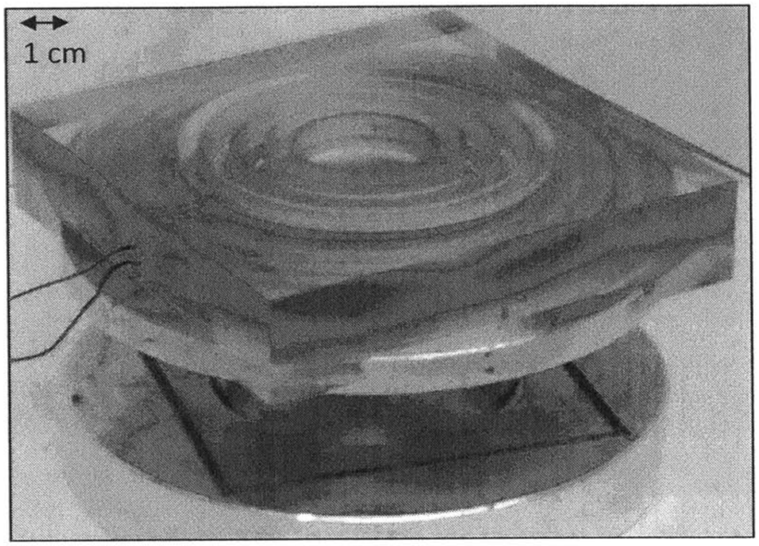

Figure 4.1: The liquid metal holder mounted atop the Taylor-Couette cell

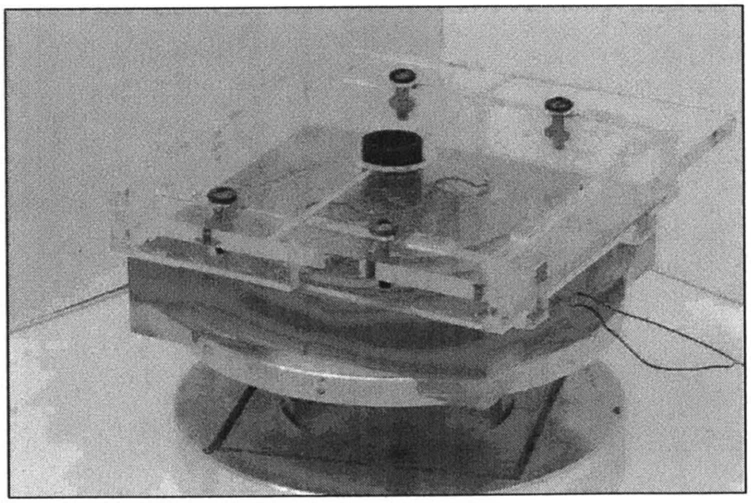

Figure 4.2: The liquid metal holder atop the TC cell, with the rotor inside and the protective safety box.

A change was made to the experimental procedure. To avoid the possibility of the oxidation state of the gallium changing between runs, a single experiment was carried out to measure drag reduction. The rotor was heated to 160°C as before, and lowered into the water. A steam film immediately formed, the power was routed to the heater via the gallium, and the experiment was begun. After 5 minutes of rotating at 60 rad/s (*Re* = 52,200), the power from the variac was gradually shut off over the course of one minute. The film slowly disappeared, leaving a passive superhydrophobic surface. Over the last 10 minutes of the test, the rheometer would measure the varying torque. Figure 4.3 below shows a typical experimental result.

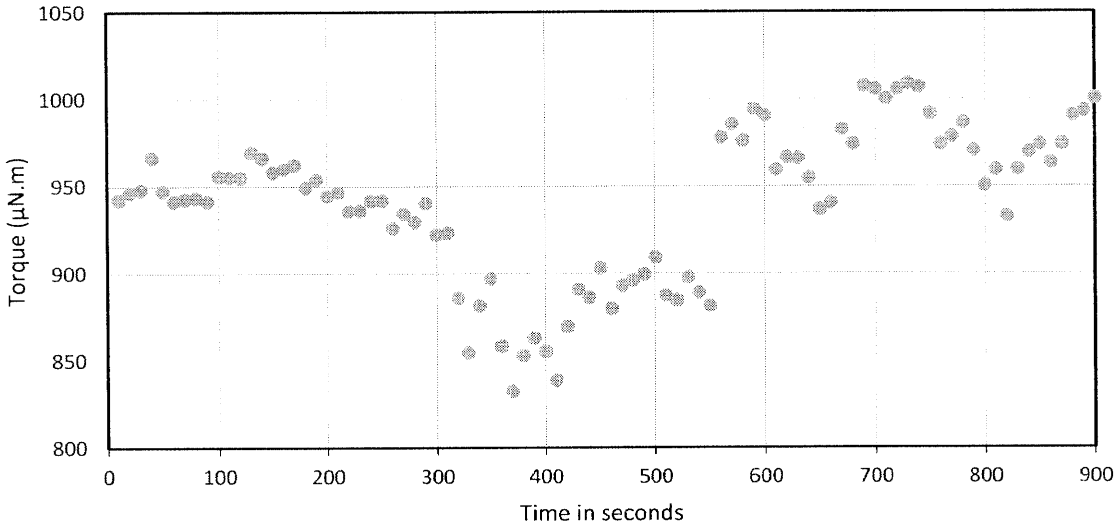

Figure 4.3: Sample trace of torque vs time for an experiment carried out at Re = 52,200. The power to the heater was turned off at t = 300 s, leading to the measurement of a lower torque. This indicated that greater drag reduction that that measured in Chapter 3 is possible.

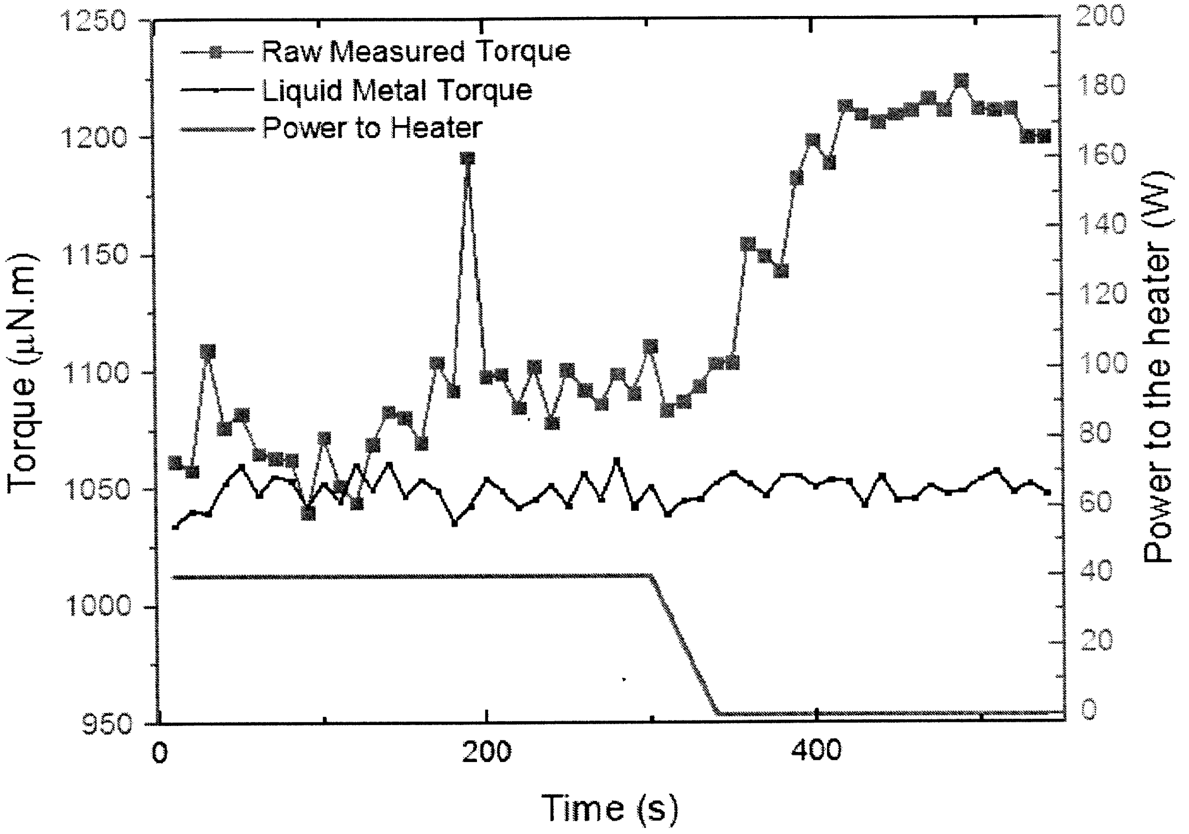

Figure 4.4: Measured torque (green) for a single experiment showing drag reduction over time. Power was supplied to the embedded rotor for the first 300 s and then turned off, as shown in the orange curve. These values represent the raw torque measured by the rheometer prior to subtracting out the liquid metal torque, which is shown in black. For the entirety of the test, the angular velocity of the rotor was 60 rad/s, corresponding to Re = 52,200. A drag reduction of 90.4% was measured.

Comparing the torques from 0-300 s (heated, film boiling rotor) to 600-900 s (passive SH surface) indicates a drag reduction of 28%, consistent with the result discussed in Chapter 3. Between 0 and 300 seconds, the power to the heater was about 60W. However, the behavior between 300 and 600 s is of great interest. The lowered torque can be explained through observations recorded during the experiment. During the first 300 s of the test, the boiling film appeared to feature a great deal of axial motion. The reduction in power over the following 300 s results in a boiling film with less axial convection. One possibility is that axial convection in the film leads to increased form drag, and hence increases the measured torque. The maximum recorded drag reduction, between 300-600 and 600-900 s was approximately 90%, and so only 35-40 W was provided to the rotor in future experiments. A typical result is shown in Fig. 4.2, above.

4.2 Discussion

Two-Fluid Taylor-Couette Model

This large skin friction drag reduction can be explained using boundary layer and slip theory. We model the system as a rotating inner cylinder of radius R_i surrounded by a layer of steam of uniform thickness h in a water-filled stationary cylinder of radius R_o (Fig. 4.5 **a**). We make use of the skin-friction law derived by Srinivasan et al., which posits that the velocity in the viscous sublayer of the turbulent flow is shifted by a constant value, b^+:

$$\frac{V_i}{u_\tau} = M \ \ln \ \mathrm{Re}_\tau + N + b^+ \tag{4.1}$$

Equation (4.1) holds for near-wall flows, where V_i represents the velocity of the inner rotor, $u_\tau = (\tau_w/\rho)^{1/2}$ is the friction velocity and $Re_\tau = u_\tau \Delta r/\nu$ is the friction Reynolds number. The first two terms on the right hand side of the equation pertain to a smooth, passive rotor in water. M and N are geometry-dependent constants, and are obtained by fitting equation 4.1 to data for a smooth, non-superhydrophobic, non-heated rotor. For this system, it was found that M=3.8 and N=-12.5. The presence of a slip boundary condition is responsible for the final term, b^+, which is the slip length b divided by the viscous length scale $\delta_v = Re(C_f/2)/\Delta r$. For the Taylor-Couette cell described above, this value is defined as:

$$b^+ = \frac{b}{\delta_v} = \left(\frac{b}{R_o - R_i}\right) \mathrm{Re}\sqrt{\frac{C_f}{2}} \tag{4.2}$$

$C_f = \tau_w/(1/2\rho V_i^2)$ is the coefficient of skin friction and the slip length, b, represents the distance that the velocity profile close to the wall must be extrapolated to give zero-velocity (*i.e.* a non-slip condition). This is illustrated in Fig. 4.5 **b**, which is shown in the frame of reference of the rotor such that the rotor appears stationary, while the outer wall appears to be rotating.

The Navier slip length b can be found from:

$$b = \frac{V_{slip}\mu}{\tau|_{r=r_i}} \tag{4.3}$$

Solving for V_{slip} requires the velocity profile. Since the system is axially symmetric, one can solve for the velocity profile using the Navier-Stokes equation in cylindrical co-ordinates for an incompressible fluid. We assume that the flow is laminar in the viscous sublayer near the wall and adopt a laminar model to compute the slip length. We also assume that the flow is diven only by the motion of the rotor, and not by any pressure gradients or gravity. The full derviation can be found in Appendix C.

Evaluating and dropping higher order terms, this ultimately simplifies to equation (4.4).

$$b_{slip} = h\left[\frac{\mu_w}{\mu_s} - 1\right]\left(\frac{R_o^2}{R_o^2 - R_i^2}\right) \tag{4.4}$$

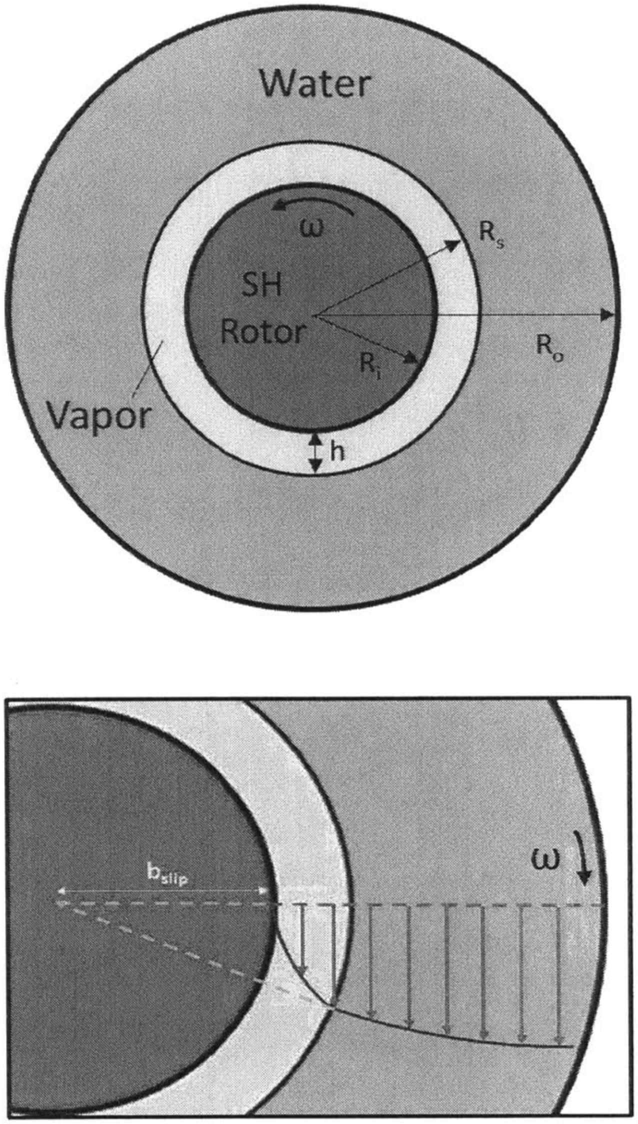

Figure 4.5: (top): Schematic of the system, consisting of a rotating inner rotor surrounded by a film of steam in a stationary outer cylinder filled with water. Bottom: velocity profiles in both liquids.

We find that the slip length scales with the thickness of the vapor film h, and with the ratio of viscosity of the two fluids μ_w/μ_s. This result is similar to that predicted by previous literature (McHale et al., 2010 and Feuillebois et al., 2009). Achieving a high viscosity ratio is essential in achieving high drag reduction. In these experiments, the water was heated to 86 °C in order to reduce the rate of heat loss from the rotor and hence reduce the energy input required to sustain film boiling. However, heating the water reduces its viscosity, and using water at room temperature would appriximately triple the slip length. The third term $R_o^2/(R_o^2-R_i^2)$ is a non-dimensional value that captures the geometry of the Taylor-Couette cell. As discussed by Feuillebois and McHale *et al.*, a geometric length scale component is inevitable in such systems due to the curvature of the surfaces. In the case of the bespoke setup used here, $R_o >> R_i$ and the large gap renders the geometric contribution a relatively small component of the slip length.

Equation (4.1), in Prandtl-Von Kármán co-ordinates (Srinivasan *et al.*, 2015) is presented below:

$$\sqrt{\frac{2}{C_f}} = M \ln\left(Re\sqrt{\frac{C_f}{2}} \right) + N + h\left(\frac{\mu_w}{\mu_a} - 1 \right)\left(\frac{R_o^2}{(\mathrm{R}_o - R_i)^2 (R_o + R_i)} \right) Re\sqrt{\frac{C_f}{2}} \qquad (4.5)$$

Here, *Re*$_\tau$ (the frictional Reynolds number) and u_τ (the friction velocity) have been replaced by the Reynolds number Re and C_f, the skin friction coefficient. Setting h = 0 correctly collapses the equation back to the case for a passive, wetting rotor. The same holds true if we assume that the two fluids have the same viscosity.

Data was obtained for several values of *Re* and the results are plotted in Fig. 4.4, along with a fit for the slip length obtained using equation (4.5). The vertical blue line indicates the critical Reynolds number $Re_c = 1.2 \times 10^4$ beyond which the flow can be considered turbulent. The theory matches the experimental data well. While the formuation is similar to that used by Srinivasan et al., the fact that the vapor film is continuous and thicker than the plastron trapped by a typical superhydrophobic surface means that the viscous sublayer begins to approximate the thickness of the vapor film at much lower Reynolds numbers. This leads to a rapid increase and saturation of skin friction drag reduction at approximately 90%.

The fitted model (black line in Figure 4.6) obtained using equation (4.5) corresponds to a slip length of 1.04 mm. As the inner and outer cylinder radii (r_i = 14 mm, r_o = 34.3 mm) as well as the viscosity ratio (μ_w/μ_a) are known for this system, equation (4.4) can be used to calculate the thickness of the steam film $h = 37 \pm 9.5$ µm. This compares favorably to experimentally measured values (Biance et al., 2003). In practice, the thickness of the boiling film is not constant but varies along the axial length of the rotor in the manner of a natural convection boundary layer. Furthermore, since we operate above the critical Taylor number ($Ta_c = 10^{10}$ for this system), toroidal vorticies are generated in the system which can also distort the film and make its thickness over time.

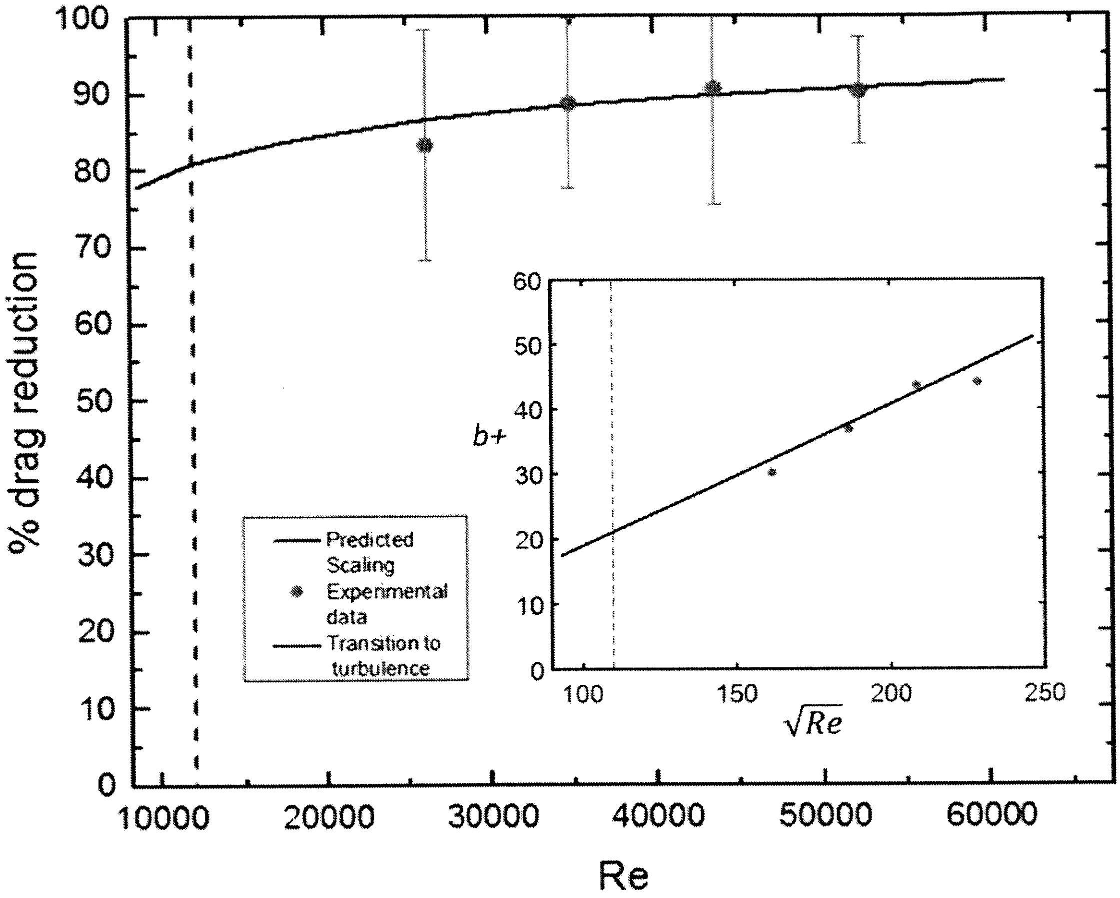

Figure 4.6: Percentage skin friction reduction as a function of Reynolds number. The black line indicates the scaling predicted by equation (8) for a slip length of 3.35 mm. The Red circles represent experimentally obtained data. The transition to turbulence is indicated by the blue line (Re = 12,000).

Since power must be actively provided in order to sustain the boiling film and reduce drag, a system efficiency can be computed that describes how much energy is saved in skin friction reduction as a fraction of the energy inputted to sustain the boiling film. As the drag on a body increases with Re for turbulent flows, the absolute energy savings and hence the efficiency also scale with Re. This is beneficial for many of the intended applications of this technology, such as boats.

4.3 Future Work

While this manuscript has demonstrated high values of drag reduction in turbulent flows, there is certainly room for further development. The torques measured for the film boiling rotors are very small, due to the large friction reduction, on the order of T = 10 μN.m or less. Since there are inherently fluctuations in the boiling film, as well as noise in the drag exerted on the contact wires by the liquid metal, the measured error of the torque is often of the same magnitude as the measured torque itself. This is still generally an order of magnitude smaller than the torque reduction, which makes plotting Figure 4.3 possible. However, an attempt to plot the data in Prandtl-Von Kármán co-ordinates would result in error bars the same size as the measured values. Since error is reported as the 95% confidence interval, repeating the experiments many more times would serve to reduce the magnitude of the error bars and make these plots possible, adding credence to the data.

Creating a surface that is both superhydrophobic and capable of withstanding temperatures is a non-trivial task. Many superhydrophobic surfaces, such as those used by Srinivasan et al., are polymer-based, and may have glass transition temperatures of

$T_g < 120$ °C, which could cause them to soften, flow and modify their surface texture if used in the film boiling experiments. The etched and silanized aluminum surfaces used to obtain these results could only be used a few times before losing their superhydrophobicity, causing them to transition to nucleate boiling. It is suspected that the aluminum was getting boehmitized (Kim *et al.,* 2013), in spite of the passivation process aimed at avoiding this. Creating a robust surface that can withstand multiple experiments would greatly increase our ability to collect data. Alternatives such as using a brass surface are currently being considered.

A great number of interesting follow-up studies can be used to advance the field. Adding temperature control to the system would allow for studying the effect of temperature on the thickness and stability of the boiling film under rapid rotation, and probing drag reduction at higher Reynolds numbers may also be of interest. With the possibility of reducing skin friction drag by over 90% now a reality, this area of research certainly merits close monitoring over the coming years.

Appendix A: Designing and Fabrication a New Taylor-Couette Cell for Improved Imaging

The Taylor-Couette cell used for all the experiments described in this thesis was designed by Justin Kleingartner and contracted out for fabrication. However, multiple years of usage and repeated cycles of heating and cooling led to increasing difficulty in attaching it to the peltier plate. Imaging the rotating rotors through the curved glass walls also resulted in a great deal of image distortion. As such, it was determined that a new cell would be required.

Machining the cell presented several interesting challenges. The first of these was material selection. We wanted to leave the option for heating the cell through the Rheomter's peltier plate, so aluminum was a better choice than steel on account of its lower thermal mass. However, the lack of corrosion resistance of the former was a concern. This was mitigated by anodizing the cell after it was machined. While hard-coat anodizing was also considered for its superior corrosion and scratch resistance, the thickness of the oxide film was in the range of 0.002-0.005", which was considerably larger than the precision to which the cell was machined (0.0005"). A regular anodized coat was under 0.001" thick, and still provided adequate corrosion resistance, particularly since the cell was only intended to work with deionized water of various temperatures.

The second challenge lay in the machining process. The bottom of the cell had to fit firmly onto the peltier plate with minimal play, and the pocket that would house the glass cylinder had to fit it very precisely to minimize leaks. Furthermore, since these were both on opposite sides of the cell, it was essential that they be highly concentric. To achieve this, the first part of the operation was to pressure-turn the outside of the cell. The setup on the lathe is depicted in Figure A.1, below.

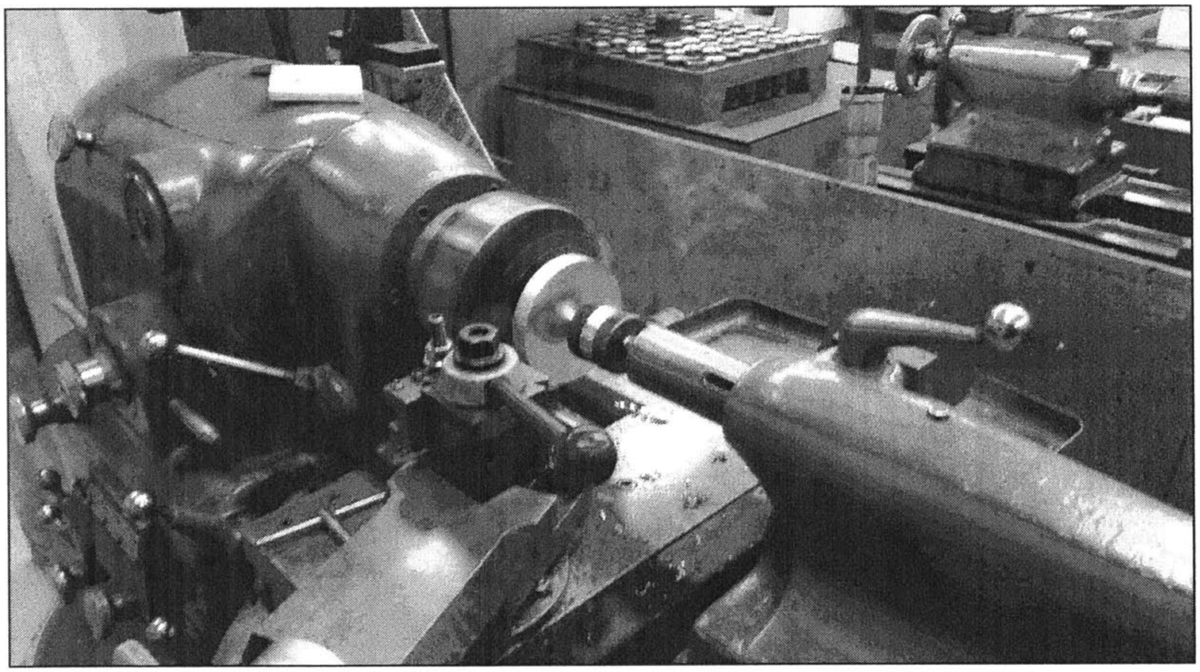

Figure A.0.1: Pressure turning the top of the Taylor-Couette cell

This surface would then serve as a reference. After transferring the part to the jaws of the lathe, an indicator dial was used to measure runout. The chuck of the lathe used was called a "buck chuck", meaning that it allowed for its concentricity to be adjusted. This allowed the jaws to be dialed in to within 0.0005" of the pressure-turned outer surface. The deeper pocket that would mate with the peltier cell was machined, and then the part was reversed in the jaws and dialed in again to the same precision relative to the outer surface. Finally, the pocket that would house the glass was machined in. O-ring grooves were added using grooving tools to ensure a snug, water-tight fit to the glass cylinder. Finally, the part was transferred to a mill, dialed in once again using indicators, and the slot which would house the outer walls was created. The cell is pictured in figure A.2, prior to anodizing.

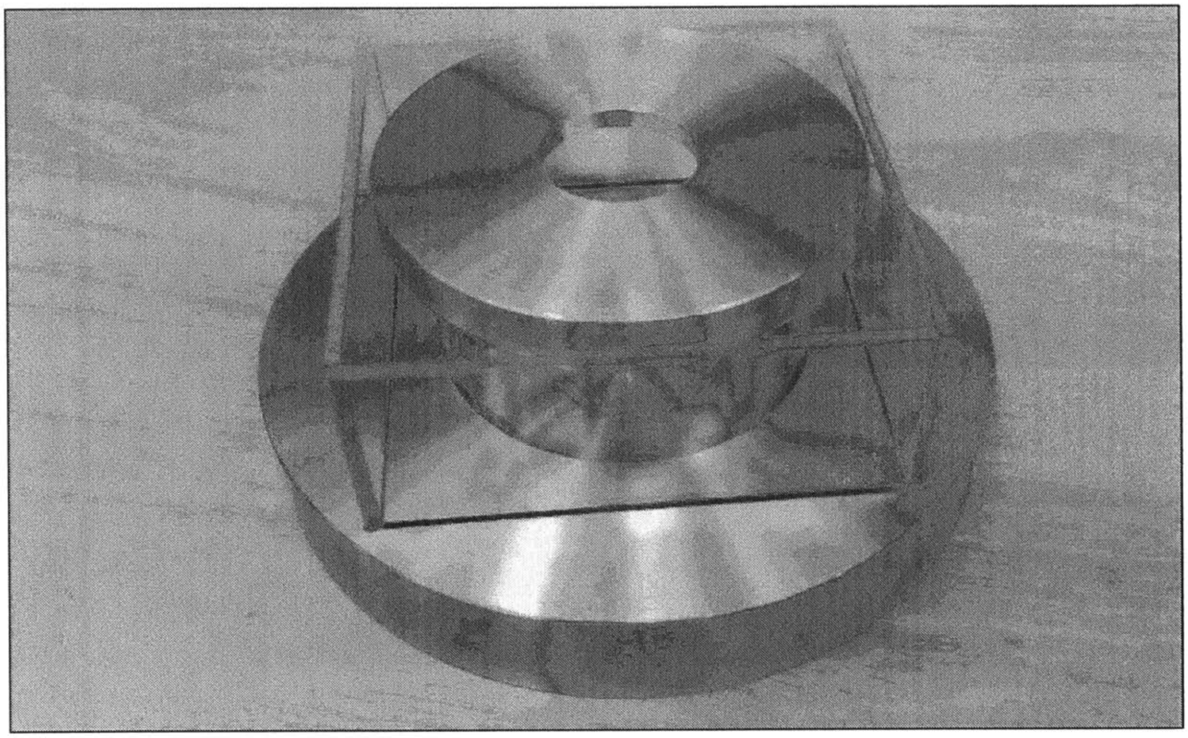

Figure A.0.2: The machined Taylor-Couette cell, prior to anodizing.

The four polycarbonate walls serve to house index-matched fluid. Light passing through the cell is thus refracted considerably less, leading to better imaging.

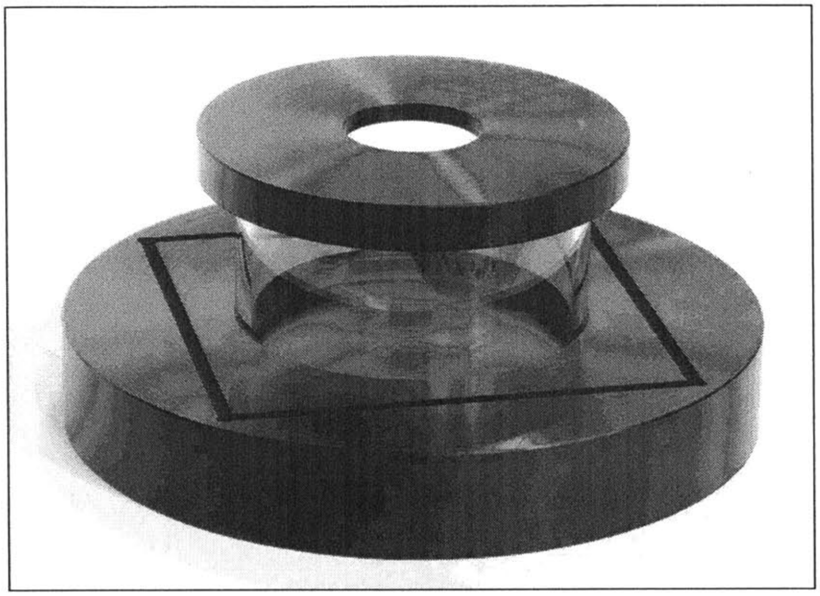

Figure A.3: The TC after anodizing. The polycarbonate walls have been removed to highlight the effect of anodizing.

Appendix B: The Hurst Exponent and the Mean Square Slope

B.2 Differentiating Between the Root Mean Square Roughness, the Hurst Exponent and the Mean Square Slope

The following parameters are obtained from laser profilometry of rough surfaces:

1) The Hurst exponent, *H*
2) The mean square height $m_0 = \langle h^2 \rangle$
3) The mean square slope $m_2 = \langle h'^2 \rangle$
4) Two characteristic dimensions: ξ (size of asperities) and λ (mean space between two asperities)

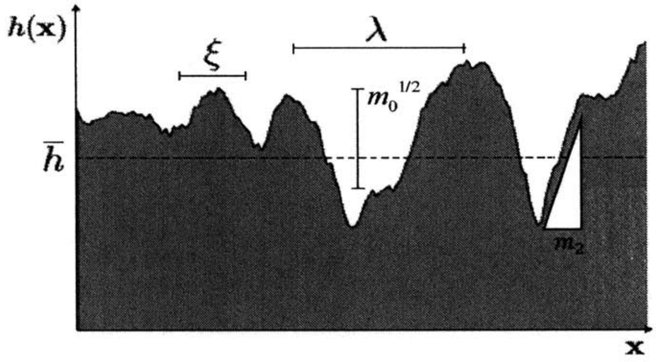

The plots below help elucidate the difference between the first three parameters:

$$h(x) = 3p + 2p\sin\left(2\pi\frac{x}{L}\right) + 0.5p\ \sin\left(2\pi\frac{5x}{L}\right) + 0.05p\ \sin\left(2\pi\frac{50x}{L}\right)$$

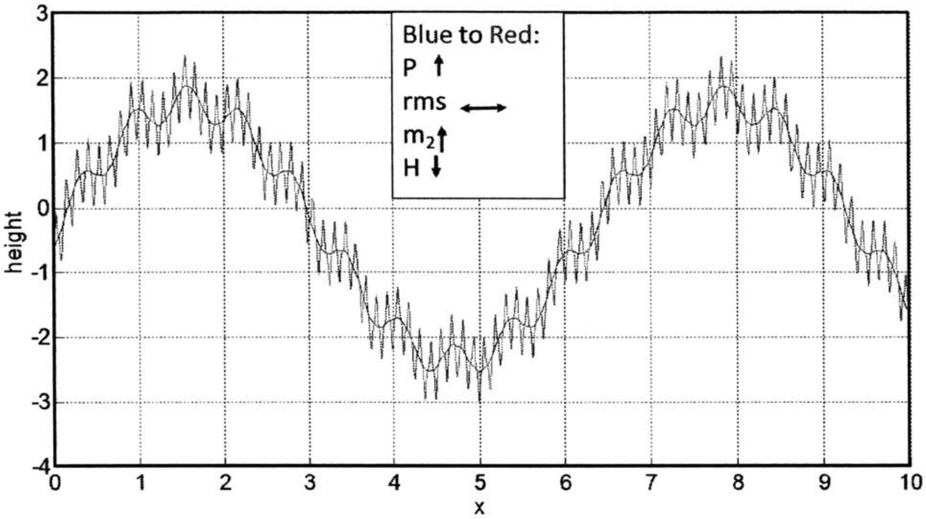

$$h(x) = 3p + 2p\sin\left(2\pi\frac{x}{L}\right) + 0.5p\ \sin\left(2\pi\frac{5x}{L}\right) + 0.05p\ \sin\left(2\pi\frac{50x}{L}\right)$$

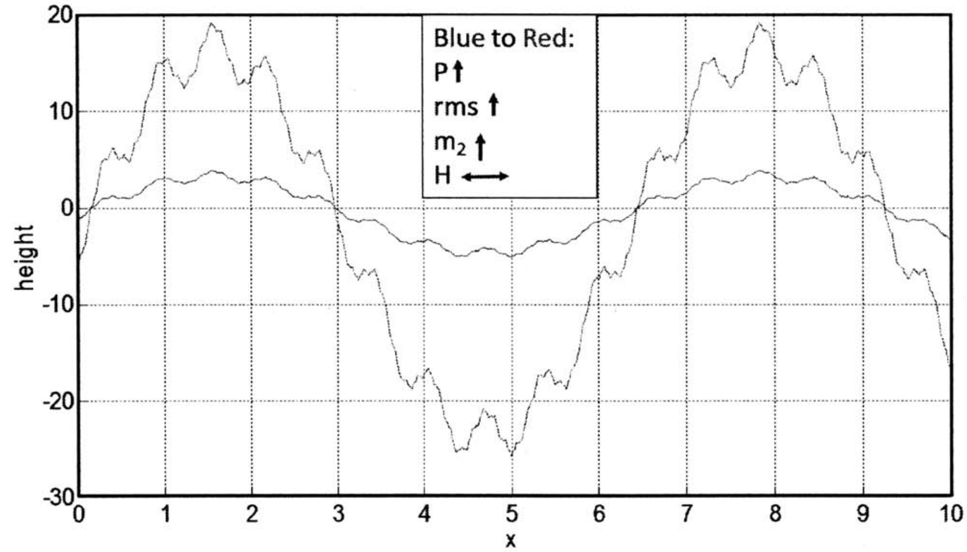

Appendix C: Derivation of Velocity Profiles for Two-Fluid Taylor-Couette System

Obtaining the value of b_{slip}, the Navier slip length, can be achieved using equation (6):

$$b = \frac{V_{slip}\mu}{\tau\big|_{y=0}} \qquad (6)$$

Solving for V_{slip} requires the velocity profile. Since the system is axially symmetric, one can solve for the velocity profile using the Navier-Stokes equation in cylindrical co-ordinates for an incompressible fluid. Since we assume laminar flow caused exclusively by the rotating inner cylinder, the fluid velocity is only in the tangential or θ direction.

Furthermore, if we assume that the flow is diven only by the motion of the rotor, and not by any pressure gradients or gravity, the result is equation (7), the velocity profile, where A, B, C and D are constants.

$$u_{steam} = \frac{A}{r} + Br \quad \text{for} \quad r_i < r < r_s$$

$$u_{water} = \frac{C}{r} + Dr \quad \text{for} \quad r_s < r < r_o \qquad (7)$$

The constants A,B,C and D can be solved for using the system boundary conditions. The first of these stems from the no-slip boundary condition at the steam-rotor interface. Two more arise at the steam-water interface, and represent velocity and shear stress continuity. The final boundary condition occurs at the water-outer wall boundary, and is one again no-slip condition.

Applying these boundary conditions to equation (7) allows us to solve for the constants A, B, C and D:

$$D = \frac{\mu_R(1+\varepsilon)^2\Omega\eta^2}{-\varepsilon(2+\varepsilon)+\mu_R\left[\eta^2(1+\varepsilon)^2-1\right]}$$

$$B = \frac{\left[1+\mu_R(\eta^2(1+\varepsilon)^2-1)\Omega\eta^2\right]}{\mu_R(1+\varepsilon)^2\eta^4-\eta^2(\mu_R+\varepsilon(2+\varepsilon))}$$

$$A = r_i^2(\Omega - B)$$

$$C = -Dr_o^2$$

Where $\mu_R = \frac{\mu_a}{\mu_w}$, $\eta = \frac{R_i}{R_o}$, $\varepsilon = \frac{R_s - R_i}{R_i} = \frac{h}{R_i}$.

With the velocity profile defined, we can now calculate the slip length. Plugging into equation (7) we obtain equation (8):

$$b_{slip} = \frac{R_i\Omega - u_{water}\left(R_i\right)}{r\frac{d}{dr}\left(\frac{u_{water}}{r}\right)\Big|_{r=R_i}} \tag{8}$$

Evaluating and dropping terms of order ε^2, this ultimately simplifies to equation (9)

$$b_{slip} = h\left[\frac{\mu_w}{\mu_a}-1\right]\left(\frac{R_o^2}{R_o^2-R_i^2}\right) \tag{9}$$

Appendix D: Drag Reduction Using Textured, non-Superhydrophobic Surfaces

D.1 Introduction and Motivation

A considerable section of this manuscript has been devoted to a discussion of methods to create superhydrophobic surfaces that optimize drag reduction in the turbulent flow regime. This requires chemical hydrophobicity, and a micro- or nano-structure to enhance this property. However, in a slight departure from all that has been considered thus far, the focus in this next section will turn to dispensing with the chemical aspect, and using surface geometry alone to achieve drag reduction. Studies and simulations have shown that a micro-texture alone may be enough to sustain drag reduction in the laminar regime. Wrinkles have been considered as way to create this texture, but the present research initiative will seek to create it using subtractive manufacturing methods. The allure of techniques such as machining lies in their scalability, relatively low cost, and the fact that they can be applied to just about any object with the correct tooling and setup.

D.2 Testing Apparatus and Methods

Once again, Srinivasan *et al.*'s tried and tested method to measure and evaluate drag reduction proved to be ideal, with the rheometer and the bespoke Taylor Couette cell allowing for accurate measurements across a range of Reynolds numbers. As with the film boiling experiments, however, certain changes were required. Fortunately, the modifications required were less extensive; far from requiring an elaborate setup involving liquid metals, high currents and high rotation rates, the only issue was creating two similar rotors – identical in every way except the surface finish. Where one would be as smooth as turning techniques would permit, the second would feature a micro-texture. A number of different textures were considered, the first of these being a series of triangle waves. This geometry was selected on account of the ease of creating it using turning tools. A high-speed stainless steel turning tool was sharpened using aluminum oxide and diamond abrasive wheels, resulting in a narrow, sharp point.

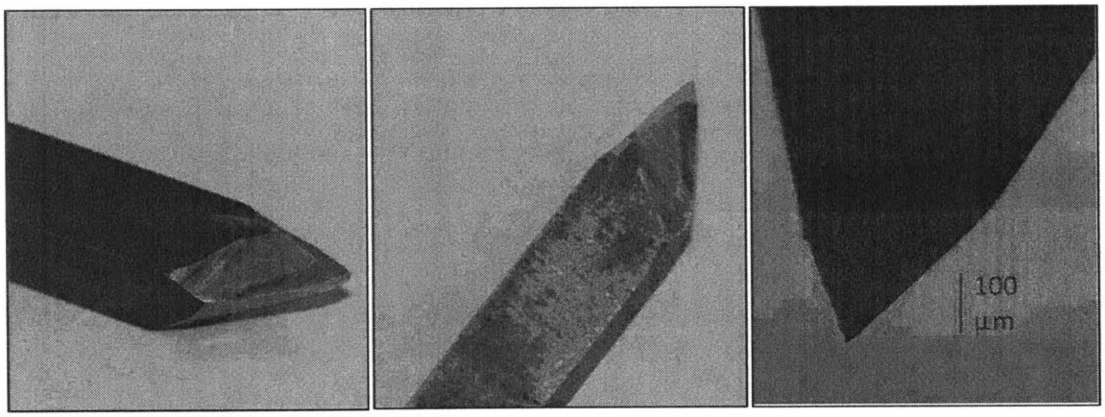

Up to this point, all geometries made by the author had been machined manually, as writing Gcode for a CNC machine to create a one-off or a low-volume output would not justify the extensive time required to create the code or setup the machine properly. In this case, however, creating 75 micron-grooves, while certainly achievable by hand, would be carried out much more quickly with a CNC machine. The CAM software used was Mastercam, and the instruction to the software was effectively to plunge the tool directly downwards into the curved face of the rotor, and then retract.

This approach is possible because the software treats the tool like as if it were a single point, where in reality, the tool tapers from a finite thickness down to a point. The result is a groove with the same profile as that of the machine tool, in this case a v-shape. Having made the groove, the software then retracts the tool, translates it along the axis of rotation to the next point, and plunges once again. The first attempt at creating these grooves was carried out on a rod of 6061 aluminum, and the resulting surface was analyzed under an SEM:

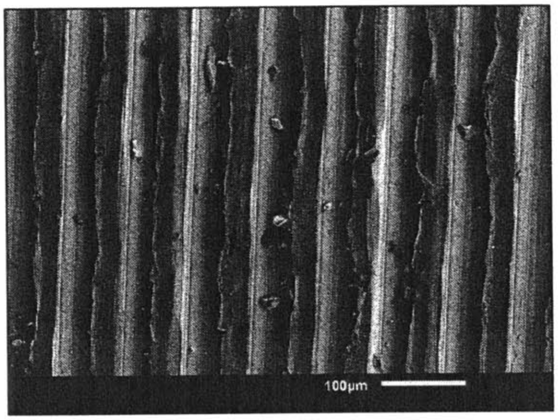

As the SEM images show, the grooves in this case are not particularly 'clean' – there are areas in which the base material has deformed or cracked rather than being fractured cleanly and being removed by the tool.

Since these additional striations and cracks added an unforeseen element to the system and could not be accounted in simulations, it was determined that they be minimized or removed completely. In order to do this, the cause of the issue was traced to a material property – toughness vs hardness. Aluminum, in particular the 6061 used to obtain the images above, is a relatively tough metal, but is not particularly hard. This means that is has a low yield stress, but requires a considerable amount to energy to fracture. In short, when a stress exerted is exerted upon it, it is more likely to deform than fracture. The solution lay in finding a material that was less tough, and could be broken off more easily, while also being machinable. Many other metals such as stainless steel and titanium, are very tough, and would therefore only exacerbate the issue. Ceramic, being extremely hard and brittle, has the ideal blend of properties, but requires carbide tools, which cannot be made as sharp as high speed steel ones. Furthermore, ceramic produces an abrasive white powder when machined, and this can be damaging to the lathe. The Haas CNC turning center being a sensitive and expensive piece equipment, it was undesirable to expose it to such elements.

Another option to use is to plastics. Two options were those that have already been discussed in this manuscript – Delrin and PAI. PAI is the harder and more brittle of the two, but is also substantially more expensive. Given the likelihood of several prototypes being required to achieve drag reduction, Delrin was the better option. The same grooves were put into a piece of Delrin, this time with a slightly different angle to the tool, leading to a slanted-V groove shape. The surface was once again imaged with an SEM:

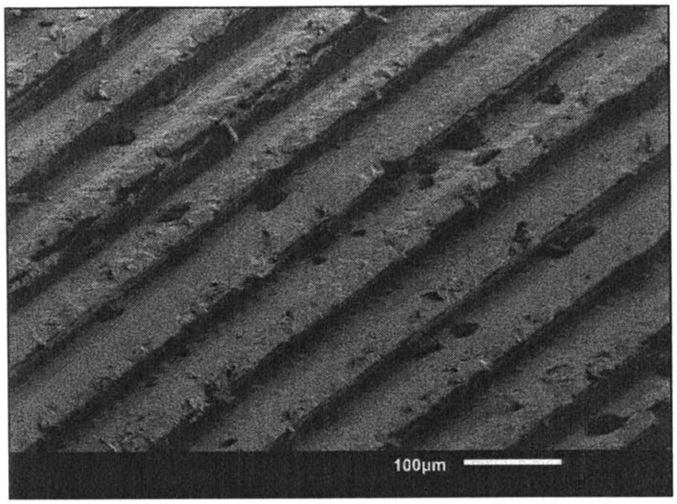

D.3 Moving Forward

Early tests seem to indicate that a wrinkled or grooved surface alone can offer drag reduction, and this opens up myriad possibilities for future studies. The prospect of combining these surfaces with an agent that changes the surface energy of water on the surface is an enticing one. Much of this manuscript is concerned with using hydrophobic agents such as POSS, PFDA and various silanes, but the mechanism at work in this case involves trapping water in the grooves, which a hydrophobic agent is likely to impede. Instead, using a hydrophilic agent might lead to better results. Hydrophilicity can also be created by adding an addition, smaller layer of roughness. Generally this would only serve to increase drag, but the entrapment of the liquid could lead to an entirely different result.

Combining these wrinkles with superhydrophobic surfaces does remain a possibility, in that they offer another length scale of roughness. The first study would consist of using iCVD to coat a grooved rotor in PFDA. The length scales are unlikely to be small enough to allow for robust superhydrophobicity and so it may also be worth adding additional roughness in the form of PMMA, for instance.

Bibliography

Aljallis, Elias, et al. "Experimental study of skin friction drag reduction on superhydrophobic flat plates in high Reynolds number boundary layer flow."*Physics of Fluids (1994-present)* 25.2 (2013): 025103.

Arkles, Barry. "Hydrophobicity, hydrophilicity and silane surface modification."*Gelest, Inc. Available via www. gelest. com. http://www. gelest. com/goods/pdf/Hydrophobicity. pdf* (2006).

Batista, J., et al. "Mercury in hair for a child population from Tarragona Province, Spain." *Science of the total Environment* 193.2 (1996): 143-148.

Bergman, Theodore L., Frank P. Incropera, and Adrienne S. Lavine.*Fundamentals of heat and mass transfer*. John Wiley & Sons, 2011.

Bernardin, J. D., and Issam Mudawar. "The Leidenfrost point: experimental study and assessment of existing models." *Journal of Heat Transfer* 121.4 (1999): 894-903.

Biance, Anne-Laure, Christophe Clanet, and David Quéré. "Leidenfrost drops."*Physics of Fluids (1994-present)* 15.6 (2003): 1632-1637.

Bill, Robert G., and William F. Herrnkind. "Drag reduction by formation movement in spiny lobsters." *Science* 193.4258 (1976): 1146-1148.

Bocquet, Lyderic, Patrick Tabeling, and Sébastien Manneville. "Comment on" Large Slip of Aqueous Liquid Flow over a Nanoengineered Superhydrophobic Surface"." *Physical review letters* 97.10 (2006): 109601.

Bonsignore, Frank. "An Investigation of the vapor cushion thickness, temperature, and vaporization time of Leidenfrost drops." (1981).

Bottiglione, F., and G. Carbone. "Role of statistical properties of randomly rough surfaces in controlling superhydrophobicity." *Langmuir* 29.2 (2012): 599-609.

Bushnell, Dennis M., and K. J. Moore. "Drag reduction in nature." *Annual Review of Fluid Mechanics* 23.1 (1991): 65-79.

Cassie, A. B. D., and S. Baxter. "Wettability of porous surfaces." *Transactions of the Faraday Society* 40 (1944): 546-551.

Choi, Chang-Hwan and Chang-Jin Kim (2006c). "Large Slip of Aqueous Liquid Flow over a Nanoengineered Superhydrophobic Surface". Phys. Rev. Lett. 96 (6), p. 066001.

Czech, E., and T. Troczynski. "Hydrogen generation through massive corrosion of deformed aluminum in water." *International Journal of Hydrogen Energy* 35.3 (2010): 1029-1037.

Daniello, Robert J., Nicholas E. Waterhouse, and Jonathan P. Rothstein. "Drag reduction in turbulent flows over superhydrophobic surfaces." *Physics of Fluids (1994-present)* 21.8 (2009): 085103.

De Gennes, Pierre-Gilles, Françoise Brochard-Wyart, and David Quéré (2004). Capillarity and wetting phenomena: drops, bubbles, pearls, waves. Springer.

Dong, Jim, and Norman N. Lichtin. "Drag-free hull for marine vessels." U.S. Patent No. 6,508,188. 21 Jan. 2003.

"Thermal Conductivity of Some Common Materials and Gases." *Engineering Toolbox*. Web. 7 Aug. 2015. <http://www.engineeringtoolbox.com/thermal-conductivity-d_429.html>.

Feuillebois, François, Martin Z. Bazant, and Olga I. Vinogradova. "Effective slip over superhydrophobic surfaces in thin channels." *Physical review letters*102.2 (2009): 026001.

Gadelmawla, E. S., et al. "Roughness parameters." *Journal of Materials Processing Technology* 123.1 (2002): 133-145.

Golovin, Kevin, et al. "Mechanically Robust Superhydrophobic Surfaces for Turbulent Drag Reduction." *Bulletin of the American Physical Society* 59 (2014).

Hayn, Ryan A., et al. "Preparation of highly hydrophobic and oleophobic textile surfaces using microwave-promoted silane coupling." *Journal of Materials Science* 46.8 (2011): 2503-2509.

Huisman, Sander G., et al. "Multiple states in highly turbulent Taylor–Couette flow." *Nature communications* 5 (2014).

Jones, Anthony C., and Michael L. Hitchman. *Chemical vapour deposition: precursors, processes and applications*. Royal Society of Chemistry, 2009.

Kim, Philseok, et al. "Hierarchical or not? Effect of the length scale and hierarchy of the surface roughness on omniphobicity of lubricant-infused substrates." *Nano letters* 13.4 (2013): 1793-1799.

Kleingartner, Justin A., et al. "Utilizing dynamic tensiometry to quantify contact angle hysteresis and wetting state transitions on nonwetting surfaces."*Langmuir* 29.44 (2013): 13396-13406.

Kovacik, Peter, et al. "Scale-up of oCVD: large-area conductive polymer thin films for next-generation electronics." *Mater. Horiz.* 2.2 (2015): 221-227.

Lafuma, Aurélie, and David Quéré. "Superhydrophobic states." *Nature materials*2.7 (2003): 457-460.

Leidenfrost, Johann Gottlob. *De aquae communis nonnullis qualitatibus tractatus*. Ovenius, 1756.

Mabry, Joseph M., et al. "Fluorinated Polyhedral Oligomeric Silsesquioxanes (F-POSS)." *Angewandte Chemie* 120.22 (2008): 4205-4208.

Marmur, Abraham, and Eyal Bittoun. "When Wenzel and Cassie are right: reconciling local and global considerations." *Langmuir* 25.3 (2009): 1277-1281.

McHale, Glen, et al. "Terminal velocity and drag reduction measurements on superhydrophobic spheres." *Applied Physics Letters* 94.6 (2009): 064104.

McHale, Glen, Michael I. Newton, and Neil J. Shirtcliffe. "Immersed superhydrophobic surfaces: Gas exchange, slip and drag reduction properties."*Soft Matter* 6.4 (2010): 714-719.

"More About Plastics", *McMaster Carr*. Web. 7 Aug. 2015. <http://www.mcmaster.com/#8574kac/=ye5p36>

Meuler, Adam J., et al. "Examination of wettability and surface energy in fluorodecyl POSS/polymer blends." *Soft Matter* 7.21 (2011): 10122-10134.

O'Hanley, Harry, et al. "Separate effects of surface roughness, wettability, and porosity on the boiling critical heat flux." *Applied Physics Letters* 103.2 (2013): 024102.

Quéré, David. "Leidenfrost dynamics." *Annual Review of Fluid Mechanics* 45 (2013): 197-215.

Read, B. E., and G. Williams. "The dielectric and dynamic mechanical properties of polyoxymethylene (Delrin)." *Polymer* 2 (1961): 239-255.

Reeja-Jayan, B., et al. "A route towards sustainability through engineered polymeric interfaces." *Advanced Materials Interfaces* 1.4 (2014).

Shirtcliffe, Neil J., et al. "Plastron properties of a superhydrophobic surface."*Applied Physics Letters* 89.10 (2006): 104106.

Shirtcliffe, Neil J., et al. "Superhydrophobic copper tubes with possible flow enhancement and drag reduction." *ACS applied materials & interfaces* 1.6 (2009): 1316-1323.

"Skin Friction Reduction Operating Costs", *Cortana.* Web. 19 December 2014. <http://www.cortana.com/SFR_Operating_Costs.htm>

"Mykroy/Mycalex Machinable Glass Bonded Mica Ceramics", *Crystex*. Web. 3 March 2015. <http://crystexllc.com/products/>

"Gallium Indium Tin", *Gallium Source*. Web. 9 March 2015. <http://www.mcssl.com/store/gallium-source/002---gallium-indium-tin-eutectic>

Sojoudi, Hossein, Gareth H. McKinley, and Karen K. Gleason. "Linker-free grafting of fluorinated polymeric cross-linked network bilayers for durable reduction of ice adhesion." *Materials Horizons* 2.1 (2015): 91-99.

Sojoudi, Hossein, et al. "Investigation into the Formation and Adhesion of Cyclopentane Hydrates on Mechanically-Robust Vapor-Deposited Polymeric Coatings." *Langmuir* (2015).

Srinivasan, Siddarth, et al. "Solution spraying of poly (methyl methacrylate) blends to fabricate microtextured, superoleophobic surfaces." *Polymer* 52.14 (2011): 3209-3218.

Srinivasan, Siddarth, et al. "Drag reduction for viscous laminar flow on spray-coated non-wetting surfaces." *Soft Matter* 9.24 (2013): 5691-5702.

Srinivasan, Siddarth, et al. "Sustainable Drag Reduction in Turbulent Taylor-Couette Flows by Depositing Sprayable Superhydrophobic Surfaces." *Physical review letters* 114.1 (2015): 014501.

Tasaltin, Nevin, et al. "Preparation and characterization of superhydrophobic surfaces based on hexamethyldisilazane-modified nanoporous alumina."*Nanoscale research letters* 6.1 (2011): 1-8.

Vakarelski, Ivan U., et al. "Drag reduction by Leidenfrost vapor layers."*Physical review letters* 106.21 (2011): 214501.

Vakarelski, Ivan U., et al. "Stabilization of Leidenfrost vapour layer by textured superhydrophobic surfaces." *Nature* 489.7415 (2012): 274-277.

Vallee, BERT L., and DAVID D. Ulmer. "Biochemical effects of mercury, cadmium, and lead." *Annual review of biochemistry* 41.1 (1972): 91-128.

Vinogradova, Olga I. "Drainage of a thin liquid film confined between hydrophobic surfaces." *Langmuir* 11.6 (1995): 2213-2220.

Weast, Robert C., et al. "Handbook of Chemistry and Physics. –1989–1990." (1989).

Wilson, Tony. "Confocal microscopy." *Academic Press: London, etc* 426 (1990): 1-64.

Wolf, A. V., Aqueous Solutions and Body Fluids, Harper and Row, New York, 1966. and Engineering Toolbox).

Woolford, B., et al. "Particle image velocimetry characterization of turbulent channel flow with rib patterned superhydrophobic walls." *Physics of Fluids (1994-present)* 21.8 (2009): 085106.

Xu, Qin, et al. "Effect of oxidation on the mechanical properties of liquid gallium and eutectic gallium-indium." *Physics of Fluids (1994-present)* 24.6 (2012): 063101.

Xu, Muchen, Guangyi Sun, and Chang-Jin Kim. "Infinite lifetime of underwater superhydrophobic states." *Physical review letters* 113.13 (2014): 136103.

Ybert, Christophe, et al. "Achieving large slip with superhydrophobic surfaces: Scaling laws for generic geometries." *Physics of Fluids (1994-present)* 19.12 (2007): 123601.

Young, Thomas. "An essay on the cohesion of fluids." *Philosophical Transactions of the Royal Society of London* (1805): 65-87.

Zhang, Xi, Huan Chen, and Hongyu Zhang. "Layer-by-layer assembly: from conventional to unconventional methods." *Chemical Communications* 14 (2007): 1395-1405.